ISSN 0021-3438 (Print)
ISSN 2412-8783 (Online)

IZVESTIYA

NON-FERROUS METALLURGY

Том 29, № 2, 2023

Scientific and Technical Journal
Founded in 1958
6 Issues per year

ИЗВЕСТИЯ ВУЗОВ

ЦВЕТНАЯ МЕТАЛЛУРГИЯ

Vol. 29, No. 2, 2023

Научно-технический журнал
Основан в 1958 г.
Выходит 6 раз в год

ISSN 0021-3438 (Print)
ISSN 2412-8783 (Online)

IZVESTIYA NON-FERROUS METALLURGY

Vol. 29, No. 2
2023

Scientific and Technical Journal Founded in 1958 6 Issues per year http://cvmet.misis.ru

Journal is included into the List of peer-reviewed scientific publications recommended by the Highest Attestation Commission of the Ministry of Education and Science of the Russian Federation for publishing the results of doctoral and candidate dissertations

Abstracting/Indexing: Russian Science Citation Index (RSCI), Chemical Abstracts (Online), INIS, OCLC ArticleFirst, Ulrich's Periodicals Directory, VINITI Database (Abstract Journal)

Founder

National University of Science and Technology "MISIS"
Address: 4 bld. 1 Leninskiy Prosp., Moscow 119049, Russia
http://www.misis.ru

Editorial Staff

Address: NUST MISIS, 4 bld. 1 Leninskiy Prosp., Moscow 119049, Russia
Phone: +7 (495) 638-45-35
E-mail: izv.vuz@misis.ru

Certificate of registration No. 015842 (13.03.1997)
Re-registration PI No. ФС77-79229 (25.09.2020)

Subscription: Ural-Press Agency

Leading Editor – O.V. Sosnina
Executive Editor – A.A. Kudinova
Layout Designer – E.A. Legkaya

Signed print 20.04.2023. Format 60×90 1/8.
Offset paper No. 1. Digital printing. Quires 10.25
Order 16756. Free price

Printed in the printing house of the MISIS Publish House
4 bld. 1 Leninskiy Prosp., Moscow 119049, Russia. Phone/fax: +7 (499) 236-76-17

ISSN 0021-3438 (Print)
ISSN 2412-8783 (Online)

ИЗВЕСТИЯ ВУЗОВ
ЦВЕТНАЯ МЕТАЛЛУРГИЯ

Том 29, № 2
2023

Научно-технический журнал Основан в 1958 г. Выходит 6 раз в год http://cvmet.misis.ru

Журнал включен в Перечень рецензируемых научных изданий, рекомендованных ВАК Минобрнауки РФ для публикации результатов диссертаций на соискание ученых степеней

Журнал включен в базы данных: Russian Science Citation Index (RSCI), Chemical Abstracts (Online), INIS, OCLC ArticleFirst, Ulrich's Periodicals Directory, РИНЦ, БД/РЖ ВИНИТИ

Учредитель

ФГАОУ ВО Национальный исследовательский технологический университет «МИСИС»
Адрес: 119049, г. Москва, Ленинский пр-т, 4, стр. 1
http://www.misis.ru

Редакция журнала

Адрес: 119049, г. Москва, Ленинский пр-т, 4, стр. 1. НИТУ МИСИС
Тел.: +7 (495) 638-45-35
E-mail: izv.vuz@misis.ru

Свидетельство о регистрации № 015842 от 13.03.1997 г.
Перерегистрация ПИ № ФС77-79229 от 25.09.2020 г.

Подписка: Агентство «Урал-пресс»

Ведущий редактор – О.В. Соснина
Выпускающий редактор – А.А. Кудинова
Дизайн и верстка – Е.А. Легкая

Подписано в печать 20.04.2023. Формат 60×90 1/8.
Бум. офсетная № 1. Печать цифровая. Усл. печ. л. 10,25
Заказ 16756. Цена свободная

Отпечатано в типографии Издательского Дома МИСИС
119049, г. Москва, Ленинский пр-т, 4, стр. 1. Тел./факс: +7 (499) 236-76-17

CONTENTS

СОДЕРЖАНИЕ

Metallurgy of Rare and Precious Metals

Металлургия редких и благородных металлов

Foundry

Литейное производство

Pressure Treatment of Metals

Обработка металлов давлением

Physical Metallurgy and Heat Treatment

Металловедение и термическая обработка

METALLURGY OF RARE AND PRECIOUS METALS / МЕТАЛЛУРГИЯ РЕДКИХ И БЛАГОРОДНЫХ МЕТАЛЛОВ

UDC 669.872
https://doi.org/10.17073/0021-3438-2023-2-5-14

Research article
Научная статья

Kinetic regularities of hydrometallurgical recycling of spent displays: behavior of indium

E.B. Kolmachikhina, O.B. Kolmachikhina, Ya.A. Yankina, Z.M. Golibzoda

Ural Federal University named after the First President of Russia B.N. Yeltsin
19 Mira Str., Yekaterinburg 620002, Russia

✉ Elvira B. Kolmachikhina (e.b.khazieva@urfu.ru)

Abstract: This article discusses the physicochemical regularities of indium leaching from the surface of glass plates of used displays in various acids. The glass of used displays was pre-cleaned from polarizers and crushed. Their base is comprised of silicon and aluminum oxides. Indium is presented in the form of $In_2O_3 \cdot SnO_2$. Indium content in the material obtained is 174.8 mg/kg. Individual solutions of sulfuric, hydrochloric and methanesulfonic acids were used as leaching agents. The influence of concentrations of the mentioned acids (0.1–1.0 N), leaching duration (10–60 min), temperature (298–353 K) and liquid-to-solid ratio (L : S = (7.5÷15.0): 1 cm^3/g) on the degree of indium extraction into solution has been determined. Partial orders of reaction in terms of CH_3SO_3H, H_2SO_4, HCl are 0.69, 0.67 and 1.10, respectively. In the course of experiments an intensive increase in indium concentration was observed in the first 20–40 min f leaching in H_2SO_4 and HCl solutions. The process rate then decreased and indium extraction actually did not increase, due to a fall in the amount of non-reacted indium. During leaching in 0.1–0.4 N in CH_3SO_3H solutions, the rate of indium dissolution did not change throughout the experiment, since the amount of non-reacted indium gas decreased insignificantly. The acids considered here can be ranked in the following ascending order of their efficiency for indium dissolution: CH_3SO_3H, H_2SO_4, HCl, which corresponds to the growth of strengths of these acids. An increase in the temperature led to a significant increase in indium extraction. The apparent activation energies of In_2O_3 dissolution in CH_3SO_3H, H_2SO_4, HCl solutions have were calculated as equal to 51.4, 51.2, 43.4 kJ/mole, respectively. It was established that with the use of HCl as leaching agent, the increase in the fraction of liquid phase in the slurry from 7.5 : 1 to 15 : 1 cm^3/g lead to fall in indium extraction by 2.4 times and the initial leaching rate by 3.2 times. It was demonstrated that an increase in L : S during indium dissolution in CH_3SO_3H (from 7.5 : 1 to 15 : 1 cm^3/g) and H_2SO_4 (from 10 : 1 to 15 : 1 cm^3/g) is accompanied by insignificant changes in extraction and initial leaching rate. Therefore, the studies performed demonstrated that indium leaching from glasses of spent displays flows in mixed mode upon the use of HCl and in kinetic mode in H_2SO_4 and CH_3SO_3H solutions.

Keywords: indium, leaching, hydrochloric acid, sulfuric acid, methanesulfonic acid, kinetics, apparent activation energy, order of reaction

Acknowledgments: This works was supported by the Russian Science Foundation, Project No. 22-79-00129. https://rscf.ru/en/project/22-79-00129

For citation: Kolmachikhina E.B., Kolmachikhina O.B., Yankina Ya.A., Golibzoda Z.M. Kinetic regularities of hydrometallurgical recycling of spent displays: behavior of indium. *Izvestiya. Non-Ferrous Metallurgy.* 2023;29(2):5–14.
https://doi.org/10.17073/0021-3438-2023-2-5-14

Кинетические закономерности гидрометаллургической переработки отслуживших дисплеев: поведение индия

Э.Б. Колмачихина, О.Б. Колмачихина, Я.А. Янкина, З.М. Голибзода

Уральский федеральный университет имени первого Президента России Б.Н. Ельцина
620002, Россия, г. Екатеринбург, ул. Мира, 19

✉ Эльвира Барыевна Колмачихина (e.b.khazieva@urfu.ru)

Аннотация: Изучены физико-химические закономерности выщелачивания индия с поверхности стеклянных пластин отработанных дисплеев в различных кислотах. Стекла отслуживших дисплеев были предварительно очищены от поляризаторов и

измельчены. Их основу составляли оксиды кремния и алюминия. Индий представлен в виде соединения $In_2O_3 \cdot SnO_2$. Содержание индия в полученном материале составляло 174,8 мг/кг. В качестве выщелачивающих агентов использовали индивидуальные растворы серной, соляной и метансульфоновой кислот. Установлено влияние концентраций указанных кислот (0,1–1,0 н), продолжительности выщелачивания (10–60 мин), температуры (298–353 K) и соотношения жидкого к твердому (Ж : Т = = (7,5÷15,0) : 1 $см^3$/г) на степень извлечения индия в раствор. Частные порядки реакций по CH_3SO_3H, H_2SO_4, HCl составили 0,69, 0,67 и 1,10 соответственно. В ходе экспериментов наблюдалось интенсивное повышение концентрации индия в первые 20–40 мин выщелачивания в растворах H_2SO_4 и HCl, после чего скорость процесса снижалась и извлечение индия практически не росло вследствие уменьшения количества непрореагировавшего индия. При выщелачивании в 0,1–0,4 н растворах CH_3SO_3H скорость растворения индия не менялась на всем протяжении эксперимента ввиду того, что количество непрореагировавшего индия снижалось незначительно. Исследуемые кислоты можно расположить в следующий ряд в порядке возрастания их эффективности в растворении индия: CH_3SO_3H, H_2SO_4, HCl, что соответствует росту сил данных кислот. Увеличение температуры значительно повышало извлечение индия. Рассчитаны значения кажущейся энергии активации растворения In_2O_3 в растворах CH_3SO_3H, H_2SO_4, HCl, составившие 51,4, 51,2, 43,4 кДж/моль соответственно. Обнаружено, что при использовании в качестве выщелачивающего агента HCl увеличение доли жидкой фазы в пульпе от 7,5 : 1 до 15 : 1 $см^3$/г снижало извлечение индия в 2,4 раза, а начальную скорость выщелачивания – в 3,2 раза. Показано, что повышение Ж : Т при растворении индия в CH_3SO_3H (с 7,5 : 1 до 15 : 1 $см^3$/г) и H_2SO_4 (с 10 : 1 до 15 : 1 $см^3$/г) сопровождается незначительным изменением извлечения и начальной скорости выщелачивания. Таким образом, проведенные исследования показали, что выщелачивание индия из стекол отслуживших дисплеев протекает в смешанном режиме при использовании HCl и в кинетическом режиме в растворах H_2SO_4 и CH_3SO_3H.

Ключевые слова: индий, выщелачивание, соляная кислота, серная кислота, метансульфоновая кислота, кинетика, кажущаяся энергия активации, порядок реакции

Благодарности: Исследование выполнено за счет гранта Российского научного фонда № 22-79-00129.
https://rscf.ru/project/22-79-00129

Для цитирования: Колмачихина Э.Б., Колмачихина О.Б., Янкина Я.А., Голибзода З.М. Кинетические закономерности гидрометаллургической переработки отслуживших дисплеев: поведение индия. *Известия вузов. Цветная металлургия*. 2023;29(2):5–14. https://doi.org/10.17073/0021-3438-2023-2-5-14

Introduction

In the recent 20 years the structure of indium consumption has significantly changed. This metal was previously mainly used for fabrication of alloys, electrical components, and semiconductors. At the present time, the major portion of indium is used in the form of indium-tin oxide (ITO). The latter is the solid solution of indium and tin oxides (90 % In_2O_3, 10 % SnO_2) characterized by semiconductor properties and transparency in visible light. Due to these properties ITO is essential in production of LED and OLED displays, solar cells, inter alia.

The main source of indium is zinc sulfide ore, with a content of 1—100 g/t [1]. At the existing level of indium consumption (about 1500 t/year) [2], its reserves in mineral ores will be sufficient only for the next decade. Used monitors are the most promising secondary source of indium.

In Russia the reprocessing of used displays is limited to the disposal of boards and luminescent lamps. At present displays are recycled only in a few countries (South Korea, Japan, and Belgium) due to the low content of valuable metals and complex composition of products.

Displays include several layers: polarizers, glass plates, liquid crystals. The glass plates are coated with ITO layer with a thickness of 50—200 nm. The indium content in them is 100—350 mg/kg [2, 3]. On the reverse side of glass substrate a polarizer layer from polyvinyl acetate film is applied.

Preliminary preparation of glass plates before reprocessing can include the stages of crushing and grinding [4]. However, the presence of polarizer film makes disintegration more difficult. High temperature processing at T = 453÷493 K allows the polarizer to be embrittled, thus increasing the efficiency of glass crushing [4, 5]. Moreover, it is possible to separate ITO particles from glass substrate by thermal processing at T = 923 K in 8—10 min and subsequently removing the product by compressed air [6]. Other methods of ITO concentrating include gravimetric separation [4], floatation [7], abrasive processing of glass surface [8, 9] and others.

Pyrometric techniques allow oxides of indium and tin to be recovered [10, 11] and then distilled, including in the form of chlorides [12]. Hydrometallurgical reprocessing procedures of glass plates include leaching in various acids (sulfuric [8, 9, 13, 14], hydrochloric [15], nitric [16], citric, malic [17]) with subsequent concentrating and separation of metals by liquid extraction [15, 18, 19] (di-(2-ethylhexyl) phosphoric acid, tributyl phos-

phate) and sorption [20, 21] (Lewatit TP 208, Lewatit VP OC 1026). The dissolution processes can be intensified by oxidizing and reducing agents [22], as well as by ultrasound processing [6, 23, 24], and so on.

This work presents a comparative assessment of the kinetics of indium leaching from the surface of glass plates of spent displays in sulfuric, hydrochloric and methanesulfonic acids. The latter is considered as "green" organic acid due to its relatively low toxicity, biodegradability, high boiling point and very low pressure of saturated vapors [25, 26]. In addition, methanesulfonic acid is characterized by high electrical conductivity, and its salts are highly soluble in water [25]. In recent years this acid has been considered as a leaching agent in studies on the reprocessing of copper, zinc, bismuth raw materials [26—28], as well as in the technology of The Paroo Station (Australia) for lead extraction from cerussite ore [29, 30].

The acids applied in this work are referred to as strong: they can be arranged in the ascending order of increase in their strength expressed in terms of the dissociation constant (pK_{a1}): CH_3SO_3H (–1,86), H_2SO_4 (–3), HCl (–7) [31, 32].

The aim of this work is to analyse the influence of the concentration of acids, duration, temperature and slurry density on physicochemical regularities of dissolution of indium from the surface of glass plates of spent displays.

Experimental

Materials, equipment and research methods

Glass from used monitors was first washed with water, dried in air, then held at 463 K for softening and manual removal of film. The cleaned glass was crushed in a rod mill. After sieving, the –1 mm fraction of crushed glass was separated for further experiments. After thorough mixing of the material, a representative sample was selected by means of quartering. This was then used for subsequent chemical analysis using a novAA 300 atomic absorption spectrophotometer (AAS) ("Analytik Jena", Germany). The particle size of the material was determined using a HELOS&RODOS laser diffraction analyzer of particle sizes ("Sympatec GmbH", Germany). The morphology of crushed glass samples and their chemical composition were analyzed using a JEOL JSM-6390LA scanning electron microscope (Japan), equipped with a JED-2300 system of energy dispersion microanalysis.

The main bulk of the material (>85 %) included particles of irregular shape with a size of less than 300 μm (Fig. 1, 2). According to the data of elemental analysis and previous studies [3, 12], the oxides of aluminum, silicon, and calcium prevailed in the material. Indium

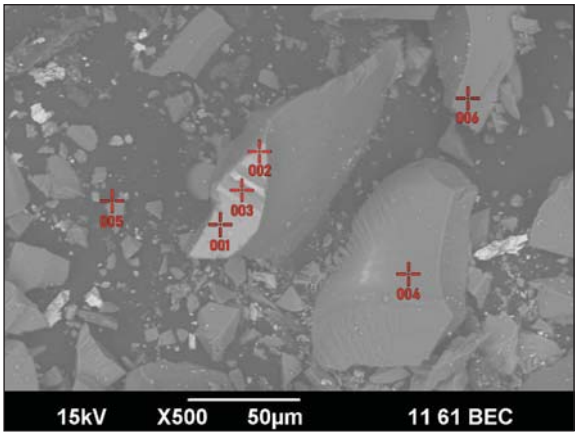

Element	Number of measurement region					
	001	002	003	004	005	006
	Content,%					
Na	1.0	0.8				
Mg				1.7	4.0	1.3
Al	2.8	8.6	12.9	19.1	20.2	14.3
Si	69.0	74.4	77.4	68.5	69.0	56.8
Ca	4.1	4.0	3.2	10.7	6.8	27.6
Mo			6.5			
In	19.9	10.1				
Sn	3.2	2.1				

Fig. 1. SEM image and elemental composition of crushed display glass

Рис. 1. СЭМ-изображение и элементный состав измельченных стекол дисплеев

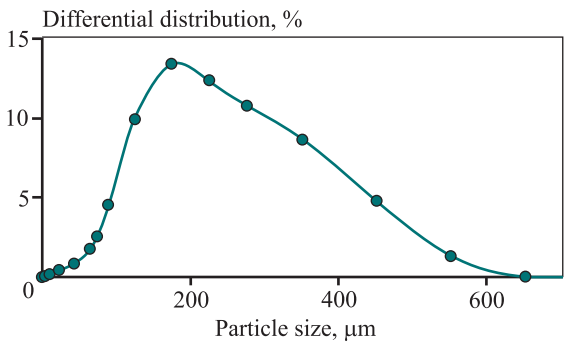

Fig. 2. Particle size distribution of crushed display glass

Рис. 2. Гранулометрический состав измельченных стекол дисплеев

and tin compounds were present on the glass surface (points *1*, *2* in Fig. 1), Molybdenum compounds were present on the surface of conducting tracks (point *3*, Fig. 1). The crushed display glass contained, mg/kg: In — 174.8, Sn — 1.7.

In the experiments, H_2SO_4 sulfuric acid (chemical pure grade), HCl acid (chemically pure grade) and CH_3SO_3H methanesulfonic acid (chemically pure grade) were used. The initial solution of the acids were prepared by distilled water dilution, and agitated using a magnetic stirrer.

Leaching of crushed glasses

The leaching experiments were carried out in a 0.5 dm^3 thermostatic reactor at T = 298÷353 K, τ = = 10÷60 min, concentration of acids 0.1—1.0 N, liquid to solid ratio L : S = (7.5÷15.0) : 1 cm^3/g. While varying L : S, the mass ratio of hydrogen and indium ions was maintained at a constant in the sample (10 mg H^+/1 mg In). Respectively, the concentrations of acids in this series of experiments varied from 0.15 to 0.3 N.

Solutions of acids with preset concentration were poured into the reactor, sealed, and heated to preset temperature with continuous stirring. Then a sample of material (20 g) was loaded into the reactor and the slurry temperature was automatically maintained with an accuracy of ±2 K.

The slurry after leaching was filtered, and the cake was washed with distilled water. Then the cake was treated at T = 363 K in 20 % solution of hydrochloric acid in several hours for complete passing of metals into solution. Then the cake was also filtered and washed with distilled water. Samples taken during leaching, filtrates after leaching and treatment with acid. The washing waters were also analyzed for content of indium ions using an AAS novAA300 ("Analytik Jena", Germany). Total indium extraction (α_{In}) was assessed by its content in the filtrates and washing waters.

Experimental data processing

The degree of indium extraction was assessed accounting for volumes of taken samples using the following equation:

$$\alpha_{In}^{i} = \frac{C^i[V_{исх} - V_{пр}(i-1)] + \sum_1^{i-1}(C^i V_{пр})}{G_{In}} \cdot 100\ \%, \quad (1)$$

where α^i_{In} is the degree of indium extraction at the time of taking the i-th sample, %; C^i is the concentration of indium in the i-th sample, g/dm^3; V_{sample} is the sample volume, dm^3; V_{ini} is the initial volume of leaching solution, dm^3; and G_{In} is the indium weight in the sample, g.

The kinetic properties (partial orders of reactions, apparent activation energy) were determined by detection of instant leaching rate at initial time (υ_0) by plotting tangents to the curves $\alpha_{In} = f(\tau)$. The tangents were plotted via the coordinate origin.

The generalizing equation for the rate of indium leaching can be written as follows:

$$\frac{d\alpha}{d\tau} = k(T, \nu)[C(\alpha)]^n [P(\alpha)]^m S(\alpha), \quad (2)$$

where k is the rate constant depending on temperature and, in the case of diffusion or mixed mode, on speed of liquid motion with regard to the surface of solid particles (ν). C and n are the concentration of acids and partial order in terms of concentration, respectively. P and m are the slurry density and partial order in terms of slurry density, respectively. $S(\alpha)$ is the function describing the cumulative surface area of reaction, as a function of extent of reaction behavior (determine by the particle shapes and particle size distribution).

Results and discussion

The influence of concentration of acids on indium extraction

The data obtained (Fig. 3) shows the changes in the pattern of dependences $\alpha_{In} = f(\tau)$ in the case of various acids. Thus, for instance, in H_2SO_4 and HCl solutions (Fig. 3, *a*, *b*) in the first 20—40 min of leaching, the intensive dissolution of indium was observed. Then the process rate significantly decreased due to a decrease in the amount of non-reacted ITO (see Fig. 3, *a*, curves *3*, *4* and Fig. 3, *b*, curves *2—4*), also in the concentration of H^+ ions (Fig. 3, *a*, curves *1*, *2* and Fig. 3, *b*, curve *1*). In the case of 0.1—0.4 N CH_3SO_3H solutions, the plots $\alpha_{In} = f(\tau)$ were a straight line. The rate of indium dissolution actually did not change throughout the experiments (Fig. 3, *c*) due to low extraction and the high amount of non-reacted indium.

At a relatively low concentration of leaching agents (0.1—0.2 N), the indium extraction in 60 min was higher in HCl solutions (α_{In} = 50÷100 %) than in solutions of H_2SO_4 (α_{In} = 43÷76 %) and CH_3SO_3H (α_{In} = 25÷39 %). With an increase in the acid concentration to 0.4—1.0 N already at 40 min, the indium is extracted nearly completely into H_2SO_4 and HCl solutions (α_{In} = 97÷100 %). On the other hand, its extraction (α_{In} = 84 %) with the

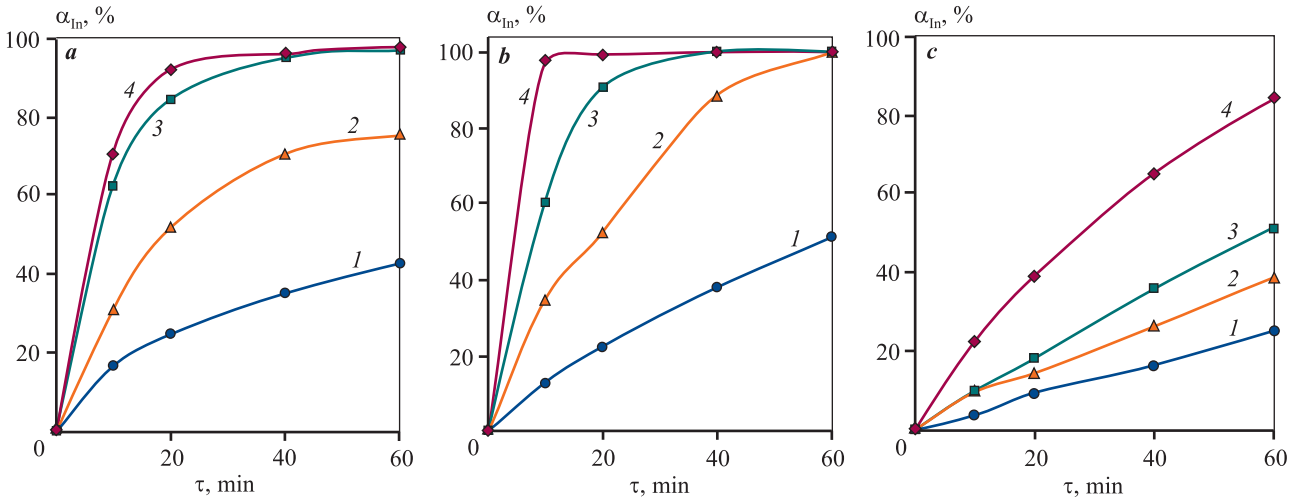

Fig. 3. Indium recovery as a function of leaching duration at different concentrations of H_2SO_4 (***a***), HCl (***b***) and CH_3SO_3H (***c***)
T = 333 K; L : S = 10 : 1 cm^3/g; C_{acids}; N: 0.1 (***1***), 0.2 (***2***), 0.4 (***3***) and 1.0 (***4***)

Рис. 3. Влияние продолжительности выщелачивания на извлечение индия при различных концентрациях H_2SO_4 (***a***), HCl (***b***) и CH_3SO_3H (***c***)
T = 333 K; Ж : Т = 10 : 1 $см^3/г$; $C_{кислот}$, н: 0,1 (***1***), 0,2 (***2***), 0,4 (***3***) и 1,0 (***4***)

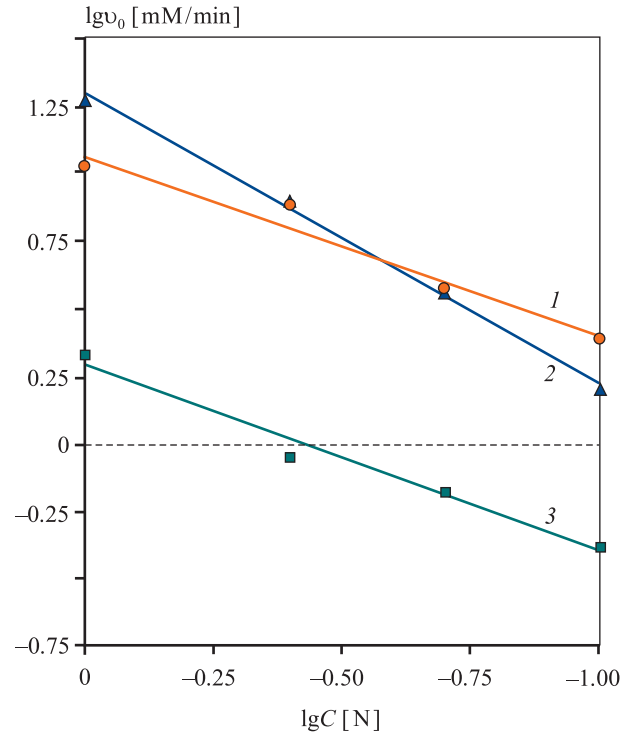

Fig. 4. Determination of partial orders of indium leaching reactions in different acids
1 – H_2SO_4, ***2*** – HCl, ***3*** – CH_3SO_3H

Рис. 4. Определение частных порядков реакций выщелачивания индия в различных кислотах
1 – H_2SO_4, ***2*** – HCl, ***3*** – CH_3SO_3H

use of CH_3SO_3H was achieved only at $C_{CH_3SO_3H}$ = 1.0 and in 60 min of leaching.

Partial orders of indium leaching in terms of H_2SO_4, HCl and CH_3SO_3H, were determined by the angle coefficients of lines plotted in lgυ$_0$—lg$C$ coordinates (Fig. 4), were 0.67, 1.10 and 0.69, respectively.

The values obtained for α_{In} and the regularities of their variation are in good agreement with the dissociation coefficients of acids. Thus, HCl was dissociated nearly completely, and its apparent extent of dissociation varies insignificantly with an increase in concentration, contrary to H_2SO_4 and CH_3SO_3H. The increase in HCl concentration leads to proportional increase in CH^+, hence to an increase in α_{In}, υ$_0$. In H_2SO_4 and CH_3SO_3H solutions, the release of free H^+ ions is restricted by interionic interactions.

The influence of temperature on indium extraction

A temperature increase from 298 to 353 K naturally leads to increased indium extraction from H_2SO_4, HCl and CH_3SO_3H solutions by 83, 87 and 67 %, respectively (Fig. 5). At low temperatures (298—313 K), the efficiency of CH_3SO_3H was minimum .At T = 298 K, the indium oxide in fact did not dissolve, and at 313 K it did not exceed 10 % (Fig. 5, *c*).

The minimum indium extraction at T = 353 K, C_{acids} = 0.2 N was obtained with the use of CH_3SO_3H (70 % in 60 min), and the maximum extraction was

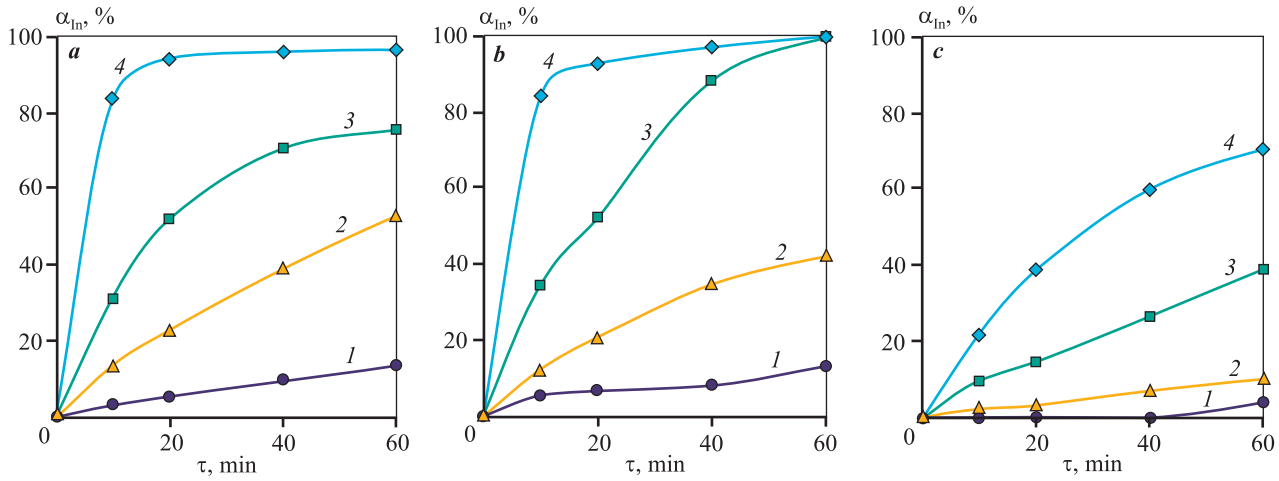

Fig. 5. Influence of leaching duration on Indium extraction as a function of leaching duration in H_2SO_4 (***a***), HCl (***b***) and CH_3SO_3H (***c***) solutions at different temperatures
L : S = 10 : 1 cm^3/g; C_{acids} = 0.2 N; *T*, K: 298 (***1***), 313 (***2***), 333 (***3***) and 353 (***4***)

Рис. 5. Влияние продолжительности выщелачивания на извлечение индия в растворах H_2SO_4 (***a***), HCl (***b***) и CH_3SO_3H (***c***) при различных температурах
Ж : Т = 10 : 1 $см^3$/г; $C_{кислот}$ = 0,2 н; *T*, K: 298 (***1***), 313 (***2***), 333 (***3***) и 353 (***4***)

in HCl solution (100 % in 60 min). During leaching in H_2SO_4 and HCl solutions at T = 353 K, the major portion of indium was dissolved in the first 10—20 min.

The kinetic regularities obtained allowed the apparent activation energy (E_a) of indium oxide dissolution in various acids to be calculated (Fig. 6): H_2SO_4 — 51.2 kJ/mole, HCl — 43.4 kJ/mole, CH_3SO_3H — 51.4 kJ/mole. The values E_a for the reactions of In_2O_3 with H_2SO_4 and CH_3SO_3H are sufficiently close and in combination with the obtained values of partial orders in terms of acids evidence process run in kinetic mode. Most probably, the leaching in these acids is limited by their dissociation with subsequent interaction of H^+ ions with ITO. Similar E_a of In dissolution in H_2SO_4 was obtained in [34]. The apparent activation energy of In dissolution in HCl solution and the partial order in terms of acid, the process runs in mixed mode.

The influence of slurry density on indium extraction

In this series of experiments the indium behavior was assessed at various slurry densities, maintaining a constant flow rate of hydrogen ions and slurry temperature. The results obtained (Fig. 7) confirm the significant influence of diffusion on indium leaching from ITO in solutions of hydrochloric acid. With an increase in the fraction of liquid phase in the slurry (from 7.5 : 1 to 15 : 1 cm^3/g) α_{In} decreased by 2.4 times, and

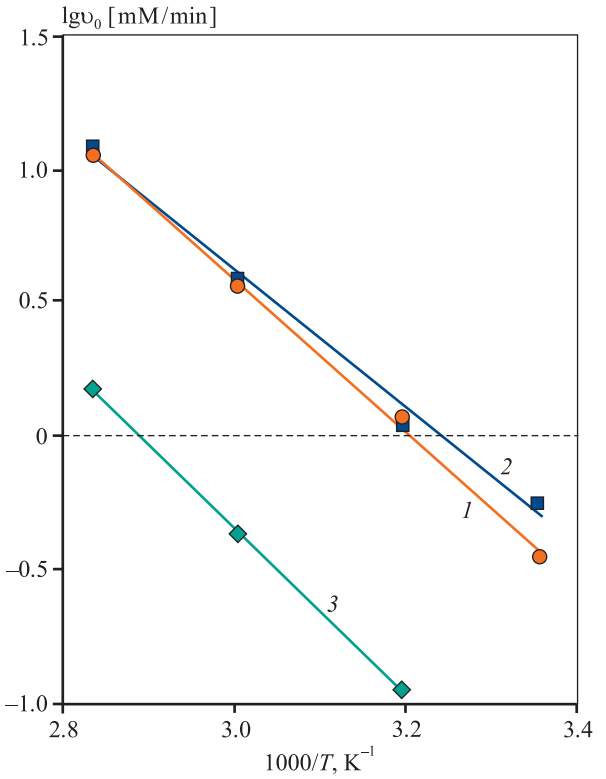

Fig. 6. $lg\upsilon_0$ as a function of $1/T$ for determination of apparent energy activation of indium dissolution in different acids
1 – H_2SO_4, ***2*** – HCl, ***3*** – CH_3SO_3H

Рис. 6. Графики зависимости $lg\upsilon_0$ от $1/T$ для определения кажущейся энергии активации растворения индия в различных кислотах
1 – H_2SO_4, ***2*** – HCl, ***3*** – CH_3SO_3H

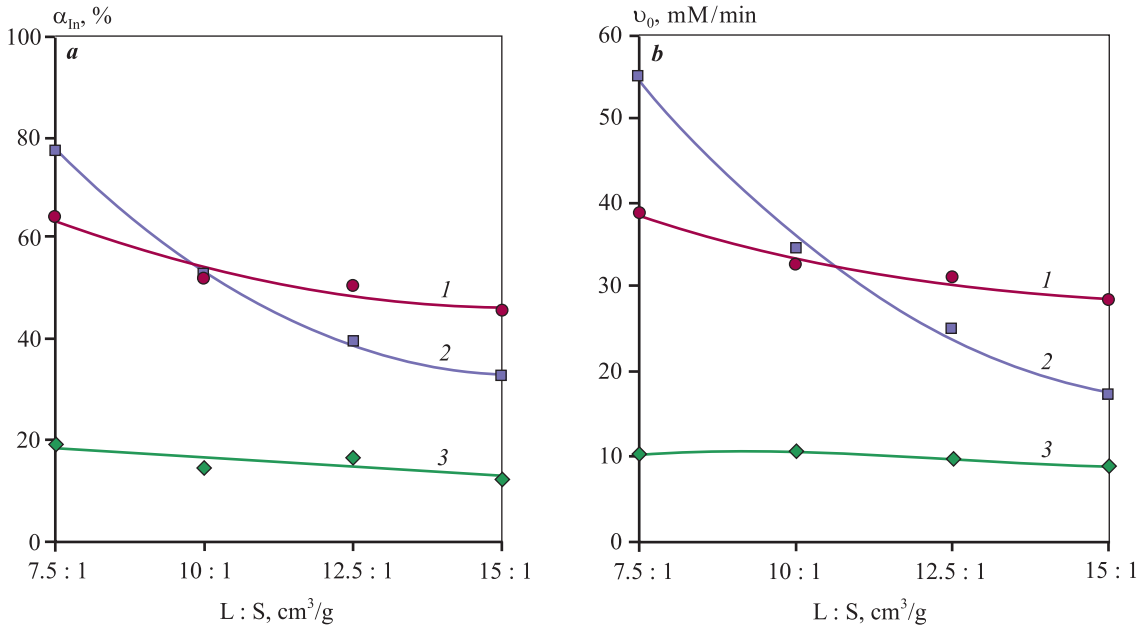

Fig. 7. Extraction (at τ = 20 min) (***a***) and initial leaching rate from solutions of different acids (***b***) as a function of slurry density

1 – H_2SO_4, ***2*** – HCl, ***3*** – CH_3SO_3H; T = 333 K

Рис. 7. Влияние плотности пульпы на извлечение (при τ = 20 мин) (***a***) и начальные скорости выщелачивания (***b***) индия из растворов различных кислот

1 – H_2SO_4, ***2*** – HCl, ***3*** – CH_3SO_3H; T = 333 K

υ_0 decreased by 3.2 times. In solutions of sulfuric acid with an increase in the fraction of liquid phase from 7.5 : 1 to 10 : 1 cm^3/g, α_{In} decreased by 12 %, and υ_0 by 6 mmol/min. Upon further increase in the volume of liquid in the slurry (L : S = (10÷15) : 1) both properties varied insignificantly. In the solutions of methanesulfonic acid in overall L : S range, α_{In} varied by 5 %, and υ_0 by 2 mmol/min.

Therefore, upon indium leaching in H_2SO_4 (L : S = = (10÷15) : 1) and CH_3SO_3H (L : S = (7.5÷15) : 1) solutions, the influence of slurry density was minimum.

Conclusions

The studies performed aimed at establishing the influence of acids (H_2SO_4, HCl and CH_3SO_3H), their concentrations (0.1—1.0 N), temperature modes (298—353 K), slurry density (L : S = (7.5÷15.0) : 1) and leaching duration (10—60 min) of used monitors demonstrated the fundamental influence of these parameters on kinetics of indium extraction into solution. The following conclusions were obtained on the basis of the obtained experimental results.

1. In the overall range of the considered acids, a high efficiency of hydrochloric acid was detected. Using this acid, 100 % indium extraction was achieved in 40 min of leaching in 0.4 N solution at T = 333 K. The increase in the HCl concentration to 1.0 N decreased the process duration to 10 min.

2. An increase in the leaching temperature allows significant improvement in indium extraction. The values of apparent activation energy of indium leaching obtained show evidence of the predominant process in kinetic mode with the use of sulfuric and methanesulfonic acids, and in mixed mode upon leaching in hydrochloric acids.

3. An increase in the fraction of liquid phase in the slurry (at constant flow rate of hydrogen ions to indium) leads to a decrease in extraction and initial rate of indium dissolution in hydrochloric acid solutions. During leaching in solutions of sulfuric and methanesulfonic acids, an insignificant influence of slurry density on extraction and initial rates of indium dissolution was observed.

References

1. Mineral commodity summaries 2022. URL: https://pubs.usgs.gov/periodicals/mcs2022/mcs2022.pdf (accessed: 24.02.2023).
2. Illés I.B., Nagy S., Kékesi T. The recycling of pure metallic indium from waste LCD screens by a combined

hydro-electrometallurgical method. *Hydrometallurgy*. 2022;213:105945.
https://doi.org/10.1016/j.hydromet.2022.105945

3. Wang H.Y. A study of the effects of LCD glass sand on the properties of concrete. *Waste Management*. 2009;29(1):335—341.
https://doi.org/10.1016/j.wasman.2008.03.005
4. Savvilotidou V., Kousaiti A., Batinic B., Vaccari M., Kastanaki E., Karagianni K., Gidarakos E. Evaluation and comparison of pre-treatment techniques for recovering indium from discarded liquid crystal displays. *Waste Management*. 2019;87:51—61.
https://doi.org/10.1016/j.wasman.2019.01.029
5. Li J., Gao S., Duan H., Liu L. Recovery of valuable materials from waste liquid crystal display panel. *Waste Management*. 2009;29(7):2033—2039.
https://doi.org/10.1016/j.wasman.2008.12.013
6. Chinnam R.K., Ujaczki É., O'Donoghue L. Leaching indium from discarded LCD glass: A rapid and environmentally friendly process. *Journal of Cleaner Production*. 2020;277:122868.
https://doi.org/10.1016/j.jclepro.2020.122868
7. Wang S., He Y., Yang J., Feng Y. Enrichment of indium tin oxide from colour filter glass in waste liquid crystal display panels through flotation. *Journal of Cleaner Production*. 2018;189:464—471.
https://doi.org/10.1016/j.jclepro.2018.04.096
8. Lahtela V., Virolainen S., Uwaoma A., Kallioinen M., Kärki T., Sainio T. Novel mechanical pre-treatment methods for effective indium recovery from end-of-life liquid-crystal display panels. *Journal of Cleaner Production*. 2019;230:580—591.
https://doi.org/10.1016/j.jclepro.2019.05.163
9. Virolainen S., Huhtanen T., Laitinen A., Sainio T. Two alternative process routes for recovering pure indium from waste liquid crystal display panels. *Journal of Cleaner Production*. 2020;243:118599.
https://doi.org/10.1016/j.jclepro.2019.118599
10. Wang Y., Wang R., Zhang C., Wang J. Full components recovery of organic matter and indium from discarded liquid crystal display panels. *Journal of Cleaner Production*. 2021;299:126862.
https://doi.org/10.1016/j.jclepro.2021.126862
11. Zhang L., Wu B., Chen Y., Xu Z. Energy and valuable resource recovery from waste liquid crystal display panels by an environment-friendly technological process: Pyrolysis of liquid crystals and preparation of indium product. *Journal of Cleaner Production*. 2017;162:141—152.
https://doi.org/10.1016/j.jclepro.2017.06.031
12. Park K-S., Sato W., Grause G., Kameda T., Yoshioka T. Recovery of indium from In_2O_3 and liquid crystal display powder via a chloride volatilization process using polyvinyl chloride. *Thermochimica Acta*. 2009;493(1-2):105—108.
https://doi.org/10.1016/j.tca.2009.03.003
13. Rocchetti L., Amato A., Fonti V., Ubaldini S., de Michelis I., Kopacek B., Vegliò F., Beolchini F. Cross-current leaching of indium from end-of-life LCD panels. *Waste Management*. 2015;42:180—187.
https://doi.org/10.1016/j.wasman.2015.04.035
14. Houssaine Moutiy E., Tran L-H., Mueller K.K., Coudert L., Blais J-F. Optimized indium solubilization from LCD panels using H_2SO_4 leaching. *Waste Management*. 2020;114:53—61.
https://doi.org/10.1016/j.wasman.2020.07.002
15. Kato T., Igarashi S., Ishiwatari Y., Furukawa M., Yamaguchi H. Separation and concentration of indium from a liquid crystal display via homogeneous liquid—liquid extraction. *Hydrometallurgy*. 2013;137:148—155.
https://doi.org/10.1016/j.hydromet.2013.06.004
16. Lee C-H., Jeong M-K., Fatih Kilicaslan M., Lee J-H., Hong H-S., Hong S-J. Recovery of indium from used LCD panel by a time efficient and environmentally sound method assisted HEBM. *Waste Management*. 2013;33(3):730—734.
https://doi.org/10.1016/j.wasman.2012.10.002
17. Argenta A.B., Reis C.M., Mello G.P., Dotto G.L., Tanabe E.H., Bertuol D.A. Supercritical CO_2 extraction of indium present in liquid crystal displays from discarded cell phones using organic acids. *The Journal of Supercritical Fluids*. 2017;120:95—101.
https://doi.org/10.1016/j.supflu.2016.10.014
18. Virolainen S., Ibana D., Paatero E. Recovery of indium from indium tin oxide by solvent extraction. *Hydrometallurgy*. 2011;107(1-2):56—61.
https://doi.org/10.1016/j.hydromet.2011.01.005
19. Ruan J., Guo Y., Qiao Q. Recovery of indium from scrap TFT-LCDs by solvent extraction. *Procedia Environmental Sciences*. 2012;16:545—551.
https://doi.org/10.1016/j.proenv.2012.10.075
20. Assefi M., Maroufi S., Nekouei R.K., Sahajwalla V. Selective recovery of indium from scrap LCD panels using macroporous resins. *Journal of Cleaner Production*. 2018;180:814—822.
https://doi.org/10.1016/j.jclepro.2018.01.165
21. Fortin-Lecomte C., Tran L-H., Rioux G., Coudert L., Blais J-F. Recovery of indium from acidic leach solutions of spent LCD panels using ion exchange. *Hydrometallurgy*. 2022;210:105845.
https://doi.org/10.1016/j.hydromet.2022.105845
22. Qin J., Ning S., Fujita T., Wei Y., Zhang S., Lu S. Leaching of indium and tin from waste LCD by a time-efficient method assisted planetary high energy ball milling. *Waste Management*. 2021;120:193—201.
https://doi.org/10.1016/j.wasman.2020.11.028

23. Zhang K., Li B., Wu Y., Wang W., Li R., Zhang Y-N., Zuo T. Recycling of indium from waste LCD: A promising non-crushing leaching with the aid of ultrasonic wave. *Waste Management*. 2017;64:236—243. https://doi.org/10.1016/j.wasman.2017.03.031
24. Souada M., Louage C., Doisy J-Y., Meunier L., Benderrag A., Ouddane B., Bellayer S., Nuns N., Traisnel M., Maschke U. Extraction of indium-tin oxide from end-of-life LCD panels using ultrasound assisted acid leaching. *Ultrasonics Sonochemistry*. 2018;40:929—936. https://doi.org/10.1016/j.ultsonch.2017.08.043
25. Gernon M.D., Wu M., Buszta T., Janney P. Environmental benefits of methanesulfonic acid. *Green Chemistry*. 1999;1(3):127—140. https://doi.org/10.1039/A900157C
26. Palden T., Onghena B., Regadío M., Binnemans K. Methanesulfonic acid: a sustainable acidic solvent for recovering metals from the jarosite residue of the zinc industry. *Green Chemistry*. 2019;21(19):5394—5404. https://doi.org/10.1039/C9GC02238D
27. Wang H., Yang S., Chang C., Zhou X., Deng X., He J., He X., Chen Y. Direct oxidative pressure leaching of bismuth sulfide concentrate in methanesulfonic acid medium. *Hydrometallurgy*. 2020;194:105347. https://doi.org/10.1016/j.hydromet.2020.105347
28. Wu J., Ahn J., Lee J. Kinetic and mechanism studies using shrinking core model for copper leaching from chalcopyrite in methanesulfonic acid with hydrogen peroxide. *Mineral Processing and Extractive Metallurgy Review*. 2021;42(1):38—45. https://doi.org/10.1080/08827508.2020.1795850
29. Wu Z., Dreisinger D.B., Urch H., Fassbender S. Fundamental study of lead recovery from cerussite concentrate with methanesulfonic acid (MSA). *Hydrometallurgy*. 2014;142:23—35. https://doi.org/10.1016/j.hydromet.2013.10.018
30. Dreisinger D., Baxter K., Worland A., Cooper T., Cau T., Waters N. Lead metal production at Paroo station mine using leach-electrowinning process in methane sulfonic acid solution. In: *PbZn 2020: 9th International Symposium on Lead and Zinc Processing* (San Diego, USA, 23—27 February, 2020). Switzerland, Springer, 2020. P. 135—163. https://doi.org/10.1007/978-3-030-37070-1_12
31. Zinchenko A.V., Izotova S.G., Rumyantsev A.V. The new handbook of the chemist and technologist. Chemical equilibrium. Properties of solutions. Saint Petersburg: Autonomous noncommercial organization scientific-production association «Professional», 2004. 998 p. (In Russ.).
Зинченко А.В., Изотова С.Г., Румянцев А.В. Новый справочник химика и технолога. Химическое равновесие. Свойства растворов. С.-Пб.: АНО НПО «Профессионал», 2004. 998 с.
32. Guthrie J.P. Hydrolysis of esters of oxy acids: pK_α values for strong acids; Brønsted relationship for attack of water at methyl; free energies of hydrolysis of esters of oxy acids; and a linear relationship between free energy of hydrolysis and pKa holding over a range of 20° pK units. *Canadian Journal of Chemistry*. 1978;56(17):2342—2354. https://doi.org/10.1139/v78-385
33. Illés I.B., Kékesi T. The application of selective leaching and complex anion exchange in a novel aqueous process to produce pure indium from waste liquid crystal display panels. *Journal of Environmental Chemical Engineering*. 2022;10(5):108420. https://doi.org/10.1016/j.jece.2022.108420
34. Cao Y., Li F., Li G., Huang J., Zhu H., He W. Leaching and purification of indium from waste liquid crystal display panel after hydrothermal pretreatment: Optimum conditions determination and kinetic analysis. *Waste Management*. 2020;102:635—644. https://doi.org/10.1016/j.wasman.2019.11.029

Information about the authors

Elvira B. Kolmachikhina – Cand. Sci. (Eng.), Research Professor of the Laboratory of Advanced Technologies for Complex Processing of Mineral and Technogenic Raw Materials of Non-Ferrous and Ferrous Metals, Ural Federal University named after the First President of Russia B.N. Yeltsin (UrFU).
https://orcid.org/0000-0002-6007-498X
E-mail: e.b.khazieva@urfu.ru

Olga B. Kolmachikhina – Cand. Sci. (Eng.), Associated Professor of the Department of non-ferrous metallurgy, UrFU.
E-mail: o.b.kolmachikhina@urfu.ru

Информация об авторах

Эльвира Барыевна Колмачихина – к.т.н., науч. сотрудник лаборатории перспективных технологий комплексной переработки минерального и техногенного сырья цветных и черных металлов, Уральский федеральный университет имени первого Президента России Б.Н. Ельцина (УрФУ).
https://orcid.org/0000-0002-6007-498X
E-mail: e.b.khazieva@urfu.ru

Ольга Борисовна Колмачихина – к.т.н., доцент кафедры металлургии цветных металлов, УрФУ.
E-mail: o.b.kolmachikhina@urfu.ru

Yana A. Yankina – Student of the Department of Non-Ferrous Metallurgy, UrFU.
E-mail: yankina.1999@mail.ru

Zamira M. Golibzoda – Student of the Department of Non-Ferrous Metallurgy, UrFU.
E-mail: golibzoda@mail.ru

Яна Александровна Янкина – студентка кафедры металлургии цветных металлов, УрФУ.
E-mail: yankina.1999@mail.ru

Замира Мирзомурод Голибзода – студентка кафедры металлургии цветных металлов, УрФУ.
E-mail: golibzoda@mail.ru

Contribution of the authors

E.B. Kolmachikhina – determined the purpose of the work, conducted experiments and analyses, prepared the text.

O.B. Kolmachikhina – participated in the discussion of the results, prepared the text.

Ya.A. Yankina – conducted experiments, performed chemical analysis, participated in the discussion of the results.

Z.M. Golibzoda – conducted experiments, participated in the discussion of the results.

Вклад авторов

Э.Б. Колмачихина – определение цели работы, проведение экспериментов и анализов, подготовка текста статьи.

О.Б. Колмачихина – участие в обсуждении результатов, подготовка текста статьи.

Я.А. Янкина – проведение экспериментов, выполнение химического анализа, участие в обсуждении результатов.

З.М. Голибзода – проведение экспериментов, участие в обсуждении результатов.

The article was submitted 27.09.2022, revised 05.03.2023, accepted for publication 06.03.2023

Статья поступила в редакцию 27.09.2022, доработана 05.03.2023, подписана в печать 06.03.2023

FOUNDRY / ЛИТЕЙНОЕ ПРОИЗВОДСТВО

UDC 621.74.045
https://doi.org/10.17073/0021-3438-2023-2-15-28

Research article
Научная статья

Analysis of the slurry and ceramic properties for investment casting obtained with domestic colloidal silica binders

V.E. Bazhenov[1], E.P. Kovyshkina[1], A.V. Sannikov[1], A.V. Koltygin[1], D.V. Ten[1], A.A. Rizhsky [1], V.D. Belov[1], E.A. Lazarev[2]

[1] **National University of Science and Technology "MISIS"**
4 bld. 1 Leninskiy Prosp., Moscow 119049, Russia

[2] **Public Joint Stock Company UEC "Kuznetsov"**
29 Zavodskoe shosse, Samara 443009, Russia

✉ Viacheslav E. Bazhenov (V.E.Bagenov@gmail.com)

Abstract: The quality of cast parts produced by investment casting is largely determined by the quality of the ceramic molds. Currently, aircraft and engine building enterprises are switching to an environmentally friendly colloidal silica binders for the manufacture of ceramic molds. In this work, the dynamic and relative viscosity of slurries prepared using fused silica powder and colloidal silica binders of the VT13-02U (Vakuumteh LLC), Stavroform VS (Polymet LLC), UltraCast One + and UltraCast Prime (both Technopark LLC) manufacturers were determined. It is shown that the slurries prepared on the considered binders have similar viscosity values, and in their rheological properties they are close to Newtonian liquids. The values of dynamic and relative viscosity at a binder content of 400 mL per 1 kg of fused silica powder were ~732 mPa·s and ~380 s, respectively. With an increase in the binder content to 600 mL per 1 kg of fused silica powder, the dynamic and relative viscosity decreased to ~70 mPa·s and ~16 s, respectively. An equation was also found that relates the dynamic viscosity determined using a rotational viscometer and the relative viscosity determined using the VZ-4 viscosimeter. The mechanical properties were determined during three-point bending tests on ceramic samples obtained using slurries on the above-mentioned colloidal silica binders and fused silica stucco. Samples obtained on binders VT13-02U, Stavroform VS and UltraCast One+ showed very similar bending strength values, namely 3.5–4.3 MPa after drying and 5.8–6.1 MPa after firing. Due to the presence of a polymer addition in the binder, the ceramic samples obtained on the UltraCast Prime binder had higher values of bending strength after drying and after firing – 6.4 and 7.2 MPa, respectively. It was also shown that with an increase in the viscosity of the slurry and a decrease in the fraction of fused silica stucco, the strength of the samples increases. The lowest surface roughness was observed for samples obtained with UltraCast grade binders.

Keywords: investment casting, nickel superalloy castings, colloidal silica binder, fused silica powder, slurry, viscosity, mechanical properties

Acknowledgments: This research received financial support from the Ministry of Science and Higher Education in the Russian Federation (Agreement No. 075-11-2022-023 from 06 April 2022) under the program "Scientific and technological development of the Russian Federation" according to governmental decree No. 218 dated 9 April 2010.

For citation: Bazhenov V.E., Kovyshkina E.P., Sannikov A.V., Koltygin A.V., Ten D.V., Rizhsky A.A., Belov V.D., Lazarev E.A. Analysis of the slurry and ceramic properties for investment casting obtained with domestic colloidal silica binders. *Izvestiya. Non-Ferrous Metallurgy.* 2023;29(2):15–28. https://doi.org/10.17073/0021-3438-2023-2-15-28

Анализ свойств суспензии и керамики для литья по выплавляемым моделям, полученных на отечественных связующих на водной основе

В.Е. Баженов[1], Е.П. Ковышкина[1], А.В. Санников[1], А.В. Колтыгин[1], Д.В. Тен[1], А.А.Рижский[1], В.Д. Белов[1], Е.А. Лазарев[2]

[1] **Национальный исследовательский технологический университет «МИСИС»**
119049, Россия г. Москва, Ленинский пр-т, 4, стр. 1

[2] **Публичное акционерное общество ОДК «Кузнецов»**
443009, Россия, г. Самара, Заводское шоссе, 29

✉ Вячеслав Евгеньевич Баженов (V.E.Bagenov@gmail.com)

Аннотация: Качество литых деталей, изготовленных методом литья по выплавляемым моделям, в значительной мере определяется качеством керамических форм. В настоящее время предприятия авиа- и двигателестроения переходят на экологически безопасное водное связующее для изготовления керамических форм. В работе определены динамическая и условная вязкости суспензий, приготовленных с использованием пылевидного плавленого кварца и отечественных водных связующих марок ВТ13-02У (ООО «Вакуумтех»), Ставроформ ВС (ООО «Полимет»), UltraCast One+ и UltraCast Prime (ООО «Технопарк»). Показано, что полученные суспензии имеют близкие значения вязкости и по своим реологическим свойствам близки к ньютоновским жидкостям. Значения динамической и условной вязкости при содержании связующего 400 мл на 1 кг пылевидного кварца составили ~732 мПа·с и ~380 с соответственно. При увеличении содержания связующего до 600 мл на 1 кг пылевидного кварца вязкость снизилась до ~70 мПа·с и ~16 с соответственно. Также было выведено уравнение, связывающее динамическую вязкость, определенную с помощью ротационного вискозиметра, и условную вязкость, установленную с помощью прибора ВЗ-4. Были определены механические свойства при испытаниях на трехточечный изгиб керамических образцов, полученных с использованием суспензий на указанных выше связующих и обсыпки из плавленого кварца. Образцы, полученные на связующих ВТ13-02У, Ставроформ ВС и UltraCast One+, показали очень близкие значения прочности: 3,5–4,3 МПа после сушки и 5,8–6,1 МПа после прокалки. Из-за наличия в составе связующего полимерной добавки керамические образцы на связующем UltraCast Prime имели более высокие значения прочности на изгиб после сушки и после прокалки – 6,4 и 7,2 МПа соответственно. Также было показано, что с увеличением вязкости суспензии и уменьшением фракции плавленого кварца прочность керамических образцов возрастает. Из всех рассмотренных связующих наименьшая шероховатость поверхности наблюдалась у образцов, полученных с использованием связующих UltraCast.

Ключевые слова: литье по выплавляемым моделям, жаропрочные никелевые отливки, водные связующие, пылевидный кварц плавленый (ПКП), суспензия, вязкость, механические свойства

Благодарности: Работа выполнена при финансовой поддержке Министерства науки и высшего образования Российской Федерации в рамках Постановления Правительства № 218 по соглашению о предоставлении субсидии № 075-11-2022-023 от 06.04.2022 г. «Создание технологии изготовления уникальных крупногабаритных отливок из жаропрочных сплавов для газотурбинных двигателей, ориентированной на использование отечественного оборудования и организацию современного ресурсоэффективного, компьютероориентированного литейного производства».

Для цитирования: Баженов В.Е., Ковышкина Е.П., Санников А.В., Колтыгин А.В., Тен Д.В., Рижский А.А., Белов В.Д., Лазарев Е.А. Анализ свойств суспензии и керамики для литья по выплавляемым моделям, полученных на отечественных связующих на водной основе. *Известия вузов. Цветная металлургия.* 2023;29(2):15–28. https://doi.org/10.17073/0021-3438-2023-2-15-28

Introduction

Casting quality plays a critical role in ensuring the overall reliability of an aircraft engine. One of the key determinants of casting quality is the quality of ceramic molds used in the investment casting process. These molds must be of high quality to produce castings with high dimension accuracy and smooth surface finishes.

Two binders are commonly used for making ceramic molds for investment casting of large nickel superalloy parts. The first binder is based on a hydrolyzed

solution of ethyl silicate, which is typically dissolved in ethanol or a mixture of ethanol and isopropanol. The second binder is an aqueous colloidal solution of silica [3]. Currently, foundries are increasingly adopting aqueous colloidal silica binders [4]. These binders contain Na-stabilized amorphous SiO_2 particles, which form silica gel as moisture is removed, thereby bonding the stucco particles together to create the ceramic mold [5—7].

Binders containing hydrolyzed ethyl silicate solutions are unsuitable for advanced, unattended foundries because organic solvents used in these binders are highly flammable. The latest environmental regulations ban the use of ethyl silicate due to health hazards associated with the organic solvents and ammonia vapors used in the curing of ceramic molds [5, 7, 8]. In contrast, aqueous colloidal silica binders are environmentally friendly and well-suited for unattended production facilities. Additionally, they are cost-effective and can reduce casting costs [9—12].

Fused silica powder (FSP) can be used as a component of slurry to make ceramic molds for casting large nickel superalloy parts. Fused silica (FS) with various particle sizes is used as stucco [13, 14]. Alumina is not typically used as stucco for large castings due to its high density which can result in overly heavy molds. Fused (amorphous) silica is preferred because it has a thermal expansion coefficient that is approximately 27 times less than that of crystalline silica [15, 16].

However, colloidal silica binders have some disadvantages compared with hydrolyzed ethyl silicate binders, including a tendency to sedimentation, slow drying of the slurry, and poor wettability of wax clusters [10]. To address these issues, additional components such as polymers, surfactants, defoamers, anti-gelling agents, and ceramic shell drying indicators are added to the slurry, and sometimes to the binder [17]. Despite these drawbacks, ceramics made with advanced hydrolyzed ethyl silicate or a colloidal silica binders exhibit similar strengths [5].

The viscosity of the slurry for the first ceramic shell layer is a crucial factor affecting the surface quality of the mold [18, 19]. An increase in dynamic viscosity of the slurry results in thicker layer, which can complicate drying and lead to mold cracking [20]. The dynamic viscosity of the slurry is influenced by factors such as temperature, stucco fraction and stucco particle size distribution [20].

Strength is the primary property of the ceramic mold. The mold must be sufficiently robust before firing in order to allow pattern removal, and after firing in order to bear the weight of the liquid metal. However, the strength after firing should not be excessive to avoid hot tearing in alloys and to facilitate mold knockout [3, 21]. The strength of the shell mold is directly dependent on slurry properties, as well as the technology employed in slurry preparation and application. If there is insufficient wetting of the slurry filler with the binder, the shells may not reach the required strength and could crack [19].

The use of colloidal silica binders without any additives results in very low strength of the green (unfired) molds, which are prone to cracking during wax pattern removal and other processes. For this reason, liquid polymer additives, such as either latex (for alkaline binders) or polyvinyl acetate (PVA) based (for acidic binders) are commonly used [21, 22].

The gas permeability of the ceramic mold is affected by the particle size of the stucco used. The permeability of the first layer is particularly important [22]. Therefore, it is crucial to examine the viscosity of the slurry and the strength of ceramic mold samples made using stuccos with varying particle size distributions.

Currently, domestic manufacturers utilize casting equipment from the leading global vendors. The equipment is designed to work with imported binders exclusively. However, high-quality binders from domestic vendors are available on the market. The aim of this study is to evaluate the viscosity of the slurries made with domestic colloidal silica binders and analyze the impact of refractory particle size in stucco on the mechanical properties and surface finish of ceramic molds.

Materials and methods

Analysis of binder properties. Preparation of slurries and viscosity measurements

We utilized four types of aqueous binders manufactured in Russia, namely VT13-02U (Vakuumtech, Moscow), Stavroform VS (Polymet, Togliatti), UltraCast One+, and UltraCast Prime (Technopark, Moscow), to prepare the slurries. To determine the density of the binders, we weighed on analytic scale a known volume (50 mL) of each binder using a burette. The pH of the binders was measured using a HI83141 pH meter from Hanna Instruments (USA).

The slurries were prepared by mixing 400 mL of the aforementioned binders with 1 kg of FSP with a particle size of 0.045 mm (Kefron, Russia). After mixing, the slurry was allowed to incubate for 24 h to ensure proper wetting of the FSP particles with

the binder and to release any trapped air. Then it was stirred for 10 min to uniformly distribute the FSP particles. The viscosity of the slurry was measured and after the 50 mL of binder was added. This enable us to determine the viscosity of the slurry containing 400, 450, 500, 550, and 600 mL of the binder per 1 kg of FSP.

To measure the viscosity of the slurries, we used two different viscosity measurements procedures.

1. The relative viscosity was estimated using a VZ-4 capillary tube viscometer (nozzle diameter and cup height: 4 mm) according to state standard GOST 9070-75. The relative viscosity is directly proportional to the slurry flow time. Each measurement was repeated 2—3 times.

2. The dynamic viscosity was measured using a DV2TLV rotary viscometer (Brookfield, USA). The slurry (binder) was poured into a 400 mL glass beaker. We used LV-1 (#61) and LV-3 (#63) spindles for a 15—400)·10^3 mPa·s viscosity range [23]. The spindle rpm ranged from 10 to 200.

Particle size measurements of fused silica powder and fused silica refractory

We conducted an estimation of the particle size distribution of FS by employing a set of sieves in accordance with GOST 29234.3-91 state standards. Specifically, a 01412 vibration sieve (Litmashpribor Usman Foundry Equipment Company, Russia) was utilized for this purpose.

To determine the particle size distribution of the FSP we used microphotographs taken with a Vega 3 SBH scanning electron microscope (Tescan, Czech Republic). We measured particle areas on the microphotographs with the aid of ImageJ 1.52a software (National Institutes of Health, USA). This software computed particle diameter and volume based on their areas. After that, we determined the volume fraction of particles within each size range.

Manufacturing the samples. Three-point bending tests. Roughness measurements

We prepared ceramic square samples for bending tests [24]. The slurry was made with VT13-02U, Stavroform VS, UltraCast One+, and UltraCast Prime binders with 20, 40, and 60 seconds relative viscosity, as measured by the VZ-4 viscometer. The wax pattern made of the paraffin/stearin 50/50 compound (Fig. 1) was coated with the slurry and dust by stucco of fused silica grades FS 0.25—0.4 mm, FS 0.4—0.6 mm, and FS 0.5—1.0 mm (Kefron, Russia). The applied slurry and stucco were removed from the upper face (surface *A*) of the wax pattern with a knife. The ceramic sample was formed in cavity *B*. Each layer was air-dried at room temperature for 2 h. The number of layers varied from 5 to 9 depending on the slurry viscosity and the FS particle size.

The wax pattern was removed in boiling water. We produced six 40±1×20±1×8±1 mm ceramic samples for each FS particle size range (FS 0.25—0.4 mm; FS 0.4—0.6 mm, and FS 0.5—1.0 mm grades) and relative viscosity of the slurry (20, 40 and 60 s). Three of the six samples produsd as a single

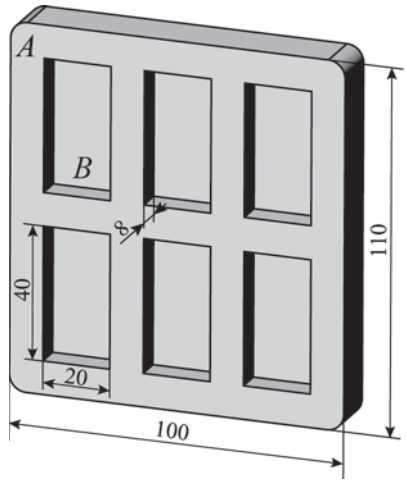

Fig. 1. Wax pattern for the production of ceramic samples

Рис. 1. Восковая модель для получения керамических образцов

Fig. 2. Ceramic samples for the mechanical tests after firing

Рис. 2. Керамические образцы после прокалки для механических испытаний

batch underwent firing as follows: heated to 900 °C over 1.5 h, held at this temperature for 2 h, and cooled in the furnace with the door open. The remaining three samples were tested before firing ("green") after air drying for 24 h. Fig. 2 illustretes the samples after firing.

We employed a 5966 universal testing machine (Instron, USA) to conduct three-point bending tests in accordance with the ASTM C1161-13 standard. The distance between the supports was set at 21 mm, and the loading rate was maintained at 1 mm/min.

The surface roughness of the samples was assessed using an M300C profilometer (MarSurf, Germany).

Results and discussion

Properties of the binders

The table presents the density and pH levels of the binders. The density values are nearly identical, falling between 1.15—1.16 g/cm^3. The pH values, which range from 9.8 to 10.6, confirm the alkaline nature of the binders. It is worth noting that the measured density and pH values fall within the ranges specified by the manufacturers.

The density and pH of investigated binders

Плотность и величина pH исследуемых связующих

Binder	Density, g/cm^3	pH
VT13-02U	1.16	9.8
Stavroform VS	1.15	10.2
UltraCast One+	1.16	10.6
UltraCast Prime	1.15	10.3

Particle Size Distribution of the FSP and FS

In Fig. 3, *a* the particle volume fractions of the FSP 0.045 mm grade fused silica powder are presented. The particles exhibit a size of 0 to 60 μm. Their size distribution is irregular, deviating from a normal distribution.

In Fig. 3, *b* the sieving residue for the FS are depicted. The FS 0.25—0.4 mm and FS 0.4—0.6 mm

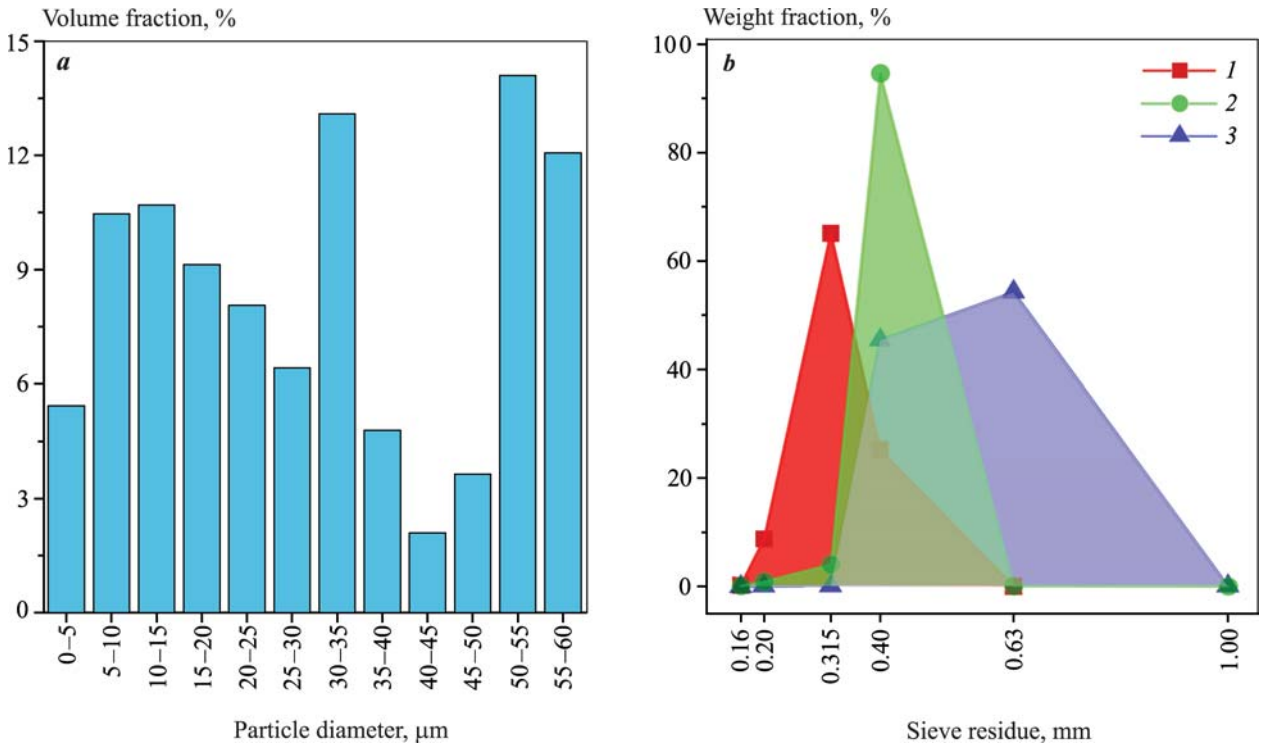

Fig. 3. Distribution of FSP 0.045 mm silica powder particles by size (***a***) and fused silica sieve analysis results (***b***)

1 – FS 0.25–0.4 mm, ***2*** – FS 0.4–0.6 mm, ***3*** – FS 0.5–1.0 mm

Рис. 3. Распределение частиц по размерам в пылевидном плавленом кварце ПКП 0,045 мм (***a***) и результаты рассева плавленого кварца на ситах (***b***)

1 – ПК 0,25–0,4 мм, ***2*** – ПК 0,4–0,6 мм, ***3*** – ПК 0,5–1,0 мм

grade refractories show that the bulk of the material is retained on the 0.315 and 0.4 mm sieves, which conforms to the FS specifications. For the 0.5—1.0 mm fused silica, its particles are distributed almost equally between the 0.4 and 0.63 mm sieves and the measured values are in line with the FS 0.5—1.0 mm grade specifications.

Slurry and binder viscosity measurements

In Fig. 4 the slurry viscosity is plotted against the binder content (in mL) per 1 kg of fused silica powder, with the viscosity of the binders indicated. The viscosity was measured using a rotational viscometer. The viscosity of the binders increased as the spindle rpm increased, indicating that they behave like non-Newtonian fluids. No significant difference was detected between the viscosities of the binders, which fell within the range of 6—8 mPa·s for 75 rpm (v), and 11—13 mPa·s for v = = 200 rpm. It is known that binders are non-Newtonian fluids, and their viscosity decreases as the shear rate increases [20]. However, we observed an inverse relationship, which may be attributed to the flow turbulence at high spindle speeds.

It is known that a higher binder viscosity leads to a higher slurry viscosity for the same filler/binder ratio [25]. In our study, the viscosities of the binders were almost the same. The authors of [20] investigated the viscosity of the Ludox SK binder using a similar method, and obtained a fairly close value of 7 mPa·s. As shown in Fig. 4, the slurry viscosity remains almost unaffected by the spindle speed, except for the low range (up to 50 rpm), indicating that the slurries behave like Newtonian fluids.

In order to determine the slurry viscosity, the average viscosity over the range of 50—200 rpm was taken since the viscosity did not change much in this range. Fig. 5, *a* illustrates the relationship between the viscosity of the slurries and the binder content, expressed in mL per 1 kg of FSP. It can be observed that the slurries containing the majority of the binders have comparable viscosities. The viscosity versus binder content relationship follows a logarithmic trend, as shown by the nearly linear curve plotted in a logarithmic scale. However, the VT13-02U grade binder exhibits a steeper curve, and slightly lower viscosity values. It is worth noting that all the binders have a similar SiO_2 content, and any variations in the viscosity of the slurries could be due the addition of polymers or other additives to the binder [26].

The cause of the viscosity variations could not be reliably determine. Studies [27, 28] have suggested that as the mixing time increases, the slurry viscosity also increases due to water evaporation into the environment and the friction heat generated in the slurry and in the mixer. Temperature and humidity fluctuations in the test room may also contribute to the viscosity differences, particularly for colloidal silica binder slurries, as they lead to non-uniform evaporation of water and non-uniform viscosity changes. Typically, the differences in the slurry viscosities are attributed to the densities and viscosities of the binders, with the latter having a greater impact on the viscosity of the slurry mixture than the density [25]. However, in this study, the viscosities and densities of the binders are very similar, indicating that the viscosities of the slurries containing different binders will be approximately equal.

It is widely recognized that the viscosity of the slurry increases in proportion with the ratio of filler to binder [25]. Specifically, when the binder content is increased from 400 to 600 mL per 1 kg of fused silica powder, the resulting viscosity drops from 550—870 to 60—80 mPa·s, respectively, indicating tenfold decrease. This viscosity level determines the velocity and uniformity of the slurry's flow over a pattern or underlying ceramic layer [17], and higher viscosity levels produce a thicker first layer [25].

Relative viscosity, as measured by the slurry flow time through a nozzle of a specific diameter, is a standard metric used in the casting industry. Fig.5, *b* displays the relative viscosity values of slurries measured using the VZ-4 viscometer. The viscosities of all slurries are near similar, with the exception of the VT13-02U binder, which was also observed in rotary viscometer readings. However, in this case, the rotary viscometer readings were lower than those of the other binders, whereas the VZ-4 viscometer readings were significantly higher.

We can infer from these observations that the relationship between viscosity and binder content (in mL) per 1 kg of FSP is non-linear. At higher binder contents, the rate of viscosity change decreases. Increasing the binder content from 400 to 600 mL per 1 kg of fused silica powder leads to a viscosity drop from ~380 to ~16 s, respectively, or about a 24-fold decrease.

Casting specifications typically call for relative viscosity levels between 20 and 70 s, depending on the layer number. Higher viscosity levels are required for the first layers, with viscosity levels decreasing in subsequent layers. A high viscosity results in a thicker and denser layer, which is particularly important when wetting is insufficient during the application of the first

layer [25, 27]. Additionally, high slurry viscosity provides a smooth finish for the first layer [27]. Previous research has shown [18] that when the relative viscosity of a slurry falls below 35 s, surface defects occur in the ceramic mold, regardless of the fused silica stucco grain size. To achieve a defect-free ceramic surface, it is necessary to increase slurry viscosity and decrease the stucco particle size.

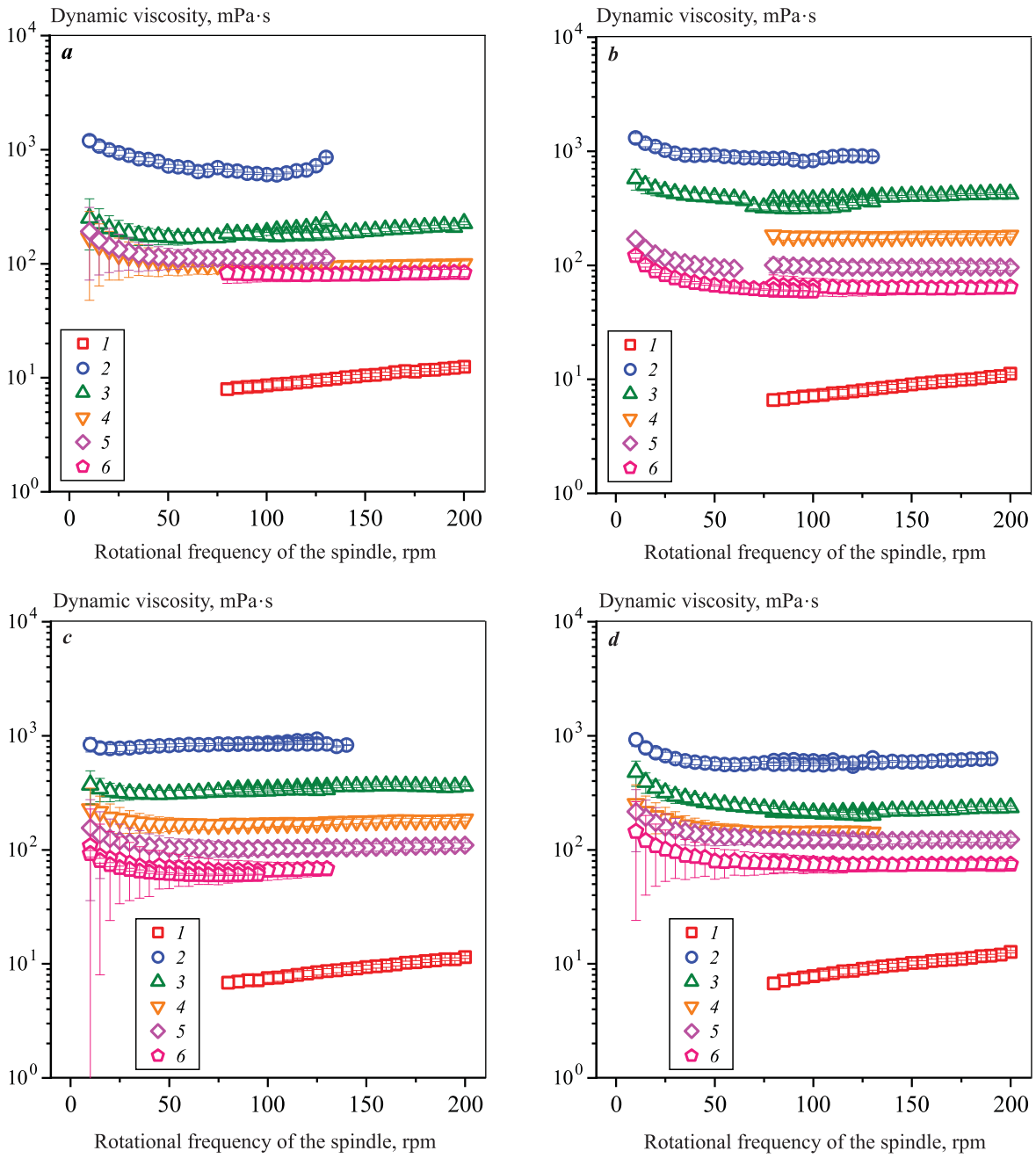

Fig. 4. Viscosity of slurry prepared with binders: VT13-02U (***a***), Stavroform VS (***b***), UltraCast One+ (***c***), UltraCast Prime (***d***), depending on the amount of binder

1 – binder without refractory, ***2*** – 400 mL, ***3*** – 450 mL, ***4*** – 500 mL, ***5*** – 550 mL, ***6*** – 600 mL
The amount of binder is given per 1 kg of silica powder

Рис. 4. Вязкость суспензии, приготовленной на связующих ВТ13-02У (***a***), Ставроформ ВС (***b***), UltraCast One+ (***c***) и UltraCast Prime (***d***), в зависимости от количества связующего

1 – связующее без наполнителя, ***2*** – 400 мл, ***3*** – 450 мл, ***4*** – 500 мл, ***5*** – 550 мл, 6 – 600 мл
Количество связующего приведено на 1 кг пылевидного кварцевого микропорошка

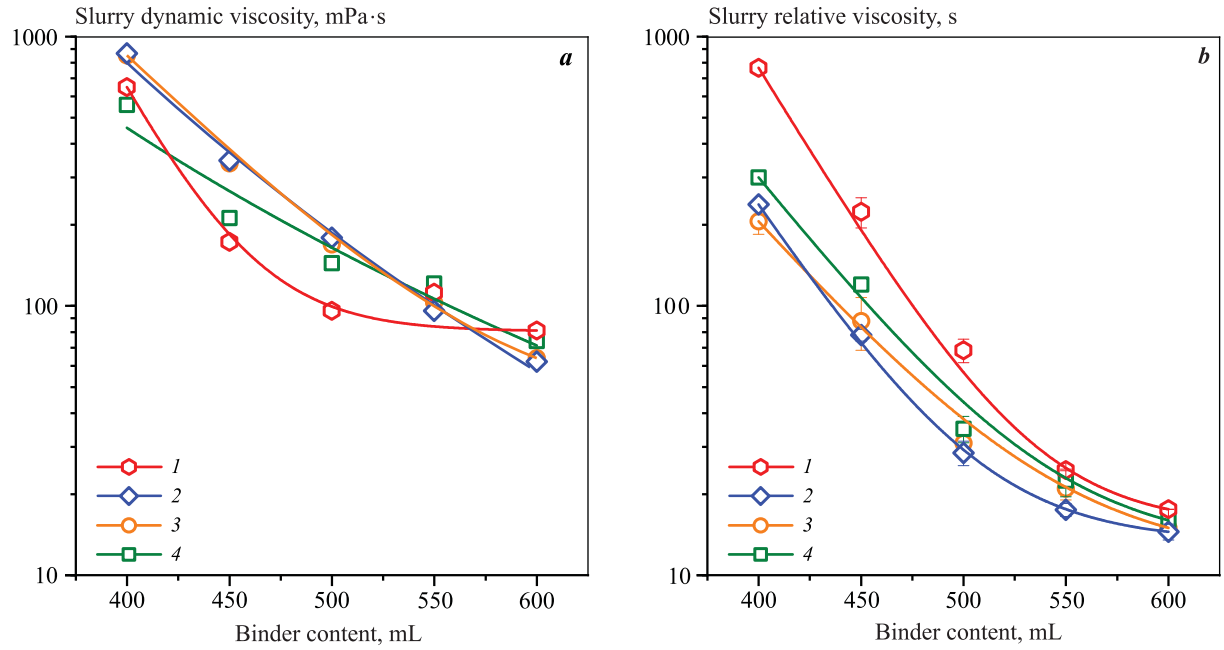

Fig. 5. The viscosity of the slurry, determined using the rotational viscosimeter (***a***) and a VZ-4 viscosimeter (***b***), depending on the content of the binder per 1 kg of silica powder

1 – VT13-02U, ***2*** – Stavroform VS, ***3*** – UltraCast One+, ***4*** – UltraCast Prime

Рис. 5. Вязкость суспензии, определенная с помощью ротационного вискозиметра (***a***) и вискозиметра ВЗ-4 (***b***), в зависимости от содержания связующего на 1 кг микропорошка

1 – ВТ13-02У, ***2*** – Ставроформ ВС, ***3*** – UltraCast One+, ***4*** – UltraCast Prime

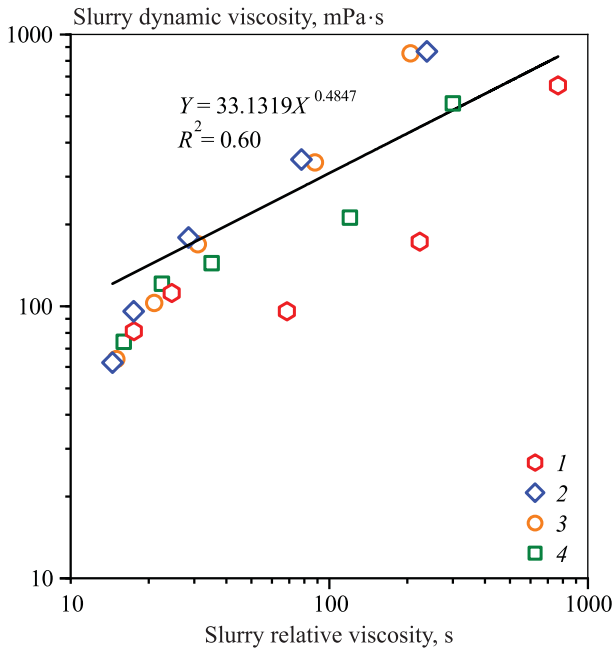

Fig. 6. Comparison of the viscosity of the slurry, determined using the VZ-4 viscosimeter (X) and a rotational viscosimeter (Y)

1 – VT13-02U, ***2*** – Stavroform VS, ***3*** – UltraCast One+, ***4*** – UltraCast Prime

Рис. 6. Соотношение между значениями вязкости суспензии, определенными с помощью вискозиметра ВЗ-4 (X) и ротационного вискозиметра (Y)

1 – ВТ13-02У, ***2*** – Ставроформ ВС, ***3*** – UltraCast One+, ***4*** – UltraCast Prime

A binder content ranging from 450 to 600 mL per 1 kg of FSP produces a slurry with a relative viscosity within the recommended range (20—70 s).

Since we have measured both the relative viscosity (using the VZ-4 viscometer) and the dynamic viscosity (using the rotary viscometer), it is worthwhile to examine the correlation between these two parameters for the slurries investigated. Fig. 6 displays the curve of dynamic viscosity (measured in mPa·s) versus relative viscosity (in seconds), as well as the equation that

can be used to convert relative viscosity (X) to dynamic viscosity (Y). The equation shown in Fig. 6 can be simplified to:

$$Y = 33X^{1/2}.$$

Three-point bending tests and roughness tests results

The flexural strength values of the ceramic samples after drying and firing are presented in Fig. 7. The impact of slurry viscosity and fused silica particle size on the flexural strength was evaluated for each binder. In most cases, the strength of the samples increased with an increase in the slurry viscosity and decrease in FS particle size. Decreasing the size of the FS particles facilitated an increase in the contact area between the stucco particles, thereby improving strength.

Regarding the effects of slurry viscosity, it appears that an increase in viscosity results in a greater amount of binder remaining on the previous layer before the

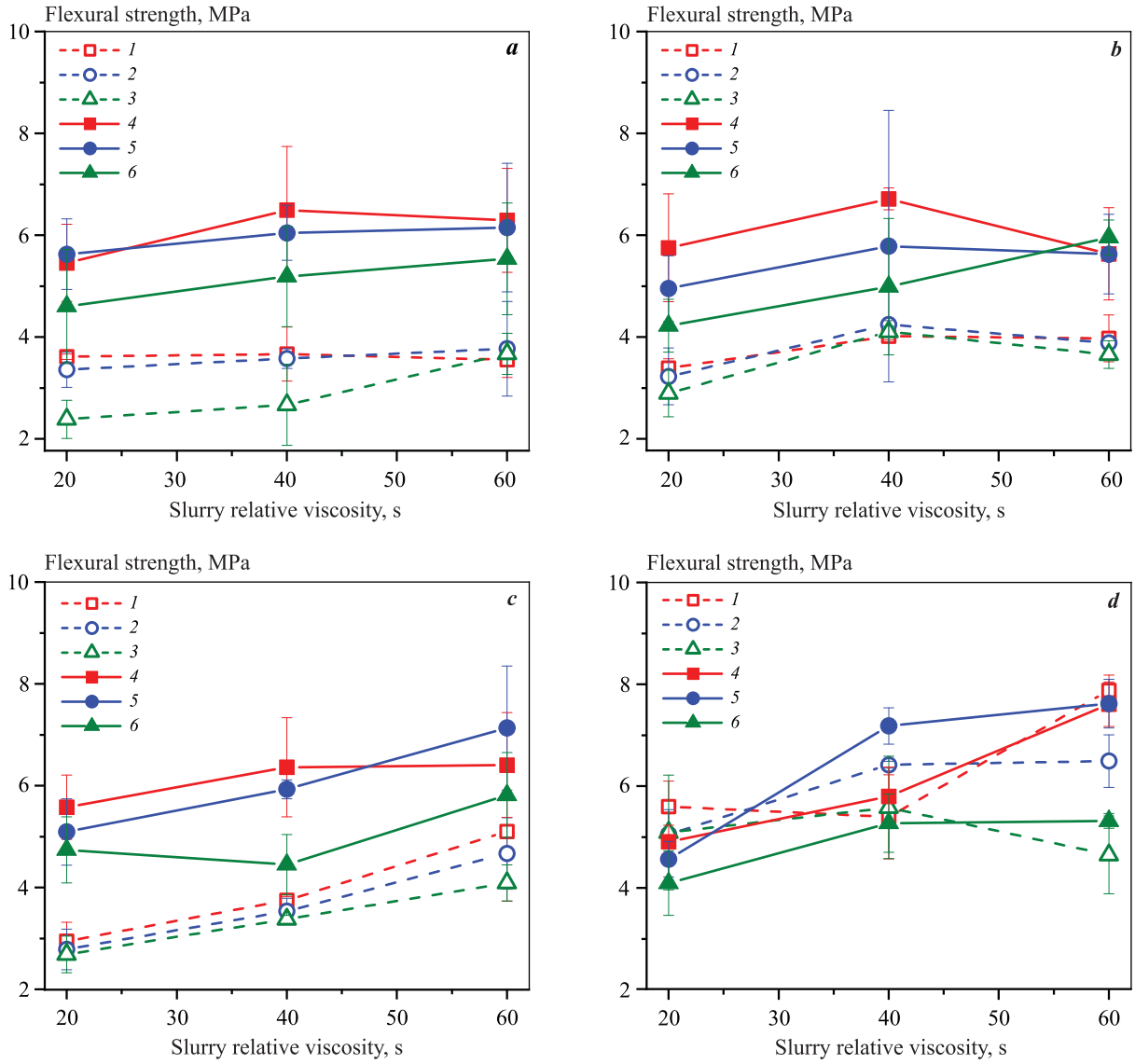

Fig. 7. Flexural strength of ceramic shell specimens obtained with binders: VT13-02U (***a***), Stavroform VS (***b***), UltraCast One+ (***c***), UltraCast Prime (***d***) as dried (***1–3***) and after firing (***4–6***)

Fused silica fraction: FS 0.25–0.4 mm (***1***, ***4***), FS 0.4–0.6 mm (***2***, ***5***), FS 0.5–1.0 mm (***3***, ***6***)

Рис. 7. Прочность на изгиб керамических образов, полученных на связующих ВТ13-02У (***a***), Ставроформ ВС (***b***), UltraCast One+ (***c***), UltraCast Prime (***d***), в состоянии после сушки (***1–3***) и прокалки (***4–6***)

Фракция плавленого кварца: ПК 0,25–0,4 мм (***1***, ***4***), ПК 0,4–0,6 мм (***2***, ***5***), ПК 0,5–1,0 мм (***3***, ***6***)

stucco application. This leads to an increase in the volume fraction of solidified binder relative to the stucco content in the ceramcs. A previous study by authors [29] has also reported an increase in ceramic strength with an increase in slurry viscosity.

Fig. 8 depicts the flexural strength of ceramic samples containing various binders at an slurry viscosity of 40 s and FS 0.4—0.6 mm fused silica grade, after drying and firing. For samples obtained with VT13-02U, Stavroform VS, and UltraCast One+ binders, the flexural strength after drying ranges from 3.5 to 4.3 MPa, and after firing, 5.8 to 6.1 MPa, resulting in a 1.5x increase due to ceramic firing. Typically, the strength of "green" ceramics is approximately half of that after firing [17, 18, 25], which is consistent with our results and those reported in previous studies [10, 17, 24].

It is noteworthy that the strength before firing is primarily determined by the wax penetration into small defects and pores as wax is not entirely removed by dewaxing in boiling water [30]. We used the paraffin/stearin 50/50 wax; high strength filled waxes may result in higher strength of the green sample.

The properties of ceramics made with the UltraCast Prime binder are slightly different. The strengths after drying and firing are 6.4 and 7.2 MPa, respectively, which is higher both before and after firing in comparison to ceramics made with other binders. Previous studies [26] suggest that adding a polymer to the binder results in higher flexural strength of the "green" ceramics equivalent of that of the fired sample. The higher strength of the ceramics containing the UltraCast Prime binder is attributed to the addition of a polymer into binder to increase the strength before firing.

The most common flexural strength values for ceramic molds are 3—10 MPa [10, 17, 24, 31]. The tested binders generally provide the required strength values for ceramic molds even before firing, with the exception of slurries with low relative viscosity (~20 s) and coarse fused silica stucco (FS 0.5—1.0 mm).

Increasing the mold firing temperature can result in the formation of cristobalite [14], which may increase the strength of the ceramics but also increase the thermal expansion coefficient, making it undesirable [14]. Another method to increase the strength of ceramics (from 15 to 40 MPa) is by adding alumina powder as a filler to the slurry, along with alumina refractory as the stucco [9].

In terms of surface roughness the ceramic samples obtained with the VT13-02U and Stavroform binders exhibited similar values, with R_z = 25 ± 2 and 26 ± 3 μm, respectively, falling within the confidence interval. The ceramic samples obtained using the UltraCast Prime and UltraCast One+ binders dispayed lower R_z values: 15 ± 1 and 21 ± 2 μm, respectively.

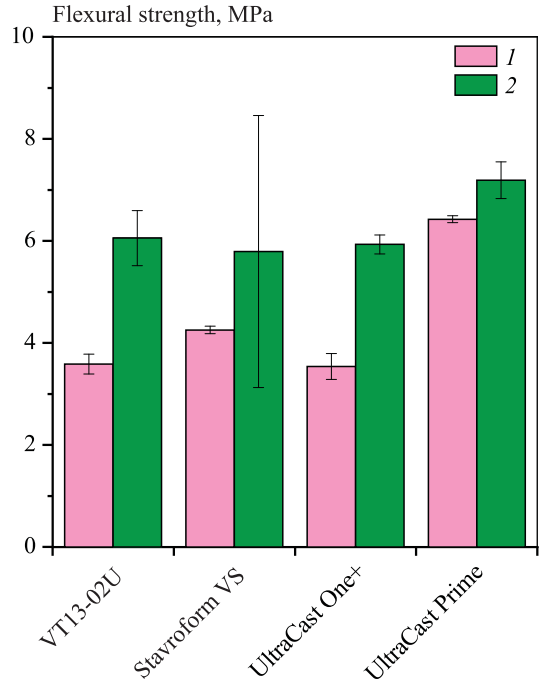

Fig. 8. The flexural strength of ceramic shell samples obtained with various binders after drying (***1***) and firing (***2***) at a slurry viscosity of 40 s and a fused silica fraction FS 0.4—0.6 mm

Рис. 8. Прочность на изгиб керамических образов, полученных на различных связующих, в состояниях после сушки (***1***) и прокалки (***2***) при вязкости суспензии 40 с и фракции плавленого кварца ПК 0,4—0,6 мм

The domestic colloidal silica binders exhibit similar properties to hydrolyzed ethyl silicate binders, but with the added benefits of being non-flammable and environmentally friendly [5, 7—9, 12]. This enables their use in the production of ceramic shells for making castings on automated and robotic lines, after correction of technological parameters, which are selected for each binder separately.

Conclusion

The study focused on the viscosity of the slurries made with colloidal silica binders (VT13-02U, Stavroform VS, UltraCast One+, and UltraCast Prime) and fused silica powder, as well as on the flexural strength of the ceramic samples produced from these

slurries with fused silica stucco. The results are as follows.

1. The slurries are close to Newtonian fluids with similar viscosities. Specifically, at binder contents of 400 and 600 mL per 1 kg of fused silica powder, the average dynamic viscosity is ~732 and ~70 mPa·s, respectively.

2. The increase the binder content from 400 to 600 mL per 1 kg of fused silica powder results in a significant decrease in relative viscosity from ~380 to ~16 s, respectively (up to 24 times). The relationship between the relative (X) and dynamic (Y) viscosities can be expressed by the following equation: $Y = 33X^{1/2}$.

3. The flexural strengths of the samples which contain the binders VT13-02U, Stavroform VS, and UltraCast One+ are similar, with values ranging from 3.5 to 4.3 MPa after drying and 5.8 to 6.1 MPa after firing. For the UltraCast Prime binder, the flexural strengths after drying and firing are 6.4 and 7.2 MPa, respectively. The high strength observed in "green" state of the UltraCast Prime binder may be due to the presence of polymer additives in the binder.

4. The strength of the samples, both after drying and firing, increases with increasing slurry viscosity and decreasing fused silica stucco particle size.

5. The surface roughness of the ceramic samples containing the VT13-02U and Stavroform binders was found to be $R_z = 25 \pm 2$ and 26 ± 3 μm, respectively. In contrast, the ceramic samples made with the UltraCast Prime and UltraCast One+ binders exhibited lower surface roughness values of 15 ± 1 and 21 ± 2 μm, respectively.

References

1. Kanyo J.E., Schaffцner S., Uwanyuze R.S., Leary K.S. An overview of ceramic molds for investment casting of nickel superalloys. *Journal of the European Ceramic Society*. 2020;40(15):4955—4973. https://doi.org/10.1016/j.jeurceramsoc.2020.07.013
2. Novokreshchennykh E.N., Myrzina K.M., Ordin D.A., Vakhrushev V.V., D'yakov M.S., Poilov V.Z., Uglev N.P. Research and selection of reagents in the development of compositions of colloidal silica binders for investment casting ceramics. *Mezhdunarodnyi nauchno-issledovatel'skii zhurnal*. 2017;(10):14—18. (In Russ.).
Новокрещенных Е.Н., Мырзина К.М., Ордин Д.А., Вахрушев В.В., Дьяков М.С., Пойлов В.З., Углев Н.П. Исследование и выбор реагентов при разработке составов водно-коллоидных связующих для литейных керамик. *Международный научно-исследовательский журнал*. 2017;(10):14—18.
3. Pattnaik S., Karunakar D.B., Jha P.K. Developments in investment casting process — A review. *Journal of Materials Processing Technology*. 2012;212:2332—2348. https://doi.org/10.1016/j.jmatprotec.2012.06.003
4. Bazylev V.A., Chernomas V.V. Application of Armosil® binder for the production of shell molds in the lost foam casting. In: *Materials of the 46th Scientific and Technical Conference of Students and Postgraduates* (Komsomol'sk-na-Amure, 1–15 Apr. 2016). Komsomol'sk na Amure: Komsomol'sk-na-Amure State Technical University, 2016. P. 47–49. (In Russ.).
Базылев В.А., Черномас В.В. Применение связующего «Армосил®» для изготовления оболочковых форм в литье по выжигаемым моделям. В сб: *Материалы 46-й научно-технической конференции студентов и аспирантов* (г. Комсомольск-на-Амуре, 1–15 апр. 2016 г.). Комсомольск на Амуре: Комсомольский-на-Амуре государственный технический университет, 2016. С. 47—49.
5. Vdovin K.N., Feoktistov N.A., Ovchinnikov M.V., Pinaev A.S. The use of universal water-based coloidal silica binders for the manufacture of ceramic investment casting molds. *Tekhnologii metallurgii, mashinostroeniya i materialoobrabotki*. 2019;(18):149—154. (In Russ.).
Вдовин К.Н., Феоктистов Н.А., Овчинников М.В., Пинаев А.С. Применение универсальных кремнеземных связующих на водной основе для изготовления керамических форм для литья по выплавляемым моделям. *Технологии металлургии, машиностроения и материалообработки*. 2019;(18):149—154.
6. Demenok A.O., Ganeev A.A., Demenok O.B., Bakerin S.V., Kulakov B.A. Development of resource-saving technology for production of large-size castings from titanium alloys. *Vestnik Yuzhno-Ural'skogo gosudarstvennogo universiteta. Seriya: Metallurgiya*. 2015;15(2):20—25. (In Russ.).
Деменок А.О., Ганеев А.А., Деменок О.Б., Бакерин С.В., Кулаков Б.А. Разработка ресурсосберегающей технологии получения крупногабаритных отливок из титановых сплавов. *Вестник Южно-Уральского государственного университета. Серия: Металлургия*. 2015;15(2):20—25.
7. Vdovin K.N., Feoktistov N.A. Ovchinnikova M.V. Technology of molding with the use of colloidal silica binders in investment casting. *Aktual'nye problemy sovremennoi nauki, tekhniki i obrazovaniya*. 2020;11(1):29—31. (In Russ.).
Вдовин К.Н., Феоктистов Н.А. Овчинникова М.В. Технология формообразования с применением связующих на водной основе в литье по выплавляемым моделям. *Актуальные проблемы современной науки, техники и образования*. 2020;11(1):29—31.

8. Shutova O.O., Leushina L.I. Improving the Environmental Safety of Precision Aluminum Casting Technology at an Aircraft Construction Enterprise. In: *Metallurgy of the XXI century through the eyes of the young*. A collection of reports of the V International Scientific and Practical Conference of Young Scientists and Students (22 may 2019). Donetsk: Donetsk National Technical University, 2019. P. 342–344. (In Russ.).
Шутова О.О., Леушина Л.И. Повышение экологической безопасности технологии точного алюминиевого литья на предприятии авиастроения. В сб: *Металлургия XXI столетия глазами молодых:* Сборник докладов V Международной научно-практической конференции молодых ученых и студентов (22 мая 2019 г.). Донецк: Донецкий национальный технический университет, 2019. С. 342—344.
9. Mukhamadeev I.R., Demenok O.B., Ganeev A.A., Pavlinich S.P., Alikin P.V. Selection of water-based colloidal silica binders for shell molds of titanium alloys investment casting. *Vestnik Yuzhno-Ural'skogo gosudarstvennogo universiteta. Seriya: Metallurgiya*. 2015;15(3):95—104. (In Russ.).
Мухамадеев И.Р., Деменок О.Б., Ганеев А.А., Павлинич С.П., Аликин П.В. Выбор связующих на водной основе для оболочковых форм литья по выплавляемым моделям титановых сплавов. *Вестник Южно-Уральского государственного университета. Серия: Металлургия*. 2015;15(3):95—104.
10. Vorfolomeev M.S. Features of the production of corundum ceramic molds for investment casting based on an inorganic aqueous colloidal silica binder. *Liteinoe proizvodstvo*. 2021;(11):16—18. (In Russ.).
Ворфоломеев М.С. Особенности изготовления корундовых керамических форм по выплавляемым моделям на основе неорганического водного связующего. *Литейное производство.* 2021;(11):16—18.
11. Kozlov V.V., Varfolomeev M.S. Features of Manufacturing Technology of Corundum Casting Molds Based on Coloidal silica Binders in Investment Casting. *Liteishchik Rossii*. 2020;(10):32—35. (In Russ.).
Козлов В.В., Варфоломеев М.С. Особенности технологии изготовления корундовых литейных форм на основе зольных связующих в литье по выплавляемым моделям. *Литейщик России*. 2020;(10):32—35.
12. Ordin D.A., Novokreshchennykh E.N., Poilov V.Z., Uglev N.P. Transfer of investment casting technology in aircraft construction to ceramics produced with colloidal silica binders: Review of the studies carried out. *Vestnik PNIPU*. 2016;(3):59—74. (In Russ.).
Ордин Д.А., Новокрещенных Е.Н., Пойлов В.З., Углев Н.П. Перевод технологии литья по выплавляемым моделям в авиастроении на керамику, полученную с использованием связующих на водной основе: Обзор выполненных исследований. *Вестник ПНИПУ.* 2016;(3):59—74.
13. Chernov V.P., Selivanova E.A. Investigation of the properties of slurries used for investment casting ceramic molds. *Vestnik MGTU im. G.I. Nosova*. 2010;(3):21—25. (In Russ.).
Чернов В.П., Селиванова Е.А. Исследование свойств огнеупорных суспензий, используемых для керамических форм при литье по выплавляемым моделям. *Вестник МГТУ им. Г.И. Носова*. 2010;(3):21—25.
14. Kanyo J.E., Schaffqner S., Uwanyuze R.S., Leary K.S. An overview of ceramic molds for investment casting of nickel superalloys. *Journal of the European Ceramic Society*. 2020;40:4955—4973.
https://doi.org/10.1016/j.jeurceramsoc.2020.07.013
15. D'yachkov V.N., Paramonov A.M., Nikitin K.V. Improving the technology for producing castings by the investment casting method. *Liteishchik Rossii*. 2012;(5):32—33. (In Russ.).
Дьячков В.Н., Парамонов А.М., Никитин К.В. Совершенствование технологии получения отливок способом ЛВМ. *Литейщик России*. 2012;(5):32—33.
16. Dubrovin V.K., Kulakov B.A., Karpinskii A.V., Goikhenberg Yu.N. Selection of molding materials for investment casting. *Liteishchik Rossii*. 2015;(7):12—15. (In Russ.).
Дубровин В.К., Кулаков Б.А., Карпинский А.В., Гойхенберг Ю.Н. Выбор формовочных материалов для литья по разовым моделям. *Литейщик России*. 2015;(7):12—15.
17. Petrov A.Yu., Trubkina S.N., Gilev V.I., Vertyukh S.S., Ovchinnikov M.V. Universal water based colloidal silica binders. *Liteishchik Rossii*. 2018;(6):9—13. (In Russ.).
Петров А.Ю., Трубкина С.Н., Гилев В.И., Вертюх С.С., Овчинников М.В. Универсальные кремнезольные связующие материалы на водной основе. *Литейщик России.* 2018;(6):9—13.
18. Yusipov R.F., Dem'yanov E.D., Vinogradov V.Yu., Paremskii I.Ya., Airapetyan A.S. Method for evaluating the surface quality of the facecoat layer of an investment casting mold. *Liteinoe proizvodstvo*. 2021;(8):23—26. (In Russ.).
Юсипов Р.Ф., Демьянов Е.Д., Виноградов В.Ю., Паремский И.Я., Айрапетян А.С. Метод оценки качества поверхности лицевого слоя формы литья по выплавляемым моделям. *Литейное производство*. 2021;(8):23—26.
19. Ferenc-Dominik J., Matysiak H., Kurzydlowski K.J. Organic viscosity modifiers for controlling rheology of ceramic slurries used in the investment casting. *Advances in Science and Technology*. 2010;70:102—107.
https://doi.org/10.4028/www.scientific.net/AST.70.102

20. Kolczyk J., Zych J. Rheological properties of ceramic slurries with colloidal binders used in the investment casting technology. *Metalurgija*. 2013;52:55—58.
21. Jones S., Yuan C. Advances in shell moulding for investment casting. *Journal of Materials Processing Technology*. 2003;135:258—265. https://doi.org/10.1016/S0924-0136(02)00907-X
22. Jones S., Jolly M.R., Lewis K. Development of techniques for predicting ceramic shell properties for investment casting. *British Ceramic Transactions*. 2002;101:106—113. https://doi.org/10.1179/096797802225003316
23. AMETEK Brookfield. LV Standard Spindles. URL: https://store.brookfieldengineering.com/lv-standard-spindles/?_pos=1&_sid=d76593138&_ss=r (accessed: 02.12.2022).
24. Li K., Liu X.-D., Du Z.-X., Li Y.-F. Bending strength and fracture surface topography of natural fiber-reinforced shell for investment casting process. *China Foundry*. 2016;13:211—216. https://doi.org/10.1007/s41230-016-5100-4
25. Zhao E., Kong F., Chen Y., Chen R., Chen Y. Characterization of zirconia-based slurries with different binders for titanium investment casting. *China Foundry*. 2012;9:125—130.
26. Venkat Y., Choudary K.R., Das D.K., Pandey A.K., Singh S. Ceramic shell moulds with zircon filler and colloidal silica binder for investment casting of shrouded low-pressure turbine blades. *Ceramics International*. 2020;46:26572—26580. https://doi.org/10.1016/j.ceramint.2020.07.125
27. Vyas A.V., Pandya M.P., Sutaria M.P. Effect of mixing proportion and mixing time on primary slurry retention and surface roughness of investment casting shells. *IOP Conf. Series: Materials Science and Engineering*. 2020;872:012094. https://doi.org/10.1088/1757-899X/872/1/012094
28. Bundy J., Viswanathan S. Characterization of zirconia-based slurries with different binders for titanium investment casting. *International Journal of Metalcasting*. 2008;3:27—37. https://doi.org/10.1007/BF03355439
29. Kline D.M. Controlling strength and permeability of silica investment casting molds: Masters Theses. Missouri: Missouri University of Science and Technology, 2010.
30. Lee K., Blackburn S., Welch S.T. A more representative mechanical testing of green state investment casting shell. *Ceramics International*. 2017;43:268—274. http://dx.doi.org/10.1016/j.ceramint.2016.09.149
31. Ivanov V.I., Kazennov S.A., Kurchman B.S. et al. Investment casting (Ed. by Ya.I. Shklennik, V.A. Ozerov). Moscow: Mashinostroenie, 1984. (In Russ.).
Иванов В.И., Казеннов С.А., Курчман Б.С. и др. Литье по выплавляемым моделям (Под общ. ред. Я.И. Шкленника, В.А. Озерова). 3-е изд., перераб. и доп. М.: Машиностроение, 1984.

Information about the authors

Viacheslav E. Bazhenov – Cand. Sci. (Eng.), Assistant Prof., Department of Foundry Technologies and Material Art Working (FT&MAW), National University of Science and Technology "MISIS" (NUST MISIS).
https://orcid.org/0000-0003-3214-1935
E-mail: V.E.Bagenov@gmail.com

Elena P. Kovyshkina – Postgraduate Student, Department of FT&MAW, NUST MISIS.
https://orcid.org/0000-0001-8603-1630
E-mail: Kovyshkina@ic-ltm.ru

Andrey V. Sannikov – Cand. Sci. (Eng.), Assistant Prof., Department of FT&MAW, NUST MISIS.
https://orcid.org/0000-0002-0517-7732
E-mail: a.v.sannikov@inbox.ru

Andrey V. Koltygin – Cand. Sci. (Eng.), Assistant Prof., Department of FT&MAW, NUST MISIS.
https://orcid.org/0000-0002-8376-0480
E-mail: misistlp@mail.com

Denis V. Ten – R & D engineer, Laboratory "Hybrid Nanostructured Materials", NUST MISIS.
https://orcid.org/0000-0003-2513-4462
E-mail: teden92@yandex.ru

Информация об авторах

Вячеслав Евгеньевич Баженов – к.т.н., доцент кафедры литейных технологий и художественной обработки материалов (ЛТиХОМ), Национальный исследовательский технологический университет «МИСИС» (НИТУ МИСИС).
https://orcid.org/0000-0003-3214-1935
E-mail: V.E.Bagenov@gmail.com

Елена Павловна Ковышкина – аспирант кафедры ЛТиХОМ, НИТУ МИСИС.
https://orcid.org/0000-0001-8603-1630
E-mail: Kovyshkina@ic-ltm.ru

Андрей Владимирович Санников – к.т.н., доцент кафедры ЛТиХОМ, НИТУ МИСИС.
https://orcid.org/0000-0002-0517-7732
E-mail: a.v.sannikov@inbox.ru

Андрей Вадимович Колтыгин – к.т.н., доцент кафедры ЛТиХОМ, НИТУ МИСИС.
https://orcid.org/0000-0002-8376-0480
E-mail: misistlp@mail.ru

Денис Васильевич Тен – инженер научного проекта лаборатории «Гибридные наноструктурные материалы», НИТУ МИСИС.
https://orcid.org/0000-0003-2513-4462
E-mail: teden92@yandex.ru

Andrey A. Rizhsky – Laborat. Assistant, Department of FT&MAW, NUST MISIS.
https://orcid.org/0000-0002-6679-7126
E-mail: andrew89.r.a@gmail.com

Vladimir D. Belov – Doc. Sci. (Eng.), Head of Department of FT&MAW, NUST MISIS.
https://orcid.org/0000-0003-3607-8144
E-mail: vdbelov@mail.ru

Evgeniy A. Lazarev – Head Metallurgist, Public Joint Stock Company UEC "Kuznetsov".
E-mail: ea.lazarev@uec-kuznetsov.ru

Андрей Андреевич Рижский – учебный мастер кафедры ЛТиХОМ, НИТУ МИСИС.
https://orcid.org/0000-0002-6679-7126
E-mail: andrew89.r.a@gmail.com

Владимир Дмитриевич Белов – д.т.н., зав. кафедрой ЛТиХОМ, НИТУ МИСИС.
https://orcid.org/0000-0003-3607-8144
E-mail: vdbelov@mail.ru

Евгений Алексеевич Лазарев – главный металлург, ПАО ОДК «Кузнецов».
E-mail: ea.lazarev@uec-kuznetsov.ru

Contribution of the authors

V.E. Bazhenov – conceptualization, analysis of the experimental results, writing of the manuscript.

E.P. Kovyshkina – realization of experiment, analysis of the experimental results.

A.V. Sannikov – realization of experiment, analysis of the experimental results.

A.V. Koltygin – scientific guidance, review and editing of the manuscript.

D.V. Ten – realization of experiment, analysis of the experimental results.

A.A. Rizhsky – realization of experiment, analysis of the experimental results.

V.D. Belov – supervision, review and editing of the manuscript.

E.A. Lazarev – formulation of the aims and objectives of the study, provision of resources.

Вклад авторов

В.Е. Баженов – формирование основной концепции, обработка результатов исследований, написание текста статьи.

Е.П. Ковышкина – проведение экспериментов, обработка результатов исследований.

А.В. Санников – проведение экспериментов, обработка результатов исследований.

А.В. Колтыгин – научное руководство, редактирование текста статьи.

Д.В. Тен – проведение экспериментов, обработка результатов исследований.

А.В. Рижский – проведение экспериментов, обработка результатов исследований.

В.Д. Белов – общее руководство, редактирование текста статьи.

Е.А. Лазарев – формулировка цели и задачи исследования, обеспечение ресурсами.

The article was submitted 09.01.2023, revised 10.03.2023, accepted for publication 13.03.2023

Статья поступила в редакцию 09.01.2023, доработана 10.03.2023, подписана в печать 13.03.2023

UDC 621.777.01
https://doi.org/10.17073/0021-3438-2023-2-29-37

Research article
Научная статья

Structure and strain state of aluminum bars at the initial phase of extrusion

Yu.N. Loginov[1,2], A.V. Razinkin[3], G.V. Shimov[1], T.V. Maltseva[1], N.I. Bushueva[1], E.G. Dymshakova[3], N.A. Kalinina[3]

[1] **Ural Federal University named after the First President of Russia B.N. Yeltsin**
19 Mira Str., Yekaterinburg 620002, Russia

[2] **M.N. Mikheev Institute of Metal Physics of Ural Branch of Russian Academy of Sciences**
18 S. Kovalevskaya Str., Yekaterinburg 620108, Russia

[3] **Kamensk Uralsky Metallurgical Works JSC**
5 Zavodskaya Str., Sverdlovsk region, Kamensk-Uralsky 623405, Russia

✉ Georgy V. Shimov (G.v.shimov@urfu.ru)

Abstract: The structure of insufficiently deformed areas at the non-steady phase of extrusion was studied. The tests at Kamensk Uralsky Metallurgical Works using a 120 MN press and 800 mm dia. container, in order to extrude a 355.6 mm dia. Bar was performed. The bar material is the Al–Mg–Si AD33 aluminum alloy (GOST 4784), similar to ASTM 6061. The percentage reduction was 80 %, and the reduction ratio was 5.06. After that, the macrostructure, microstructure, and average grain size along the radius, mechanical properties at room and elevated temperatures were investigated. It was found that the extruded bar macrostructure is fine-grained, homogeneous, and dense, with no nonmetallic or intermetallic inclusions. The cross-section contained several structures. The central part is weakly deformed preserving the dendritic cell structure inherited from the casting. At the circumference, a streaked structure is formed. Its components are crushed and uniformly distributed. We measured the strength at elevated temperatures and compared the results to the data available in the literature. The tested material strength almost doubled, thus indicating its incomplete softening. The ductility was also performed. The DEFORM-2D software, in order to simulate the low reduction of extrusion was used. The metal at the circumference is exposed to a greater strain from the extrusion beginning. A step-by-step analysis indicated that at the first step, the strain is localized near the die hole. In the second step, a rigid area is formed in the vicinity of the die/container liner interface. The circumference layer of metal with a 1.75–2.00 reduction of area is formed. At the bar center, this range is 0.75–1.00 (half of the circumference value). In the third step, the circumference layer with an elevated strain has a wedge-like shape. In the fourth step, the circumference layer (with elevated strain) has an equal thickness along the extrusion axis. This indicates the steady phase. The plastic strain at the bar front end is higher at the circumference than in the center. This confirms the structural analysis results. They show that the central part of the bar may retain its cast structure, while the circumference is deformed. If the bar central part is required to have some specific properties, the bar has to undergo another manufacturing operation to increase the accumulated strain. Re-extrusion processes the areas insufficiently deformed during the first extrusion.

Keywords: extrusion, plastic strain, metal structure, heterogenic properties, finite element modeling, simulation

Acknowledgments: This study is part of the Russian Science Foundation project (No. 22-29-00931, dated 20.12.2021).

For citation: Loginov Yu.N., Razinkin A.V., Shimov G.V., Maltseva T.V., Bushueva N.I., Dymshakova E.G., Kalinina N.A. Structure and strain state of aluminum bars at the initial phase of extrusion. *Izvestiya. Non-Ferrous Metallurgy.* 2023;29(2):29–37.
https://doi.org/10.17073/0021-3438-2023-2-29-37

Структурное состояние и деформации заготовки из алюминиевого сплава в начальной стадии прессования

Ю.Н. Логинов[1,2], **А.В. Разинкин**[3], **Г.В. Шимов**[1], **Т.В. Мальцева**[1], **Н.И. Бушуева**[1], **Е.Г. Дымшакова**[3], **Н.А. Калинина**[3]

[1] **Уральский федеральный университет имени первого Президента России Б.Н. Ельцина**
620002, Россия, г. Екатеринбург, ул. Мира, 19

[2] **Институт физики металлов имени М.Н. Михеева УрО РАН**
620108, Россия, г. Екатеринбург, ул. С. Ковалевской, 18

[3] **ОАО «Каменск-Уральский металлургический завод»**
623405, Россия, Свердловская обл., г. Каменск-Уральский, ул. Заводская, 5

✉ Георгий Викторович Шимов (G.v.shimov@urfu.ru)

Аннотация: Выявлены особенности строения зон недостаточной проработки металла в нестационарной стадии прессования. В условиях ОАО «Каменск-Уральский металлургический завод» (Россия) на прессе номинальным усилием 120 МН выполнено прессование слитка из контейнера диаметром 800 мм с получением прутка диаметром 355,6 мм. Материал слитка – алюминиевый сплав АД33 (ГОСТ 4784) – аналог сплава 6061 по стандарту ASTM системы Al–Mg–Si. Относительное обжатие в таком процессе составляло 80 %, а коэффициент вытяжки – 5,06. Дальнейшее исследование включало изучение макроструктуры, микроструктуры вдоль радиальной координаты, определение среднего размера зерна вдоль радиальной координаты, испытания механических свойств при комнатной и повышенной температурах. Установлено, что макроструктура выходной части прутка – мелкозернистая, однородная, плотная, неметаллические и интерметаллидные включения отсутствуют. Однако по поперечному сечению выявлена разноструктурность: в центре структура демонстрирует слабодеформированное состояние, сохраняя рисунок строения дендритных ячеек, унаследованных от литья; на периферии структура имеет строчечное строение, ее составляющие малого размера и равномерно распределены. Получены значения прочностных свойств при повышенных температурах и выполнено сравнение с известными из литературы данными. Материал в опытах оказался прочнее почти в 2 раза, что говорит о его неполном разупрочнении. Также выполнено сравнение пластических свойств. В расчетной части с помощью программного модуля DEFORM-2D проведено численное моделирование прессования с малым коэффициентом вытяжки. Выявлено, что металл на периферии подвергается большей степени деформации с самого начала процесса. Отслеживание ситуации по шагам показало, что на первом шаге деформации локализованы вблизи отверстия матрицы, на втором – наблюдалось образование жесткой зоны в окрестности стыка матрицы и рабочей втулки контейнера. В периферийной области установился слой металла со степенью деформации 1,75–2,00. В то же время в центре этот диапазон снизился до 0,75–1,00, т.е. значения оказались практически в 2 раза меньше. На третьем шаге периферийный слой с повышенным уровнем деформации имеет клинообразную форму, на четвертом – периферийный (с повышенной степенью деформации) слой имеет равную толщину вдоль оси прессования, что говорит о наступлении стационарной стадии. Для переднего конца прутка на периферии показатель пластической деформации выше, чем для центральной части. Это подтверждает результаты структурного анализа, где было показано, что в центральной части может сохраняться литая структура, в то время как на периферии возникают все признаки наличия деформированного состояния. Таким образом, если возникает необходимость использования этой части заготовки в качестве материала с необходимым уровнем свойств, то придется применить технологическую операцию с увеличением накопленной степени деформации. При запланированной повторной обработке прессованием создаются условия для проработки областей металла, недостаточно деформированных при первичной обработке.

Ключевые слова: прессование, пластическая деформация, структура металла, неоднородность свойств, метод конечных элементов, численное моделирование

Благодарности: Исследования проведены в рамках выполнения проекта Российского научного фонда (№ 22-29-00931 от 20.12.2021).

Для цитирования: Логинов Ю.Н., Разинкин А.В., Шимов Г.В., Мальцева Т.В., Бушуева Н.И., Дымшакова Е.Г., Калинина Н.А. Структурное состояние и деформации заготовки из алюминиевого сплава в начальной стадии прессования. *Известия вузов. Цветная металлургия*. 2023;29(2):29–37. https://doi.org/10.17073/0021-3438-2023-2-29-37

Introduction and problem statement

Extrusion is a common manufacturing process used for making aluminum or other light metal parts [1]. The process should be quickly adjusted to make new parts since the product range can be extremely extensive. This means replacing just one tooling for extrusion — the die. Moreover, extrusion improves metal ductility by irregularly compressing the metal from all sides. Indeed, the ductility of aluminum alloys is often low [2]. The extrusion process is required in order to increase ductility [3, 4].

On the other hand, extrusion results in a irregularly strain distribution [5], especially in the initial phase. This phase is commonly referred to as unsteady. It begins with closing the opening between the bar and tooling, and the metal expanding and filling the extrusion container [6, 7]. Next, the bar front endis pushed through the opening in the die. At this phase, the strain gradually penetrates the metal. However, the compressive stress is not yet high enough which may lead to cracking [8].

Finally, the process reaches the steady phase. This is when the strain field is stabilized. There is a chance to obtain consistent metal properties and structure the entire bar length [9], although some inconsistencies across the cross-section will most likely remain [10—12]. In this case, the bar outer shell experiences extensive strain, which may lead to cracking [13].

A question arises: how long is the unsteady phase? We need to know this, in order to determine which bar part meets the specifications.

Few studies address this question. It should be noted some papers about this topic [14, 15]. Finite element modeling can be used to simulate the stresses and strains in real extrusion processes [16, 17].

The study purpose is to identify the structure of insufficiently deformed areas at the unsteady extrusion phase.

Industrial test conditions

The tests was performed at Kamensk Uralsky Metallurgical Works using a 120 MN press and 800 mm dia. press container, in order to extrude a 355.6 mm dia. bar. The bar material is the Al—Mg—Si AD33 aluminum alloy (GOST 4784), similar to ASTM 6061. Its required chemical composition is (wt.%): 0.8—1.20 Mg; 0.4—0.8 Si; 0.04—0.35 Cr; 0.15—0.40 Cu. The actual metal composition was as follows (wt.%): 1.0 Mg; 0.6 Si; 0.14 Cr; 0.19 Cu; 0.58 Fe; 0.10 Mn; 0.02 Zn; 0.06 Ti. Some of the elements are acceptable impurities.

The percent reduction was 80 %, and the reduction ratio was 5.06. After the test, we studied:

— macrostructure;
— microstructure along the radius;
— average grain size along the radius;
— mechanical properties at room and elevated temperatures.

For the tests, the samples was cut off from the front end of the bar. Fig. 1 shows the metal macrostructure (1/4 cross-section). The bar front end macrostructure is fine-grained, homogeneous, and dense, with no non-metallic or inter-metallic inclusions.

The bar front end macrostructure is dense, with no non-metallic or inter-metallic inclusions in the cross-section. We identified several structures in the cross-section:

— the center (Fig. 2, *a*) is weakly deformed, preserving the dendritic cell structure inherited from the casting;

— the same structure is at half of the radius (Fig. 2, *b*) from the center;

— at the circumference (Fig. 2, *c*), a streaked structure is formed. Its components are crushed and uniformly distributed.

The streak structure indicates that the main elongation occurs along the extrusion axis. In the cylindrical coordinate system, the other principal strains (tangent and radial) are compression strains.

The average grain size at the bar center at half of the radius from the center was 190 μm, and 30 μm at the

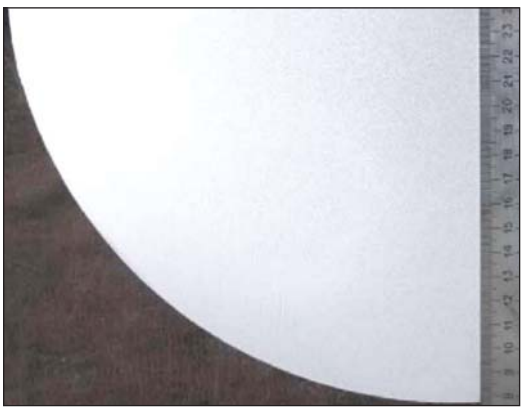

Fig. 1. The bar front end macrostructure, 355.6 mm dia. (1/4 cross-section)

Рис. 1. Макроструктура выходной части прутка диаметром 355,6 мм (поперечное сечение, четверть темплета)

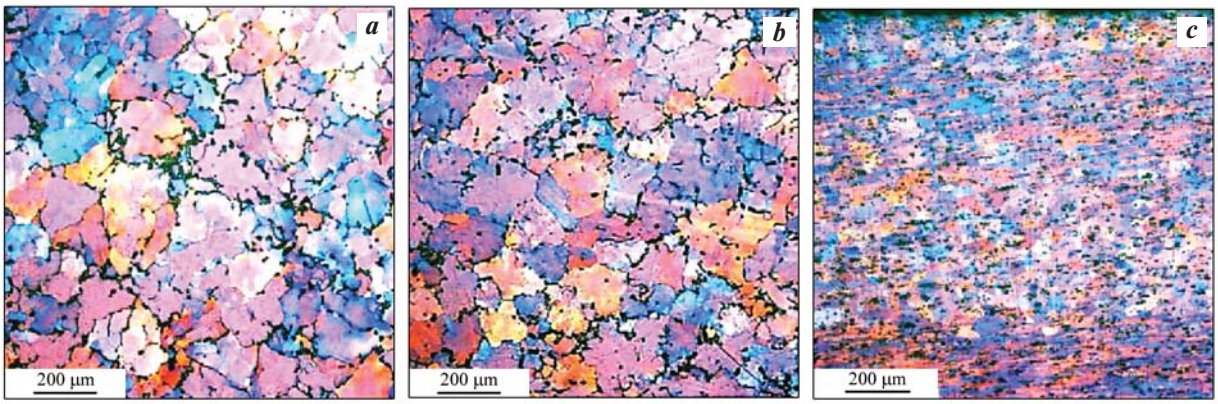

Fig. 2. The bar microstructure in polarized light. Bar center (***a***), at half of the radius from the center (***b***), and the circumference (***c***)

Рис. 2. Микроструктура в поляризованном свете прутка в центре (***a***), на половине радиуса (***b***) и на периферии (***c***)

circumference (6× difference). It indicates inconsistent penetration of the strains along the radius. The smaller the grain size, the larger the strain.

Fig. 3 shows the strength vs. temperature curve. There is a large (up to 94 %) difference between the ultimate tensile strength and offset yield strength at room temperature. However, it drops sharply at t = = 300 °C. The strength decreases as the temperature increases.

The comparison was made for the measured strength values at elevated temperatures to those reported by other researchers. Chinese researchers [18] performed static tests (0.001 s^{-1} strain rate) with the 6061 alloy at t = 450 °C. The yield stress was 18 MPa. This value is similar to the yield offset measured with the procedure proposed by A.V. Tretiakov and V.I. Zyuzin [19]. The tested material strength almost doubled, thus indicating its incomplete softening. The authors of the paper [18] suggested that the softening in the temperature range which they studied is caused not by recrystallization, but by dynamic recovery.

Fig. 4 shows the ductility properties of the alloy. This relationship is non-monotonic in contrast to strength. The test values was compared to the available results for the AD33 alloy. For example, according to matweb.com, alloy 6061 (AD33 analog made to the ASTM standard) after annealing has 124 MPa tensile strength and

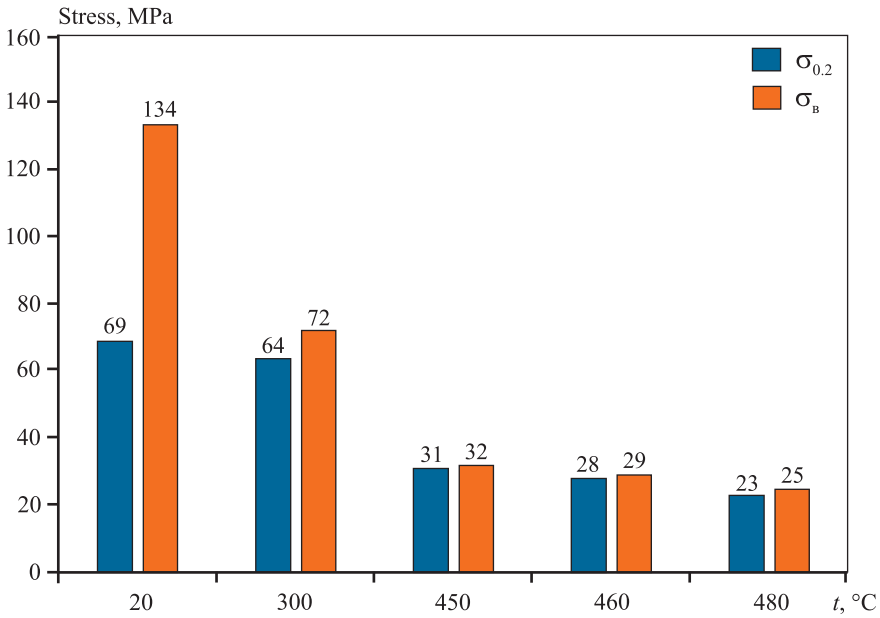

Fig. 3. Strength vs. test temperature curve

Рис. 3. Зависимость прочностных свойств от температуры испытаний

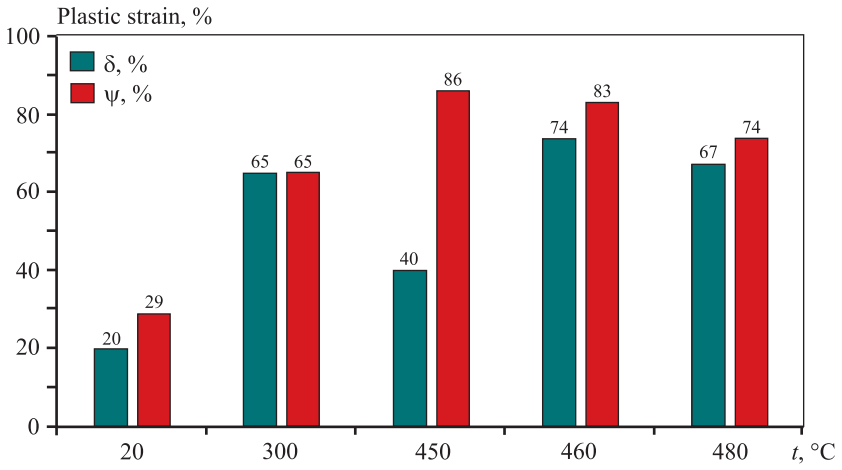

Fig. 4. The bar front end ductility vs. test temperature

Рис. 4. Показатели пластичности передней части прутка в зависимости от температуры испытаний

55 MPa yield strength. The experimental values were 134 and 69 MPa (8 % and 25 % higher), respectively, i.e. the strength exceeded the standard values for the annealed alloy.

The matweb.com database indicates the relative elongation at break for the alloy is 30 %. The relative elongation at break that we measured is 19 %, which is less than the rated value by $100 \cdot (30 - 19)/30 \approx 37$ %. This means that the bar front end after extrusion is partially hardened. The hardening is more intense at the circumference. It is confirmed by greater grain refinement among other things.

The relative reduction of area can be used to estimate the shear strain at break and to plot the fracture diagram [20].

Fig. 4 shows that the relative reduction of area increases sharply as the metal is heated: at $t = 300$ °C it is 65 % and remains high (74—86 %) at 450—480 °C. This enables the subsequent metal forming without cracking. It is assumed that the extruded bar front end will be re-extruded at the next process stage. The high strain during extrusion will further enhance the metal structure to its final form.

Simulation

The above conclusion can be confirmed by simulation of the metal behavior during extrusion with a small area reduction. DEFORM-2D software was used. The stress-strain simulation model was axisymmetric. The thermal boundary conditions were as close as possible to the actual values:

— bar temperature: 470 °C;

— press container temperature: 450 °C;

— die and pressure pad temperature: 380 °C;

— ambient temperature at the die hole: 20 °C;

— convective heat transfer coefficient: 0.02 N/s/mm/°C;

— overall heat transfer coefficient: 11 N/c/mm/°C.

The coefficient values and UoMs are as indicated in the software UI.

The extrusion ram velocity was 3.7 mm/s. The boundary conditions are expressed as Siebel law for the 0.7 friction coefficient. The reason for this is the high normal stress typical of extrusion. The container and die diameters were 800 mm and 355.6 mm, respectively, identical to the industrial test (see above). The more detailed problem statement is presented in [21].

Fig. 5 shows the simulation results as equal strain regions. Indeed, the metal at the circumference is exposed to a greater strain degree from the beginning of extrusion. This is because the bar front end is extruded first as an undeformed, rigid plug with a diameter equal to the die diameter. Then the strain rate increases inwards. This process is gradual and slow.

Fig. 5, *a*—*d* shows the steps of this sequence and the color strain scale (Fig. 5, *e*)

In the first step (Fig. 5, *a*), the strain is localized near the die. In the second step (Fig. 5, *d*), a “dead” (rigid) area is formed in the vicinity of the die/container liner interface. The circumference metal layer with a 1.75—2.00 reduction of area is formed. Concurrently, this range is 0.75—1.00 (half of the circumference value) at the bar center.

In the third step (Fig. 5, *c*), the circumference layer with an elevated strain has a wedge-like shape. Its thickness is increased, i.e., the process is not yet at the steady phase. The extruded length-to-bar diameter ratio is 2. In

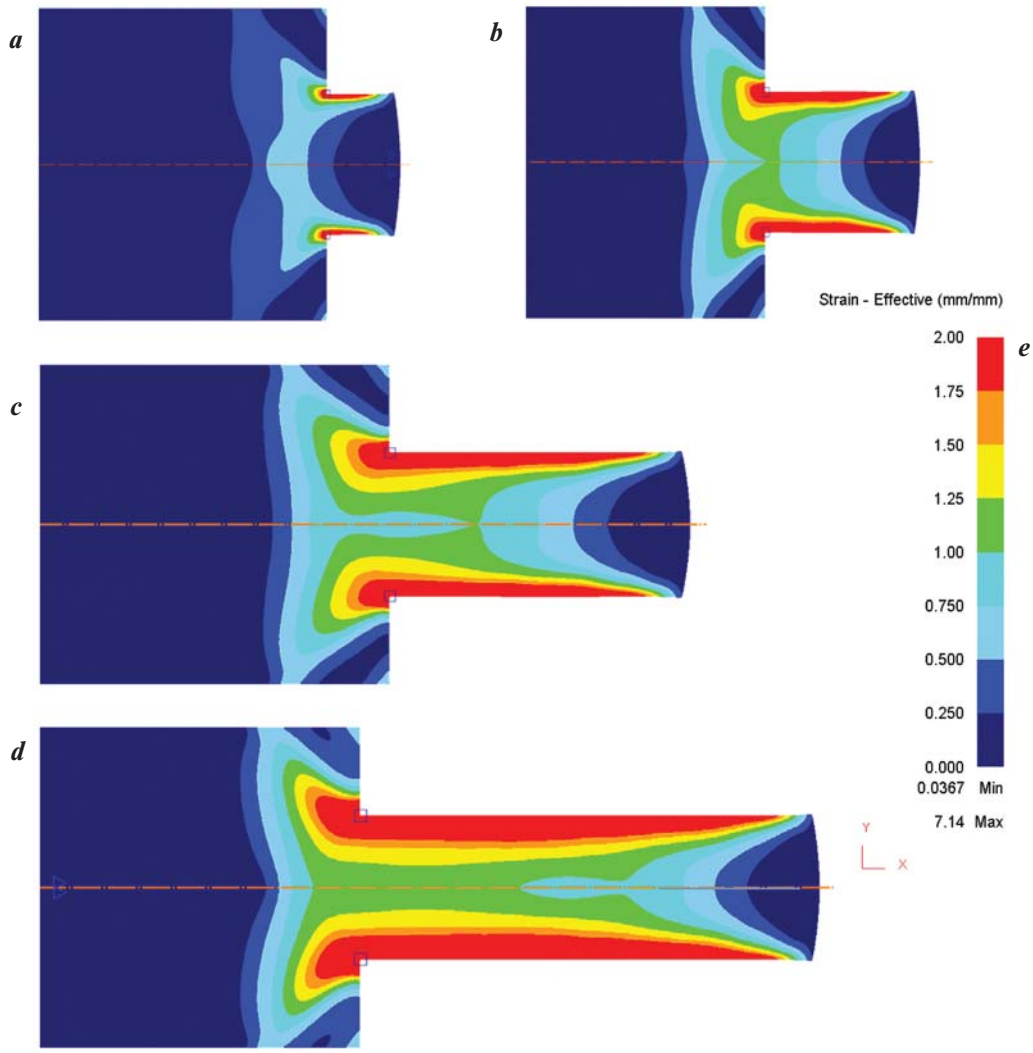

Fig. 5. Strain distribution vs. the bar front end relative extruded length (length to diameter ratio)
a – 0.5, ***b*** – 1.0, ***c*** – 2.0, ***d*** – 3.0, ***e*** – effective strain color scale

Рис. 5. Изменение картины распределения степени деформации по мере выдавливания переднего конца прутка на относительную длину (отношение его длины к диаметру)
a – 0,5, ***b*** – 1,0, ***c*** – 2,0, ***d*** – 3,0, ***e*** – цветовая шкала степени деформации strain effective

the fourth step, the circumference layer (with elevated strain) has an equal thickness along the extrusion axis. It indicates the steady phase. The strain in the center is now in the 1.00—1.25 range.

The estimated strain as the logarithm of the reduction ratio (the logarithm of the bar area before/after extrusion ratio) is 0.7. The FEM analysis gives slightly excessive strain values, since the shear strain is also included, but the reduction ratio is ignored.

In general, the color-coded strain patterns show that at the steady phase. The plastic strain at the bar front end is higher at the circumference than in the center [22]. It confirms the above structural analysis results. They show that the bar central part may retain its cast structure, while the circumference is deformed.

If the bar central part is required to have some specific properties, the bar has to undergo another manufacturing operation to increase the accumulated strain.

Conclusion

The structural analysis of the hot-pressed 6061 aluminum alloy bar front end showed that the front end has an inconsistent grain size distribution. The central part contains large grains. The grain size decreases towards the circumference.

The hot sample tests revealed a sufficiently high duc-

tility of the extruded bar front end. The bar is suitable for re-extrusion to process the areas insufficiently deformed during the first extrusion.

References

1. Bauser M., Sauer G., Siegert K. Extrusion. 2nd Ed. Ohio: ASM International, 2006.
2. Sukunthakan Ngernbamrung, Yudai Suzuki, Norio Takatsuji, Kuniaki Dohda. Investigation of surface cracking of hot-extruded AA7075 billet. *Procedia Manufacturing*. 2018;15:217—224. https://doi.org/10.1016/j.promfg.2018.07.212
3. Loginov Yu.N. Extrusion as a method of intensive deformation of metals and alloys. Yekaterinburg: UrFU, 2016. 156 p. (In Russ).
   Логинов Ю.Н. Прессование как метод интенсивной деформации металлов и сплавов. Екатеринбург: УрФУ, 2016. 156 с.
4. Mayén J., Abúndez A., Pereyra I., Colín J., Blanco A., Serna S. Comparative analysis of the fatigue short crack growth on Al 6061-T6 alloy by the exponential crack growth equation and a proposed empirical model. *Engineering Fracture Mechanics*. 2017;177:203-217. https://doi.org/10.1016/j.engfracmech.2017.03.036
5. Shinobu Kaneko, Kenji Murakami, Tetsuo Sakai. Effect of the extrusion conditions on microstructure evolution of the extruded Al—Mg—Si—Cu alloy rods. *Materials Science and Engineering: A*. 2009; 500:8—15. https://doi.org/10.1016/j.msea.2008.09.057
6. Teleshov V.V., Snegireva L.A., Zakharov V.V. On the influence of some technological factors on the structure and properties of large-sized pressed semi-finished products. *Tekhnologiya legkikh splavov*. 2022;1:10—21. (In Russ).
   Телешов В.В., Снегирева Л.А., Захаров В.В. О влиянии некоторых технологических факторов на структуру и свойства крупногабаритных прессованных полуфабрикатов. *Технология легких сплавов*. 2022;1:10—21. (In Russ).
7. Loginov Yu.N., Degtyareva O.F. Influence of the stage of pressing out of a hollow aluminum alloy ingot on the process of subsequent pressing. Kuznechno-shtampovochnoye proizvodstvo. *Obrabotka materialov davleniyem*. 2007;7:37—42. (In Russ).
   Логинов Ю.Н., Дегтярева О.Ф. Влияние стадии распрессовки полого слитка из алюминиевого сплава на процесс последующего прессования. *Кузнечно-штамповочное производство. Обработка материалов давлением*. 2007;7:37—42.
8. Loginov Yu.N., Antonenko L.V. Study of the stress-strain state to prevent the formation of longitudinal cracks in pressed pipes. *Tsvetnyye metally*. 2010;5:119—122. (In Russ).
   Логинов Ю.Н., Антоненко Л.В. Изучение напряженно-деформированного состояния для предупреждения образования продольных трещин в прессованных трубах. *Цветные металлы*. 2010;5:119—122.
9. Danilin A.V., Danilin V.N., Romantsev B.A. Predicting the type of structure after pressing in products made of hard-to-form aluminum alloys based on the results of mathematical modeling. *Kuznechno-shtampovochnoye proizvodstvo. Obrabotka materialov davleniyem*. 2019;1:26—38. (In Russ).
   Данилин А.В., Данилин В.Н., Романцев Б.А. Прогнозирование вида структуры после прессования в изделиях из труднодеформируемых алюминиевых сплавов на основании результатов математического моделирования. *Кузнечно-штамповочное производство. Обработка материалов давлением*. 2019;1:26—38.
10. Nadja Berndt, Philipp Frint, Marcus Böhme, Sören Müller, Martin F.-X. Wagner. On radial microstructural variations, local texture and mechanical gradients after cold extrusion of commercially pure aluminum. *Materials Science and Engineering: A*. 2022;850:143496. https://doi.org/10.1016/j.msea.2022.143496
11. Lin G., Song W., Feng D., Li K., Feng Y., Liu J. Study of microstructure and mechanical property heterogeneity throughout the wall thickness of high strength aluminum alloy thick-wall pipe. *Journal of Materials Research*. 2019:34(15);2736—2745. https://doi.org/10.1557/jmr.2019.127
12. Kai Zhang, Knut Marthinsen, Bjørn Holmedal, Trond Aukrust, Antonio Segatori. Through thickness variations of deformation texture in round profile extrusions of 6063-type aluminium alloy: Experiments, FEM and crystal plasticity modelling. *Materials Science and Engineering: A*. 2018;722:20—29. https://doi.org/10.1016/j.msea.2018.02.081
13. Ridha Hambli, Daniel Badie-Levet. Damage and fracture simulation during the extrusion processes. *Computer Methods in Applied Mechanics and Engineering*. 2000;186(1):109—120. https://doi.org/10.1016/S0045-7825(99)00109-7
14. Berezhnoy V.L. Analysis and formalization of ideas about the unevenness of deformation for the technological development of pressing. *Tekhnologiya legkikh splavov*. 2013;1:40—57. (In Russ).
   Бережной В.Л. Анализ и формализация представлений о неравномерности деформации для технологического развития прессования. *Технология легких сплавов*. 2013;1:40—57.

15. Li J., Wu X., Liao B., Cao L. Simulation of dynamic recrystallization in an Al—Mg—Si alloy during inhomogeneous hot deformation. *Materials Today Communications*. 2021;29:102810. https://doi.org/10.1016/j.mtcomm.2021.102810
16. Zhi Peng and Terry Sheppard. A study on material flow in isothermal extrusion by FEM simulation. *Modelling and Simulation in Materials Science and Engineering*. 2004;12(5):745—763. https://doi.org/10.1088/0965-0393/12/5/001
17. Kai Zhang, Knut Marthinsen, Bjørn Holmedal, Trond Aukrust, Antonio Segatori. Through thickness variations of deformation texture in round profile extrusions of 6063-type aluminium alloy: Experiments, FEM and crystal plasticity modelling. *Materials Science and Engineering: A*. 2018;722:20—29. https://doi.org/10.1016/j.msea.2018.02.081
18. Wei Chen, Ying-ping Guan, Zhen-hua Wang. Hot deformation behavior of high Ti 6061 Al alloy. *Transactions of Nonferrous Metals Society of China*. 2016;26(2):369—377. https://doi.org/10.1016/S1003-6326(16)64129-8
19. Tretyakov A.V., Zyuzin V.I. Mechanical properties of metals and alloys during pressure treatment. Moscow: Metallurgiya, 1973. 224 p. (In Russ).
Третьяков А.В., Зюзин В.И. Механические свойства металлов и сплавов при обработке давлением. М.: Металлургия, 1973. 224 с.
20. Kolmogorov V.L. Mechanics of metal pressure treatment: Moscow: Metallurgiya, 1986. 687 p. (In Russ).
Колмогоров В.Л. Механика обработки металлов давлением: М.: Металлургия, 1986. 687 с.
21. Loginov Yu.N., Shimov G.V., Bushueva N.I. Deformations in the nonstationary stage of aluminum alloy rod extrusion process with a low elongation ratio. *Obrabotka metallov (tekhnologiya, oborudovanie, instrumenty) = Metal Working and Material Science*. 2022;24(2):39—49. https://doi.org/10.17212/1994-6309-2022-24.2-39-49
22. Hongmei Che, Xianquan Jiang, Nan Qiao, Xiaokui Liu. Effects of Er/Sr/Cu additions on the microstructure and mechanical properties of Al—Mg alloy during hot extrusion. *Journal of Alloys and Compounds*. 2017;708:662—670. https://doi.org/10.1016/j.jallcom.2017.01.039

Information about the authors

Yuri N. Loginov – Dr. Sci. (Eng.), Professor of the Department "Metal Processing by Pressure", Ural Federal University named after the First President of Russia B.N. Yeltsin (UrFU); Leading Research Scientist, Institute of Metal Physics named after M.N. Mikheev of the Ural Branch of the Russian Academy of Sciences.
https://orcid.org/0000-0002-7222-2521
E-mail: J.n.loginov@urfu.ru

Alexander V. Razinkin – Cand. Sci. (Eng.), Director of Technology, Kamensk Uralsky Metallurgical Works JSC (JSC "KUMZ").
E-mail: RazinkinAV@kumz.ru

Georgy V. Shimov – Cand. Sci. (Eng.), Ass. Professor of the Department "Metal Processing by Pressure", UrFU.
https://orcid.org/0000-0001-5763-0837
E-mail: G.v.shimov@urfu.ru

Tatiana V. Maltseva – Cand. Sci. (Eng.), Ass. Professor of the Department of Materials Science, UrFU.
E-mail: For_mtv01@mail.ru

Natalia I. Bushueva – Research Engineer of the Scientific Laboratory "Metal Processing by pressure", UrFU.
https://orcid.org/0000-0002-0603-8785
E-mail: N.i.bushueva@urfu.ru

Elena G. Dymshakova – Head of the Central Factory Laboratory, JSC "KUMZ".
E-mail: Dymshakovaeg@kumz.ru

Natalia A. Kalinina – Process Engineer, JSC "KUMZ".
E-mail: Kalinina_NA@mail.ru

Информация об авторах

Юрий Николаевич Логинов – д.т.н., профессор кафедры «Обработка металлов давлением», Уральский федеральный университет имени первого Президента России Б.Н. Ельцина (УрФУ); вед. науч. сотрудник Института физики металлов им. М.Н. Михеева УрО РАН.
https://orcid.org/0000-0002-7222-2521
E-mail: J.n.loginov@urfu.ru

Александр Викторович Разинкин – к.т.н., директор по технологии, ОАО «Каменск-Уральский металлургический завод» (ОАО «КУМЗ»).
E-mail: RazinkinAV@kumz.ru

Георгий Викторович Шимов – к.т.н., доцент кафедры «Обработка металлов давлением», УрФУ.
https://orcid.org/0000-0001-5763-0837
E-mail: G.v.shimov@urfu.ru

Татьяна Викторовна Мальцева – к.т.н., доцент кафедры материаловедения, УрФУ.
E-mail: For_mtv01@mail.ru

Наталья Игоревна Бушуева – инженер-исследователь научной лаборатории «Обработка металлов давлением», УрФУ.
https://orcid.org/0000-0002-0603-8785
E-mail: N.i.bushueva@urfu.ru

Елена Геннадьевна Дымшакова – начальник центральной заводской лаборатории ОАО «КУМЗ».
E-mail: Dymshakovaeg@kumz.ru

Наталья Александровна Калинина – инженер-технолог ОАО «КУМЗ».
E-mail: Kalinina_NA@mail.ru

Contribution of the authors

Yu.N. Loginov – formation of the main concept, setting the goal and objectives of the study, preparation of the text, formulation of conclusions.

A.V. Razinkin – organizing the collection of production parameters and their analysis, adjusting the links between production observations and calculated data.

G.V. Shimov – statement of the problem of a computational experiment and analysis of the solution of this problem.

T.V. Maltseva – establishing links between metallographic studies and mechanical properties.

N.I. Bushueva – carrying out calculations by the finite element method, building relationships between the calculated parameters.

E.G. Dymshakova – setting the tasks of metallographic analysis, its implementation and processing of results.

N.A. Kalinina – processing of observations in the production process, streamlining these data.

Вклад авторов

Ю.Н. Логинов – формирование основной концепции, постановка цели и задачи исследования, подготовка текста, формулировка выводов.

А.В. Разинкин – организация сбора производственных параметров и их анализ, корректировка связей между производственными наблюдениями и расчетными данными.

Г.В. Шимов – постановка задачи вычислительного эксперимента, анализ решения этой задачи.

Т.В. Мальцева – установление связей между металлографическими исследованиями и механическими свойствами.

Н.И. Бушуева – проведение расчетов методом конечных элементов, построение связей между расчетными параметрами.

Е.Г. Дымшакова – постановка задач металлографического анализа, его проведение и обработка результатов.

Н.А. Калинина – обработка наблюдений в производственном процессе, упорядочение полученных данных.

The article was submitted 21.02.2023, revised 14.03.2023, accepted for publication 16.03.2023

Статья поступила в редакцию 21.02.2023, доработана 14.03.2023, подписана в печать 16.03.2023

UDC 620.178.322.3
https://doi.org/10.17073/0021-3438-2023-2-38-48

Research article
Научная статья

Structure and tensile fracture mechanism of aluminum matrix composites produced by internal oxidation

V.V. Mylnikov[1], **E.A. Chernyshov**[1], **A.D. Romanov**[2], **M.V. Mylnikova**[1], **E.A. Zakharychev**[1,3], **N.A. Ryabov**[1]

[1] **Nizhny Novgorod State University of Architecture and Civil Engineering**
65 Ilyinskaya Str., Nizhny Novgorod 603950, Russia

[2] **Nizhny Novgorod State Technical University n.a. R.E. Alekseev**
24 Minina Str., Nizhny Novgorod 603950, Russia

[3] **Institute of Chemistry of N.I. Lobachevsky National Research University**
23 Gagarin Prosp., Nizhny Novgorod, GSP-20 603950, Russia

✉ Vladimir V. Mylnikov (mrmylnikov@mail.ru)

Abstract: This article presents experimental results of resistance against fracture upon static tension of cast aluminum matrix composites based on aluminum with various content of Al_2O_3 strengthening phase. The cast aluminum matrix composite materials were produced by the technology based on burnout of aluminum melt upon interaction with oxygen. Two batches of ingots with various content of solid phase were smelted for tests of static strength. The average particle size of strengthening phase of predominantly prismatic morphology was 60–80 μm, and their content varied from 15 to 25 %. The fracture surfaces obtained upon static uniaxial tension of the considered samples were studied on the samples destroyed at maximum stress. The fracture surfaces were analyzed using an optical microscope with expanded options due to improved long-focus system and digital processing of images based on unique procedure of 3D structure analysis. For in-depth analysis of characteristic fracture region a scanning electron microscope was used equipped with energy and wavelength dispersive elemental analyzers. It was established in the studies that in the samples with lower content of dispersed phase, the fracture is characterized by mixed heterogeneous in terms of macrogeometry pattern. This can be interpreted as dry fibrous fracture with visible crystalline pimples and breakaways. With an increase in the solid phase, a mixed, sufficiently homogenous in terms of macrogeometry, fracture pattern of fanlike fibrous structure can be observed. Crystalline pimples were also detected of a different fracture surface area, as well as breakaways of other geometrical sizes. The features of changes in the relief of fracture surface and the fracture mechanisms of the obtained composites have been detected and described.

Keywords: cast aluminum matrix dispersion strengthened composite material (DSCM), corundum, tension, transcrystalline fracture, intercrystallite fracture, macrostructure, microstructure, deformation

Acknowledgments: This work was supported by the Russian Science Foundation, grant No. № 22-13-20009, https://rscf.ru/project/22-13-20009/

For citation: Mylnikov V.V., Chernyshov E.A., Romanov A.D., Mylnikova M.V., Zakharychev E.A., Ryabov N.A. Structure and tensile fracture mechanism of aluminum matrix composites produced by internal oxidation. *Izvestiya. Non-Ferrous Metallurgy.* 2023;29(2):38–48. https://doi.org/10.17073/0021-3438-2023-2-38-48

Структура и механизм разрушения алюмоматричных композитов, полученных методом внутреннего окисления, при растяжении

В.В. Мыльников[1], Е.А. Чернышов[1], А.Д. Романов[2], М.В. Мыльникова[1], Е.А. Захарычев[1,3], Н.А. Рябов[1]

[1] **Нижегородский государственный архитектурно-строительный университет**
603950, Россия, г. Нижний Новгород, ул. Ильинская, 65

[2] **Нижегородский государственный технический университет им. Р.Е. Алексеева**
603950, Россия, г. Нижний Новгород, ул. Минина, 24

[3] **Нижегородский государственный университет им. Н.И. Лобачевского**
603950, Россия, г. Нижний Новгород, ГСП-20, пр-т Гагарина, 23

✉ Владимир Викторович Мыльников (mrmylnikov@mail.ru)

Аннотация: Представлены результаты исследований сопротивления разрушению при статическом растяжении литых алюмоматричных композитов на основе алюминия с различным содержанием упрочняющей фазы Al_2O_3. Литые алюмоматричные композиционные материалы были изготовлены по технологии, которая основана на процессе выгорания расплава алюминия при взаимодействии с кислородом. Для проведения исследований на статическую прочность были отлиты две партии слитков с различным содержанием твердой фазы. Средний размер частиц упрочняющей фазы, преимущественно призматической морфологии, составлял 60–80 мкм, а их количество изменяли от 15 до 25 %. Поверхности разрушения, полученные при статическом одноосном растяжении исследованных образцов материала, изучались на образцах, разрушившихся при максимальном значении напряжения. Исследования поверхности разрушения проводились с помощью оптического микроскопа с расширенными возможностями за счет усовершенствованной длиннофокусной оптической системы и цифровой обработки изображения с применением оригинальной методики изучения 3D-структур. Для углубленного анализа характерных областей излома использовался растровый электронный микроскоп с энерго- и волнодисперсионным элементным анализаторами. В ходе проведенных исследований было установлено, что у образцов с меньшим содержанием дисперсной фазы излом носит смешанный неоднородный по макрогеометрии характер, который можно интерпретировать как сухой волокнистый излом с видимыми кристаллической сыпью и вырывами. С увеличением количества твердой фазы наблюдается смешанный, достаточно однородный по макрогеометрии характер излома с веерообразно-волокнистым строением, в котором также зафиксированы кристаллическая сыпь, отличающаяся распределением по площади излома, и вырывы других геометрических размеров. Выявлены и описаны особенности изменения рельефа поверхности разрушения и механизмы разрушения полученных композитов.

Ключевые слова: литой алюмоматричный дисперсно-упроченный композиционный материал (ДУКМ), корунд, растяжение, транскристаллитное разрушение, интеркристаллитное разрушение, макроструктура, микроструктура, деформация

Благодарности: Исследование выполнено за счет гранта Российского научного фонда № 22-13-20009.
https://rscf.ru/project/22-13-20009/

Для цитирования: Мыльников В.В., Чернышов Е.А., Романов А.Д., Мыльникова М.В., Захарычев Е.А., Рябов Н.А. Структура и механизм разрушения алюмоматричных композитов, полученных методом внутреннего окисления, при растяжении. *Известия вузов. Цветная металлургия*. 2023;29(2):38–48. https://doi.org/10.17073/0021-3438-2023-2-38-48

Introduction

Cast composite materials are promising in terms of their wide scale implementation in various fields of aircraft and mechanical engineering as anti-friction structural and other materials. They provide for decrease in the item weight, improvement of their specifications and especially development of new machines and structures [1—8]. Serial production of dispersion strengthened composite materials (DSCM) with solid phase in the form of SiC and Al2O3 was pioneered by “Duralcan” (Canada), “Alcan” and “Alcoa” (Canada, USA). However, full scale use of DSCM is restricted, especially in Russia, and does not comply with potential technical

capabilities of these materials. This is primarily attributed to insufficiently developed scientific and engineering basis for their creation, which would guarantee the selection and forecasting of their structure, composition and production technology. This would also achieve the required strength and operational properties of machine parts and structures from DSCM, including those with nanosized strengthening elements at acceptable costs [9—11].

Leading positions in terms of application volumes in various fields of mechanical engineering and aircraft are occupied by composite materials based on aluminum matrix. At present numerous technologies of strengthening by dispersed phase are available, including strengthening by own oxides (Al_2O_3) and carbides (Al_4C_3) or mixing of various strengthening dispersed phases (for instance, TiC—Al_2O_3—Al) or aluminides (for instance, Fe_3Al—TiC) [12—21]. In each case with an increase in the volumetric fraction of solid phases, the strength increases and the plasticity of ready composites decreases.

This work investigates aluminum matrix composites obtained by liquid phase method [22], which is based on burnout of aluminum melt upon interaction with oxygen. In the course of its development the positive features of well-known technologies were taken into account: basic oxygen-converter process, casting of aluminum alloys in oxygen environment and development of air independent energy facility on the basis of high metallized fuel [23, 24]. During the interaction of aluminum melt with oxygen, the presence of solid interface between matrix and filler is provided. In addition, this method allows composites to be fabricated in one stage and to provide uniform particle distribution in the melt. Thus, it allows to more complete implementation of DSCM potential. Our comparative uniaxial tension tests demonstrated that the ultimate strength is in the range σ_u = 180÷205 MPa, which in comparison with the results in [25] (σ_u = 100÷÷150 MPa upon variation of Al_2O_3 in alloy from 5 to 20 %) is higher by about 25 %.

The aim of this work is to study the fracture surface of cast aluminum matrix composites after uniaxial tension to fracture with accounting for structure modification.

Experimental

In order to implement the developed method of internal oxidation, a unique test rig was created consisting of a high temperature induction furnace (Fig. 1, position *I*) and system of oxygen storage and supply.

The test rig is comprised of a high accuracy gas panel, equipped at the output with needle valve for accurate adjustment of gas supply, connected with a pressure meter, and after the needle transforming into a regular ball valve and rotameter. Aluminum billets were loaded into the furnace *4* (Fig. 1, position *I*) and smelted. Then, the silicon carbide tube *3* was inserted into the aluminum melt with control of the vertical supply (*1*) and in the corner (*2*), which was hermetically connected with the steel tube fixed with the rotameter. Using this system, oxygen was fed into the aluminum melt. In order to prevent undesirable surface oxidation of aluminum, the protective inert gas environment was formed which was fed via the tube *5*. As a consequence of high temperature chemical reaction $4Al + 3O_2 \rightarrow 2Al_2O_3$, the ceramic phase was obtained directly in the melt in one stage process. In order to eliminate cast defects and to degas, the synthesized material was blown with argon directly before casting into molds of moderate size.

From the fabricated castings, the samples for tensile tests (Fig. 2) were fabricated according to State Standard GOST 1497-84. The ingots were mechanically cut in the transverse direction into preliminary workpieces (Fig. 2, *a*). Then the samples were cut out (Fig. 2, *b*) and ground (Fig. 2, *c*) using the rotary horizontally located wheel of a SShPM-1 machine (Russia) with the ability to vary the number of rotations. In this case, for ease of work, the sample was installed in a special device.

After grinding, the samples were mechanically polished. In this case the wheel was covered with cloth or felt, wetted with chromium oxide slurry during polishing. The surface of polished samples was washed, degreased, and dried.

Aluminum, Grade A6 (Fig. 3, *a*), was used as a matrix material for fabrication of dispersion strengthened composite, with the following chemical composition according to State Standard GOST 11069-2001, wt.%: 99.6 Al; 0.25 Fe; 0.2 Si; 0.03 Ti; 0.01 Cu; 0.06 Zn. The alloy was strengthened with solid oxide phase Al_2O_3 (Fig. 3, *b*), in most cases with a 4- and 6-face shape. In order to analyze the static strength, two batches of ingots were smelted with various content of solid phase.

Three samples for various ingot regions were fabricated from the obtained castings. The average particle size of strengthening phase, mainly of prismatic morphology, was 60—80 μm (Fig. 4), and their content was varied from 15 to 25 vol.%.

The uniaxial tensile tests of flat samples were carried out using an AG-Xplus-0.5 universal testing machine ("Shimadzu", Japan) at ambient temperature, the loading rate was 5 N/(mm^2·s).

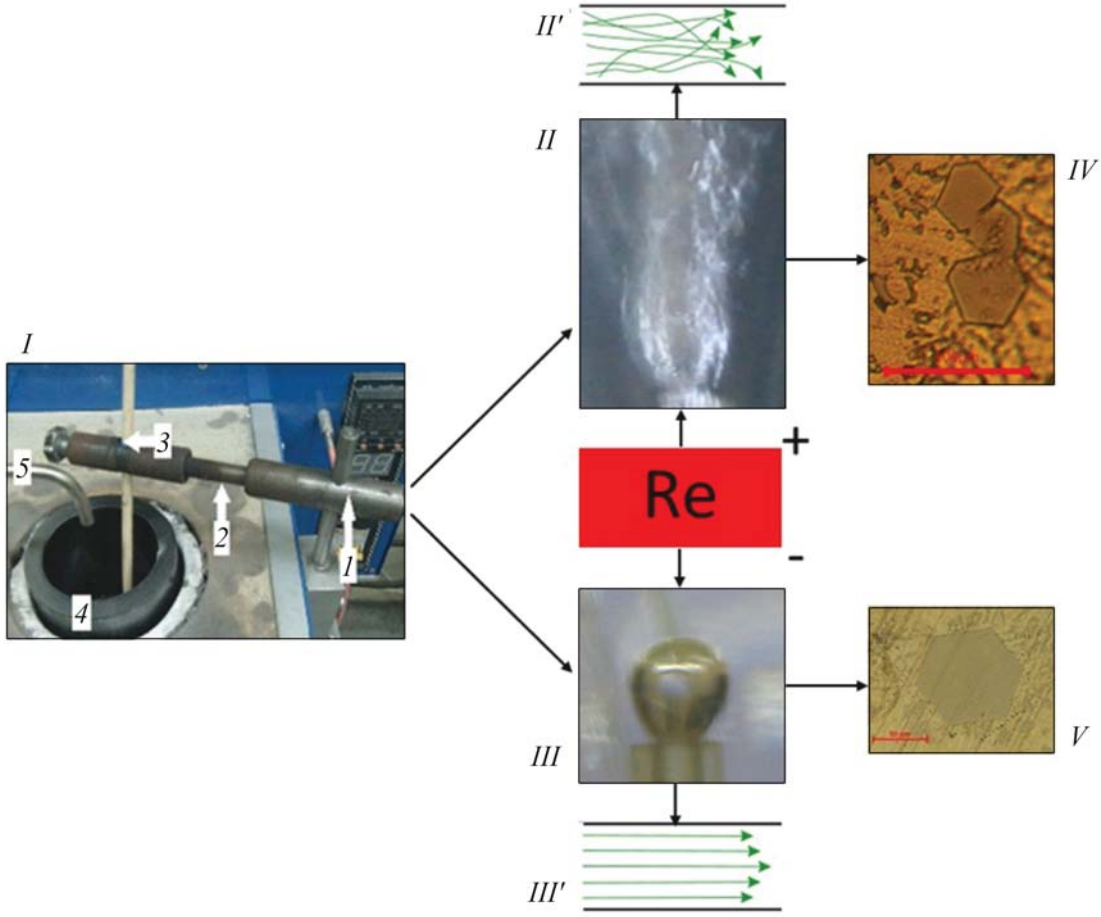

Fig. 1. Layout of ceramic phase fabrication

I – furnace working part with dismounted heat insulation (***1***, ***2*** – control system of oxidizer vertical supply (***1***) and in the corner (***2***), ***3*** – silicon carbide tube, ***4*** – crucible, ***5*** – supply tube of protective inert gas); ***II*** – jet of supplied oxidizing gas with characteristic turbulent motion regime ***II′***; ***III*** – single bubble of oxidizing gas with laminar motion regime ***III′***; ***IV*** and ***V*** – microstructures obtained in the course of processes ***II*** and ***III***

Рис. 1. Схема получения керамической фазы

I – рабочая часть печи с демонтированной теплоизоляцией (***1***, ***2*** – система регулировки подачи окислителя по вертикали (***1***) и углу (***2***), ***3*** – карбидокремниевая трубка, ***4*** – тигель, ***5*** – трубка подачи защитного инертного газа); ***II*** – струя подаваемого газа-окислителя с характерным турбулентным режимом движения ***II′***; ***III*** – единичный пузырек газа-окислителя с ламинарным режимом движения ***III′***; ***IV*** и ***V*** – микроструктуры, получаемые при реализации процессов ***II*** и ***III***

The fracture surface was analyzed using a VHX-1000 optical microscope (“Keyence”, Japan) with expanded options due to improved long-focus system and digital processing of images. The 3D structures illustrated in Figs. 5, *e* and 6, *e*, were analyzed using the procedure for studying fracture surface in 3D image by means of the “e-Preview Optimal Image” regime [26], on the basis of which the most heterogeneous morphologically sites of fracture surface profile. The characteristic features of these fracture regions were analyzed in details using a JSM-IT300LV scanning electron microscope (“JEOL”, Japan) with energy and wavelength dispersive elemental analyzers.

Results and discussion

The fracture surfaces obtained upon static loading of the analyzed samples from dispersion strengthened composite materials were analyzed on samples destroyed at the maximum stress.

Figure 5, *a* illustrates macroscopic image of the fracture surface of flat DSCM sample 1 with 15 % of inclusions of solid phase. Mixed relief, heterogeneous in terms of macrogeometry is observed with crystalline pimples and breakaways. The fracture center and crack nucleation area are distinctly observed at the point of conglomeration of dispersed phase inclusions

(see Fig. 5, *b*, *c*). Analysis of the macrostructure in polarized light in Optimal Image regime (Fig. 5, *b*) and microstructure (Fig. 5, *d*) revealed secondary cracking. This can be caused by high normal tensile stresses as a consequence of the separation of matrix—solid phase interface along the plane of maxi-

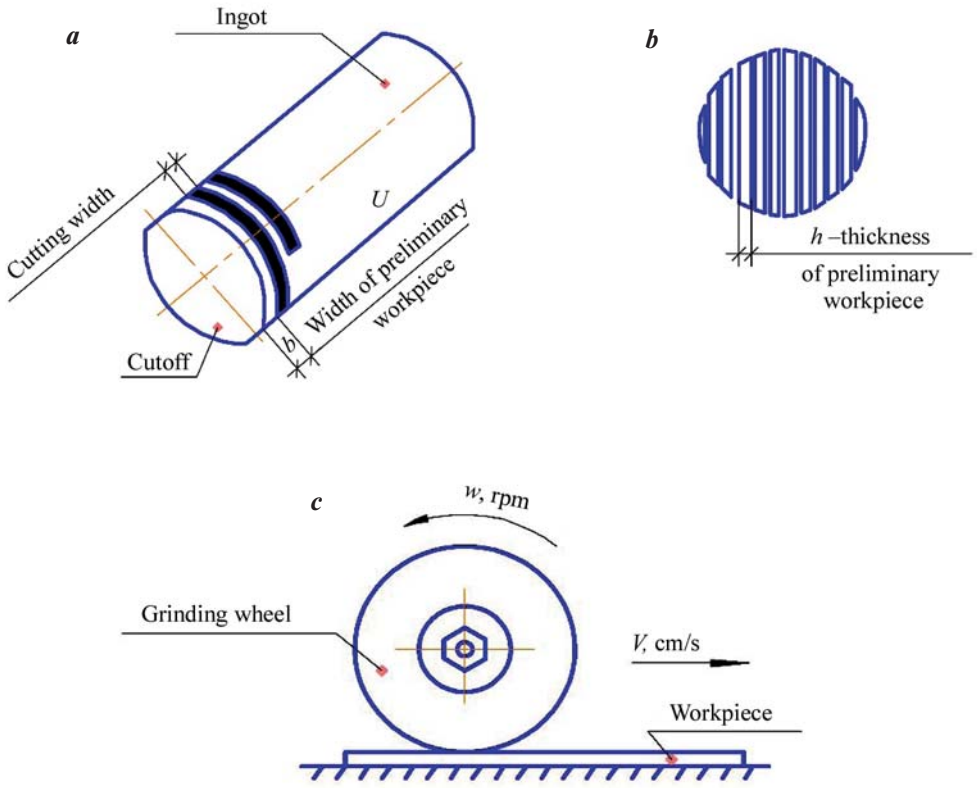

Fig. 2. Schematic view of fabrication of samples for tensile tests
a – transversal cutting of ingot, ***b*** – longitudinal cutting of workpiece, ***c*** – grinding of workpiece

Рис. 2. Схема изготовления образцов для испытаний на растяжение
a – поперечная резка слитка, ***b*** – продольная резка заготовки, ***c*** – шлифование заготовки

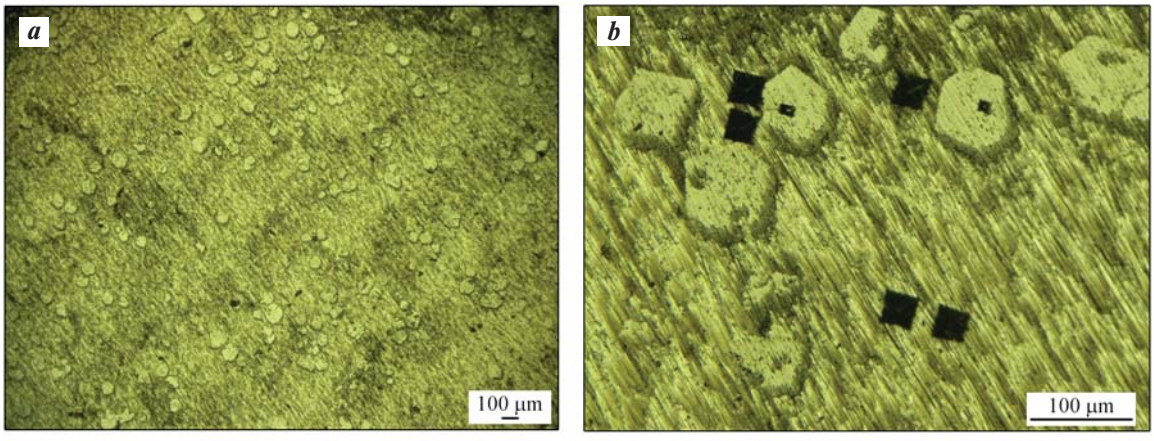

Fig. 3. Microstructure of the obtained material in initial state (***a***) and with indentation of pyramid with the weight of 100 g of PMT-3 hardness meter (***b***)

Рис. 3. Микроструктура полученного материала в исходном состоянии (***a***) и с отпечатками пирамидки массой 100 г твердомера ПМТ-3 (***b***)

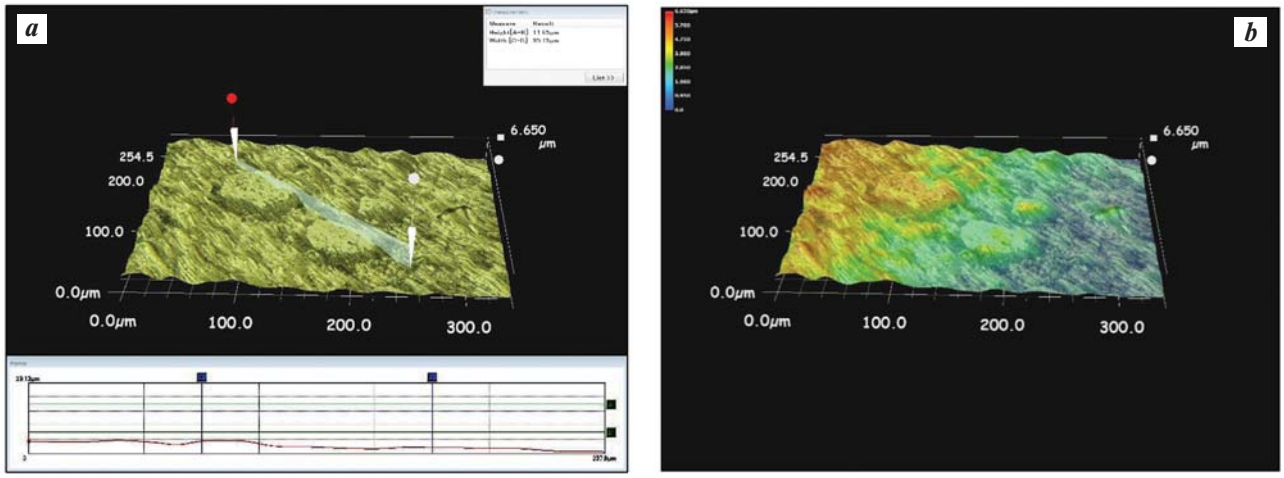

Fig. 4. Topographic image of surface and profile of samples

a – relief across the highlighted cross section with determination of height across this cross section; ***b*** – analysis of relief heights using colored image

Рис. 4. Топографическое отображение поверхности и профиль образцов

a – рельеф по выделенному сечению с определением высот по этому сечению; ***b*** –исследование высот рельефа с использованием цветного отображения

mum shear depending on orientation of each single grain.

The general macrogeometry of fracture surface is heterogeneous, however, individual sites were identified on it. They were characterized by morphologically unified fracture surfaces with nearly similar reliefs and existence of single type fracture elements. This is illustrated in Fig. 5, *e* in the form of degree of surface roughness in the direction perpendicular to the plane of load application, related to the stability of high energy propagation of crack upon fracture at these sites.

A relatively moderate amount of dispersed inclusions (in comparison with the second batch of samples) in the matrix of analyzed material located at significant distances leads to formation of moderate seams. This can be attributed to the fact of their bypassing by crack frontal zone, which is simpler than over the body of high solid phases. The profilogram distinctly illustrates a rather acute single change in the profile oriented at the angle ≈45° to the tension axis (see Fig. 5, *e*).

This is related to a slowing of crack growth and the blunting of its tip as a consequence of significant plastic deformation with formation of a cup-like structure and can be interpreted as a shear at this site characteristic for the shear area.

Microstructural studies (see Fig. 5, *d*) illustrate an alteration of crystalline segments and cleavage edges around oxides according to the transcrystalline mechanism with thin fibrous stripes. In some places a dendritic structure with intercrystallite fracture and quasi-cleavage can be observed.

The pattern of fracture surface of DSCM sample *2*, with 25 % of solid phase inclusions, is illustrated in Fig. 6. The fracture center is far from the tension axis but does not appear at the free surface of the sample. It is possible to observe a mixed fracture pattern, homogenous in terms of macrogeometry, with a fan-like fibrous structure (Fig. 6, *a*). In addition, crystalline pimples are detected which differ from previously considered samples by distribution over the fracture surface, as well as breakaways of other geometrical sizes. The higher amount of dispersive inclusions in the matrix of the analyzed material in comparison with DSCM *1*, located at shorter distances between themselves, smooths out the roughness at certain sites. This can be attributed to a decrease in the distance of bypassing of the solid phase by crack frontal zone. The profilogram (see Fig. 6, *e*), and the 3D structure, indirectly confirms the provisions discussed above. It does not contain morphologically heterogeneous in terms of macrogeometry area with significant differences of fracture surface relief.

Contrary to DSCM *1*, comprised of fibrous area and shear area, at some segments of fracture surface of sample *2* a radial area is detected (see Fig. 6, *c*, *d*). Its occurrence is related to an increase in the content of solid phase in alloy and characterizes transfer of crack from slow growth to its unsteady propagation with formation

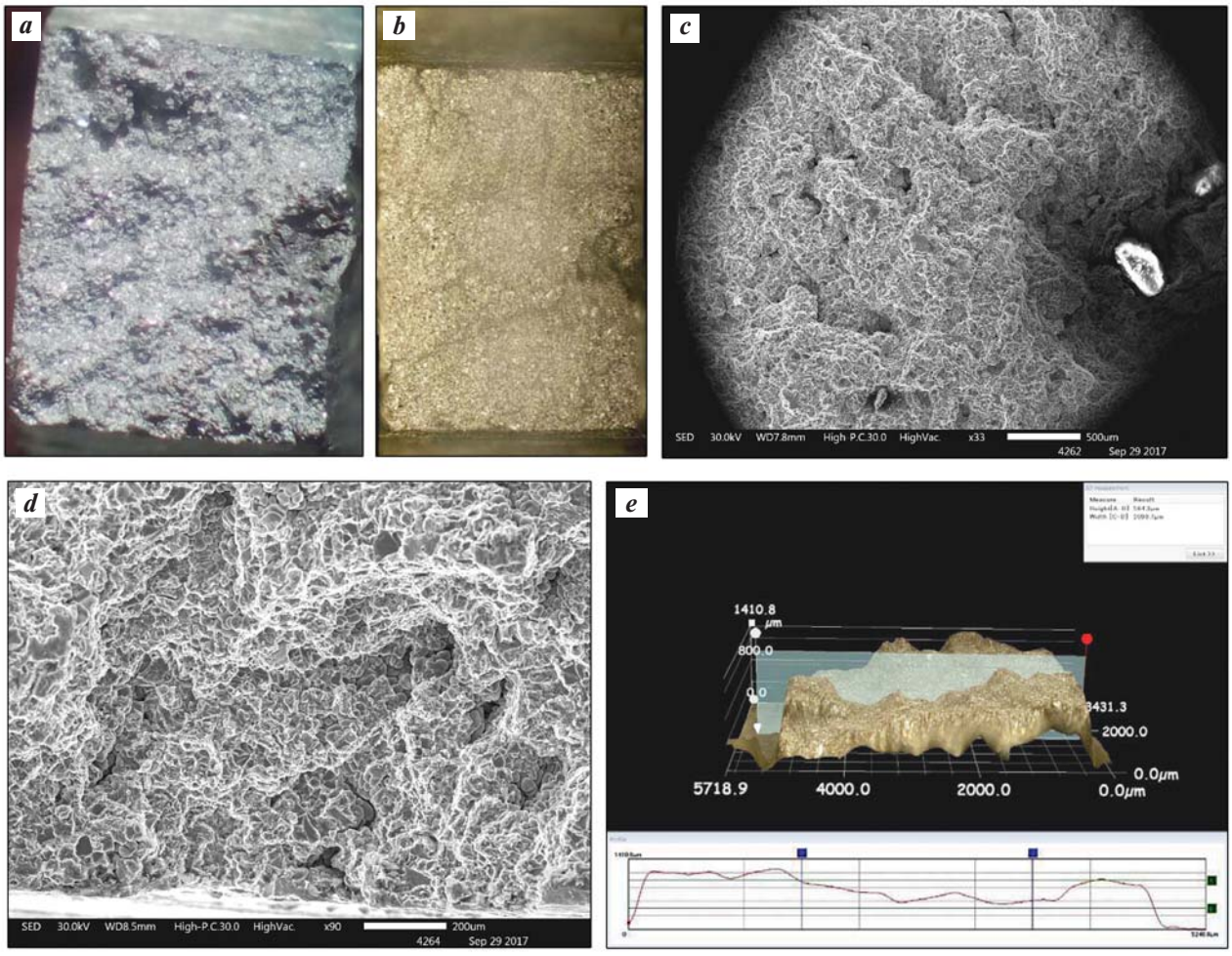

Fig. 5. Fracture surface of DSCM sample *1*

a – optical macrostructure (×40); ***b*** – macrostructure in Optimal Image regime; ***c*** and ***d*** – scanning electron microscopy; ***e*** – 3D structure with profilogram across the highlighted cross section

Рис. 5. Поверхность излома образца ДУКМ *1*

a – оптическая макроструктура (×40); ***b*** – макроструктура в режиме Optimal Image; ***c*** и ***d*** – результаты растровой электронной микроскопии; ***e*** – 3D-структура с профилограммой по выделенному сечению

of radial seams. It is possible to observe the chaotic alteration of viscous fracture according to the tearing mechanism and shear with a brittle cleavage fracture in the form of crystalline fracture. This fracture has stepwise relief and occurrence of dendritic sites with intercrystallite structure (see Fig. 6, *d*).

Such features are caused by the non-compliance of the general direction of crack propagation and the shortest direction from its front to a free surface. This is related to unsteady vortex crack propagation at a microlevel, characterized by stepwise (either fast or slow) propagation across the material body. However, in contrary to the DSCM sample *1* with lower content of solid phase inclusions, this is not related to the existence of single type fracture elements, but with an absolutely opposite fracture mechanism. This is comprised of the alteration of viscous fracture according to tearing and shearing mechanisms with consideration for brittle cleavage fracture at a separate fracture site surface (see Fig. 6, *d*).

Conclusions

The fracture surface of dispersion strengthened aluminum matrix material, with 15 % and 25 % content of dispersed phase exposed to deformation under conditions of static uniaxial tension was studied in this paper. The following differences in morphology of fracture surface were established.

In the material with lower Al_2O_3 content analyzed, the macroanalysis of fracture surface demonstrates

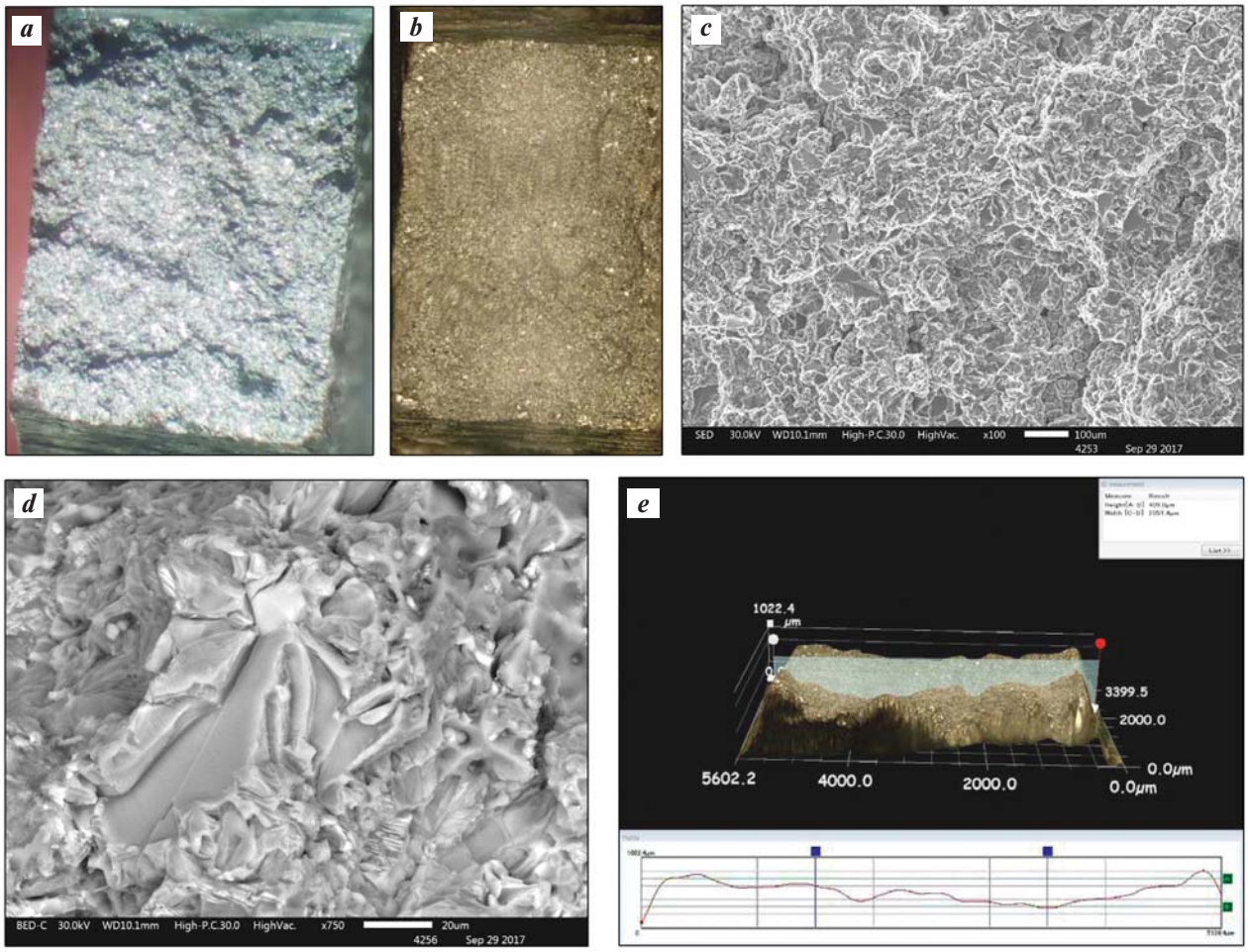

Fig. 6. Fracture surface of DSCM sample *2*

a – optical macrostructure (×40); ***b*** – macrostructure in Optimal Image regime; ***c*** and ***d*** – scanning electron microscopy; ***e*** – 3D structure with profilogram across the highlighted cross section

Рис. 6. Поверхность излома образца ДУКМ *2*

a – оптическая макроструктура (×40); ***b*** – макроструктура в режиме Optimal Image; ***c*** и ***d*** – результаты растровой электронной микроскопии; ***e*** – 3D-структура с профилограммой по выделенному сечению

mixed heterogeneous in terms of macrogeometry pattern. This can be characterized as a dry fibrous fracture, comprised of fibrous area and shear area and accompanied by secondary cracking.

With an increase in the content of solid phase, a radial area appears on the fracture surface, evidencing a change in the fracture mechanism and frontal zone of the main crack. The occurrence of features of the radial area is related to structural changes resulting from an increase in the content of solid phase in the alloy. This characterizes crack transfer from slow growth to its unstable propagation with formation of radial seams.

The structure of DSCM sample *2*, with 25 % content of strengthening phase, does not allow stable propagation of the crack. A higher amount of dispersed phases is a significant obstacle for its propagation, resulting in material strengthening. This consumes a significant portion of the fracture work. At higher (in comparison with the samples of the first batch) content of the strengthening phase in the material structure an obvious alteration of viscous fracture according to breakaway mechanism and shear with brittle fractures can be observed. However, the morphology of fracture surface becomes sufficiently homogeneous in terms of macrogeometry.

Analysis of fractures in the samples of the second batch did not reveal sharp differences in the relief. The profilograms were not characterized by any sharp relief drops or extreme values of the profile.

Therefore the macrostability of fracture processes can be stated, which cannot be attributed to fracture of DSCM sample *1*, where a rather strong single drop is observed.

References

1. Kablov E.N., Ospennikova O.G., Lomberg B.S. Strategic trends of development of structural materials and technologies of their processing for modern and future aircraft engines. *The Paton Welding Journal*. 2013;(11):23—32.
2. Liu Y. B., Lim S. C., Lu L., Lai M.O. Recent development in the fabrication of metal matrix-particulate composites using powder metallurgy techniques. *Journal of Materials Science*. 1994;29:1999—2007.
3. Gorbunov P.Z., Gal V.V. Promising dispersed-hardened composite materials. *Proizvodstvenno-tehnicheskij opyt*. 1993;1—2:81—84. (In Russ.).
   Горбунов П.З., Галь В.В. Перспективные дисперсно-упрочненные композиционные материалы. *Производственно-технический опыт*. 1993;(1-2):81—84.
4. Rohatgi P. Cast aluminum matrix composites for automotive applications. *JOM*. 1991;43(4):10—16.
5. Kurganova Y.A., Chernyshova T.A., Kobeleva L.I., Kurganov S.V. Service properties of aluminum-matrix precipitation-hardenet composite materials and the prospects of their use on the modern structural material market. *Russian metallurgy (Metally)*. 2011;(7):663—666.
6. Belov N.A., Belov V.D., Alabin A.N., Mishurov S.S. New generation of economically alloyed aluminum alloys. *Metallurgist*. 2010;54(5-6):311—316.
7. Lutz A.R., Galochkina I.A. Aluminum composite alloys are the alloys of the future. Samara: Samarskii gosudarstvennyi tekhnicheskii universitet, 2013. (In Russ.).
   Луц А.Р., Галочкина И.А. Алюминиевые композиционные сплавы — сплавы будущего. Самара.: СамГТУ, 2013.
8. Kurganova Yu.A. Prospects for the development of metal matrix composite materials for industrial purposes. *Servis v Rossii i za rubezhom*. 2012;3(30):235—240. (In Russ.).
   Курганова Ю.А. Перспективы развития металломатричных композиционных материалов промышленного назначения. *Сервис в России и за рубежом*. 2012;3(30):235—240.
9. Goswami R.K., Dhar Ajay, Srivastava A.K., Gurta Anil K. Effect of deformation and ceramic reinforcement on work hardening behavior of hot extruded 2124 Al—SiC metal matrix composites. *Journal of Composite Materials*. 1999;33(13):1160—1172.
10. NADCA Product SpecificationStandards for Die Casting: Aluminum, Aluminum-MMC, Copper, Magnesium, Zinc and ZA Alloys. 7-th ed. Wheeling, Illinois, 2009.
11. Moyal J.S., Lopez-Esteban S., Pecharroma'n C. The challenge of ceramic/metal microcomposites and nanocomposites. *Progress in Material Science*. 2007;52:1017—1090.
12. Kandalova E.G., Luts A.R., Makarenko A.G., Orlov A.V. Technology for the production of Al—TiC composite from powder exothermic mixtures directly in the aluminum melt. *Zagotovitel'nye proizvodstva v mashinostroenii*. 2005;(11):47—51. (In Russ.).
   Кандалова Е.Г., Луц А.Р., Макаренко А.Г., Орлов А.В. Технология получения композита Al—TiC из порошковых экзотермических смесей непосредственно в расплаве алюминия. *Заготовительные производства в машиностроении*. 2005;(11):47—51.
13. Kem A.Ju. Technological bases of production of powder and composite nanostructured materials and products. Rostov-on-Don: Izdatelskii centr, Donskoi gosudarstvennyi tekhnicheskii universitet, 2008. (In Russ.).
   Кем А.Ю. Технологические основы производства порошковых и композиционных наноструктурных материалов и изделий. Ростов-на-Дону: Изд. центр ДонГТУ, 2008.
14. Minaev A.M., Pruchkin V.A. On the internal oxidation of high-purity aluminum. *Voprosy sovremennoj nauki i praktiki*. 2011;(6):48—53. (In Russ.).
   Минаев А.М., Пручкин В.А. О внутреннем окислении высокочистого алюминия. *Вопросы современной науки и практики*. 2011;(6):48—53.
15. Mitra R., Mahagan Y.R. Interfaces in discontinuously reinforced metal matrix composites: An overview. *Bulletin of Materials Science*. 1995;18(4):405—434.
16. Afanas'ev V.K., Gertsen V.V., Dolgova S.V., Musohranov Ju.M. On the effect of water vapor on the formation of properties of high-silicon Al alloys. *Metallurgija mashinostroenija*. 2015;(5):17—22. (In Russ.).
   Афанасьев В.К., Герцен В.В., Долгова С.В., Мусохранов Ю.М. О влиянии водяного пара на формирование свойств высококремнистых Al-сплавов. *Металлургия машиностроения*. 2015;(5):17—22.
17. Muolo M.L., Passerone V.A., Passerone D. Oxygen influence on ceramics wettability by liquid metals Ag/α-Al_2O_3-experiments and modelling. *Materials Science and Engineering: A*. 2008;3(495):153—158.
18. Orlov A.V., Luts A.R., Kandalova E.G., Makarenko A.G. Technology for producing the Al—TiC composite from powder exothermic mixtures directly in the aluminum melt. *Zagotovitel'nye proizvodstva v mashinostroenii*. 2005;(11):54—61. (In Russ.).
   Орлов А.В., Луц А.Р., Кандалова Е.Г., Макаренко А.Г. Технология получения композита Al—TiC из порошковых экзотермических смесей непосредственно в расплаве алюминия. *Заготовительные производства в машиностроении*. 2005;(11):54—61.

19. Barathet V., Auradi V. Fractographic characterization of Al_2O_3 particulates reinforced Al2014 alloy composites subjected to tensile loading. *Frattura ed Integrità Strutturale*. 2021;57:14—23. https://doi.org/10.3221/IGF-ESIS.57.02
20. Olmos L., Martin Christophe L., Bouvard D. Sintering of mixtures of powders: Experiments and modelling. Powder Technology. 2009;190:134—140.
21. Agureev L.E., Kostikov V.I., Rizakhanov R.N., Eremeeva Zh.V., Barmin A.A., Savushkina S.V., Ashmarin A.A., Ivanov B.S., Rudshtein R.I. Aluminum powder composites reinforced by oxide nanoparticles used as microadditives. *International Journal of Nanomechanics Science and Technology*. 2014;5(3):201—211.
22. Chernyshov E.A., Romanova E.A., Romanov A.D., Romanov I.D., Mylnikov V.V. Elaboration of aluminium based metalmatrix composite manufacturing. In: *IOP Conference Series: Materials Science and Engineering*. 2019:012046.
23. Chernyshov E.A., Romanov A.D., Romanova E.A., Myl'nikov V.V. Development of technology for obtaining aluminum matrix cast composite material by synthesis of the hardening phase of aluminum oxide in aluminum melt. *Izvestija vuzov. Poroshkovaja metallurgija i funkcional'nye pokrytija*. 2017;(4):29—36. (In Russ.).
Чернышов Е.А., Романов А.Д., Романова Е.А., Мыльников В.В. Разработка технологии получения алюмоматричного литого композиционного материала с помощью синтеза упрочняющей фазы оксида алюминия в расплаве алюминия. *Известия вузов. Порошковая металлургия и функциональные покрытия*. 2017;(4):29—36. https://doi.org/10.17073/1997-308X-2017-4-29-36
24. Chernyshov E.A., Lonchakov S.Z., Romanov A.D., Myl'nikov V.V., Romanova E.A. Investigation of the microstructure of an alumomatric dispersed-filled cast composite material obtained by internal oxidation. *Perspektivnye materialy*. 2016;(9):78—83. (In Russ.).
Чернышов Е.А., Лончаков С.З., Романов А.Д., Мыльников В.В., Романова Е.А. Исследование микроструктуры алюмоматричного дисперсно-наполненного литого композиционного материала, полученного методом внутреннего окисления. *Перспективные материалы*. 2016;(9):78—83.
25. Khedera A.R.I., Marahleh G.S., Al-Jamea D.M.K. Strengthening of Aluminum by SiC, Al_2O_3 and MgO. *Jordan Journal of Mechanical and Industrial Engineering*. 2011;5(6):533—541.
26. Myl'nikov V.V., Romanov A.D., Chernyshov E.A. Studies of the influence of the amount of the hardening phase of a dispersed-hardened composite material based on aluminum on the regularities of the destruction process. *Izvestija vuzov. Poroshkovaja metallurgija i funkcional'nye pokrytija*. 2018;(3):55—63. (In Russ.).
Мыльников В.В., Романов А.Д., Чернышов Е.А. Исследования влияния количества упрочняющей фазы дисперсно-упрочненного композиционного материала на основе алюминия на закономерности процесса разрушения. *Известия вузов. Порошковая металлургия и функциональные покрытия*. 2018;(3):55—63.

Information about the authors

Vladimir V. Mylnikov – Cand. Sci. (Eng.), Associate Professor of the Department of Construction Technologies; Leading Researcher of the Department of Scientific Research, Innovation and Project Work; Head of the Laboratory of Strength and Plasticity of Functional Materials, Nizhny Novgorod State University of Architecture and Civil Engineering (NNGASU).
https://orcid.org/0000-0001-5545-4163
E-mail: mrmylnikov@mail.ru

Evgenii A. Chernyshov – Dr. Sci. (Eng.), Professor, Leading Researcher of the Department of Scientific Research, Innovation and Project Work, NNGASU.
https://orcid.org/0000-0002-3793-6043
E-mail: frfltvbrhft@mail.ru

Aleksei D. Romanov – Postgraduate Student, Nizhny Novgorod State Technical University n.a. R.E. Alekseev.
https://orcid.org/0000-0001-7504-6693
E-mail: t763@yandex.ru

Информация об авторах

Владимир Викторович Мыльников – к.т.н., доцент кафедры технологии строительства; вед. науч. сотрудник Управления научных исследований, инноваций и проектных работ; зав. лабораторией «Прочность и пластичность функциональных материалов», Нижегородский государственный архитектурно-строительный университет (ННГАСУ).
https://orcid.org/0000-0001-5545-4163
E-mail: mrmylnikov@mail.ru

Евгений Александрович Чернышов – д.т.н., проф., вед. науч. сотрудник Управления научных исследований, инноваций и проектных работ, ННГАСУ.
https://orcid.org/0000-0002-3793-6043
E-mail: frfltvbrhft@mail.ru

Алексей Дмитриевич Романов – аспирант, Нижегородский государственный технический университет им. Р.Е. Алексеева.
https://orcid.org/0000-0001-7504-6693
E-mail: t763@yandex.ru

Marina V. Mylnikova – Junior Researcher of the Department of Scientific Research, Innovation and Project Work, NNGASU.
https://orcid.org/0000-0001-6417-7591
E-mail: mpolivceva@yandex.ru

Evgenii A. Zakharychev – Cand. Sci. (Chem.), Head of the Laboratory of Polymer Materials, Research Institute of Chemistry of N.I. Lobachevsky National Research University; Junior Researcher of the Department of Scientific Research, Innovation and Project Work, NNGASU.
https://orcid.org/0000-0001-5941-4919
E-mail: zakharychev@list.ru

Nikolai A. Ryabov – Student, Technician of the Department of Scientific Research, Innovation and Project Works, NNGASU.
https://orcid.org/0000-0002-9037-4334
E-mail: nikolay.ryabov.04@mail.ru

Марина Владимировна Мыльникова – мл. науч. сотрудник Управления научных исследований, инноваций и проектных работ, ННГАСУ.
https://orcid.org/0000-0001-6417-7591
E-mail: mpolivceva@yandex.ru

Евгений Александрович Захарычев – к.х.н., зав. лабораторией полимерных материалов, НИИ химии, Нижегородский государственный университет им. Н.И. Лобачевского; мл. науч. сотрудник Управления научных исследований, инноваций и проектных работ, ННГАСУ.
https://orcid.org/0000-0001-5941-4919
E-mail: zakharychev@list.ru

Николай Алексеевич Рябов – студент, техник Управления научных исследований, инноваций и проектных работ, ННГАСУ.
https://orcid.org/0000-0002-9037-4334
E-mail: nikolay.ryabov.04@mail.ru

Contribution of the authors

V.V. Mylnikov – formation of the basic concept, statement of the purpose and objectives of the study, preparation of the text, formulation of conclusions.

E.A. Chernyshov – scientific guidance, correction of the text, correction of conclusions.

A.D. Romanov – testing samples, analysis of research results.

M.V. Mylnikova – correction of the text, correction of conclusions, analysis of research results.

E.A. Zakharychev – preparation of the experiment, conducting experiments, formulation of conclusions.

N.A. Ryabov – testing samples.

Вклад авторов

В.В. Мыльников – формирование основной концепции, постановка цели и задачи исследования, подготовка текста, формулировка выводов.

Е.А. Чернышов – научное руководство, корректировка текста, корректировка выводов.

А.Д. Романов – проведение испытаний образцов, проведение анализа результатов исследований.

М.В. Мыльникова – корректировка текста, корректировка выводов, анализ результатов исследований.

Е.А. Захарычев – подготовка эксперимента, проведение экспериментов, формулировка выводов.

Н.А. Рябов – проведение испытаний образцов.

The article was submitted 05.11.2022, revised 26.12.2022, accepted for publication 10.01.2023

Статья поступила в редакцию 05.11.2022, доработана 26.12.2022, подписана в печать 10.01.2023

UDC 669.017
https://doi.org/10.17073/0021-3438-2023-2-49-56

Research article
Научная статья

Mechanical properties and electrical conductivity of Al–Y–Sc–Er cold worked alloy

L.E. Gorlov, M.V. Glavatskikh, R.Yu. Barkov, A.V. Pozdniakov

National University of Science and Technology "MISIS"
4 bld. 1 Leninkiy Prosp., Moscow 119049, Russia

✉ Leonid E. Gorlov (gorlov@edu.misis.ru)

Abstract: Aluminum alloys alloyed with rare earth and transition metal are promising materials for electric energy transportation due to their high properties of strength, thermal stability, and electrical conductivity. The features of strengthening, their mechanical properties and electrical conductivity of Al–0.2Y–0.2Sc–0.3Er alloy after cold rolling have been established. The alloy as a cast structure is presented by aluminum solid solution (Al) and dispersed eutectics with τ_2 ($Al_{75-76}Er_{11-17}Y_{7-14}$) phase upon complete dissolution of scandium in (Al), and a content of yttrium and erbium at the level of 0.2–0.3 % each. Cold rolling the ingot accelerates strengthening upon annealing at 270 and 300 °C, reducing the time of achieving peak hardness. The maximum strengthening due to precipitation of $L1_2$ dispersoid of $Al_3(Sc,Y,Er)$ phase with the average particle size up to 10 nm is achieved after 7 h of annealing at 300 °C after cold rolling. This shows the prevailing heterogeneous mechanism of nucleation due to defects accumulated during cold rolling which stimulates strengthening. The eutectic particles are located mainly along the boundaries, elongated in the rolling direction. Irrespective of the mode of sheet fabrication, the alloy demonstrates high thermal stability up to 400 °C. During annealing of the sheets to 450 °C, their non-recrystallized structure is retained. Ingot annealing at t = 300 °C in 7 h and cold rolling with subsequent annealing under the same conditions provide a high level of mechanical properties and electrical conductivity: $\sigma_{0.2}$ = 194 MPa, σ_u = 210 MPa, δ = 12.1 % and IACS – 60,1 %. The alloy has demonstrated high yield stress up to 100 h of annealing at t = 300 °C.

Keywords: aluminum alloys, scandium, yttrium, recrystallization, mechanical properties, electrical conductivity

Acknowledgments: This work was supported by the grants НШ-1752.2022.4 and МК 3457.2022.4.

For citation: Gorlov L.E., Glavatskikh M.V., Barkov R.Yu., Pozdniakov A.V. Mechanical properties and electrical conductivity of Al–Y–Sc–Er cold worked alloy. *Izvestiya. Non-Ferrous Metallurgy.* 2023;29(2):49–56. https://doi.org/10.17073/0021-3438-2023-2-49-56

Механические свойства и электропроводность холоднодеформированного сплава Al–Y–Sc–Er

Л.Е. Горлов, М.В. Главатских, Р.Ю. Барков, А.В. Поздняков

Национальный исследовательский технический университет «МИСИС»
119049, Россия, г. Москва, Ленинский пр-т, 4

✉ Леонид Евгеньевич Горлов (gorlov@edu.misis.ru)

Аннотация: Алюминиевые сплавы, легированные редкоземельными и переходными металлами, являются перспективными материалами для транспортировки электроэнергии ввиду высоких показателей прочности, термической стабильности и электропроводности. В работе определены особенности упрочнения, механические свойства и электропроводность сплава

Al–0,2Y–0,2Sc–0,3Er после холодной прокатки. Литая структура сплава представлена алюминиевым твердым раствором (Al) и дисперсной эвтектикой с фазой τ_2 ($Al_{75-76}Er_{11-17}Y_{7-14}$) при полном растворении скандия в (Al) и содержании иттрия и эрбия на уровне 0,2–0,3 % каждого. Холодная прокатка слитка ускоряет упрочнение при отжиге при температурах 270 и 300 °С, уменьшая время достижения пиковой твердости. Максимальное упрочнение за счет выделения $L1_2$-дисперсоидов фазы $Al_3(Sc,Y,Er)$ со средним размером частиц до 10 нм достигается после 7 ч отжига при температуре 300 °С после холодной прокатки, что говорит о превалировании гетерогенного механизма зарождения за счет дефектов, накопленных в процессе холодной прокатки, стимулирующих упрочнение. Частицы эвтектики располагаются преимущественно вдоль границ, вытягиваясь в направлении прокатки, и вне зависимости от режима получения листа сплав демонстрирует высокую термическую стабильность до 400 °С. В процессе отжига листов до 450 °С сохраняется нерекристаллизованная структура. Отжиг слитка при t = 300 °С в течение 7 ч и холодная прокатка с последующим отжигом в тех же условиях обеспечивают высокий уровень механических свойств и электропроводности: $\sigma_{0,2}$ = 194 МПа, $\sigma_в$ = 210 МПа, δ = 12,1 % и IACS – 60,1 %. Сплав продемонстрировал высокую стабильность предела текучести вплоть до 100 ч отжига при t = 300 °С.

Ключевые слова: алюминиевые сплавы, скандий, иттрий, рекристаллизация, механические свойства, электропроводность

Благодарности: Работа выполнена при финансовой поддержке грантов НШ-1752.2022.4 и МК 3457.2022.4.

Для цитирования: Горлов Л.Е., Главатских М.В., Барков Р.Ю., Поздняков А.В. Механические свойства и электропроводность холоднодеформированного сплава Al–Y–Sc–Er. *Известия вузов. Цветная металлургия.* 2023;29(2):49–56.
https://doi.org/10.17073/0021-3438-2023-2-49-56

Introduction

Strengthening Al—Sc alloys during annealing of ingots provides formation of structured $L1_2$ dispersoids [1—11]. Additional doping with zirconium leads to an increase in thermal stability of the precipitates due to formation of $L1_2$ dispersoids of $Al_3(Sc_xZr_y)$ phase [12—19]. In this way, high strength conductive alloys were developed on the basis of Al—Sc—Zr system [20, 21]. Al—0.35Sc—0.2Zr[1] alloy after heat deformation treatment is characterized by a good combination of strength (σ_u = 210 MPa), plasticity (δ = 7.6 %), and electrical conductivity (IACS — 60.2 %) [20]. A less expensive alloy containing 0.06 % Sc has lower strength (194 MPa) at higher electrical conductivity (IACS — 61 %) [21].

In recent years much attention has been paid to other rare earth metals (REM), in particular, to Y, Yb, Er, and Gd [22—34]. Minor amounts during crystallization are present in aluminum solid solution. Upon annealing in alloys with scandium they substitute in $L1_2$ dispersoids, thus increasing the density of their precipitation and mechanical properties of the alloys [22—31]. Thus, for example, Al—0.2Y—0.2Sc alloy after rolling and annealing demonstrated a good combination of the properties: the yield stress up to 183 MPa, the ultimate strength up to 202 MPa, the relative elongation up to 15.8 % at the electrical conductivity of 60.8—61.5 % [31]. Further strengthening was achieved after additional doping with 0.3 % ytterbium [32]. As a consequence, in Al—0.2Y—0.2Sc—0.3Yb alloy the ultimate strength increased to 244 MPa with a decrease in plasticity to 7.6—11.9 % and electrical conductivity to 57—57.7 % [32]. Approximately the same level of properties was obtained in the sheets from Al—0.3Er—0.2Sc—0.2Yb alloy due to precipitation of dispersoids with the size of 4—8 nm [33]. For the aim of comparison, dispersoids of $Al_3(Er,Y,Zr)$ phase in scandium free Al—0.3Er—0.2Y—0.2Zr alloy provide lower strengthening ($\sigma_u \le 156$ MPa) at the same electrical conductivity [34].

In [35], a significant influence of annealing before deformation on mechanical properties and electrical conductivity of new Al—0.2Y—0.2Sc—0.3Er alloy was demonstrated. Ingot annealing, hot and cold rolling with subsequent annealing provide the following combination of properties: $\sigma_{0.2}$ = 191 MPa, σ_u = 207 MPa, δ = = 14 % and IACS — 59.7 %.

The aim of this work is to establish the influence of heat treatment on the properties of cold deformed conductive Al—0.2Y—0.2Sc—0.3Er alloy.

Experimental

Al—0.2Y—0.2Sc—0.2Er (AlYScEr) alloy was smelted in a resistance furnace from aluminum with a purity of 99.99 %, and dopants: Al—9Y, Al—2Sc and Al—10Er. The ingots were 40 mm wide, 20 mm thick and 120 mm height, and obtained by crystallization in copper water cooled mold at the cooling rate of ≈15 K/s. Rolling of ingots in a cast state (T1) and after annealing at t = 300 °C in 7 h (T2) was carried

[1] Hereinafter the contents of components are in wt.%, if not otherwise mentioned.

out at ambient temperature to the thickness of 1 mm. The microstructure studies were carried out using an Axiovert 200MMAT optical microscope (OM) (Carl Zeiss, Germany), a TESCAN VEGA 3LMH scanning electron microscope (SEM) (Czech Republic), a JEM 2100 transmission electron microscope (TEM) (Japan). Samples for PEM were prepared using a Struers Tenupol-5 facility of electrolytic pulsing (Denmark). Vickers hardness was measured using a Wilson/Wolpert 930N hardness meter (Germany) at the load of 5 kg.

Uniaxial tensile tests were carried out using a Zwick/Roell Z250 facility (Germany) at a deformation rate of $3 \cdot 10^{-3}$ s^{-1}. Samples with an operating length of 20 mm and width of 6 mm were cut out from a sheet in the rolling direction.

Electric resistance was measured on samples with a length of 70 mm and a width of 5 mm, cut from sheets using the double bridge method on an INSTEK GOM-802 ohmmeter (China).

Results and discussion

The initial ingot microstructure and phase composition of AlYScEr alloy were studied in detail in [35]. Aluminum solid solution (Al) and dispersed eutectics with τ_2 ($Al_{75-76}Er_{11-17}Y_{7-14}$) phase are presented in the as cast structure. Herewith, scandium is totally dissolved in (Al), and the content of yttrium and erbium is at a level of 0.2—0.3 %. The maximum strengthening due to precipitations of $L1_2$ dispersoids of Al_3(Sc,Y,Er) alloy was achieved after 7 h annealing at 300 °C.

Figure 1 illustrates the microstructure of alloy ingot after annealing providing the maximum hardness. The size of the precipitates does not exceed 10 nm. The particles of Al_3(Sc,Y,Er) phase are highlighted in TEM images, the diffraction pattern contains respective reflections located between main ones from the lattice (Al).

Figure 2 illustrates the microstructure and distribution of dopants between the phases in the highlighted

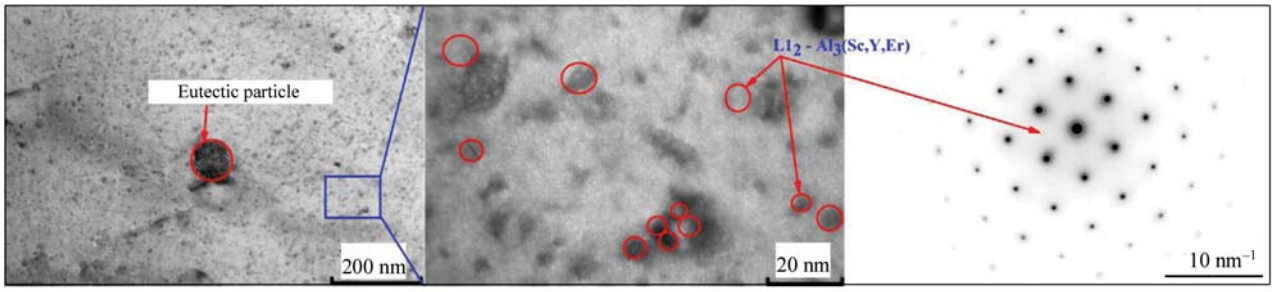

Fig. 1. Microstructure (TEM) and diffraction pattern of AlYScEr alloy after annealing at t = 300°C in 7 h

Рис. 1. Микроструктура (ПЭМ) и микроэлектронограмма сплава AlYScEr после отжига при t = 300 °С в течение 7 ч

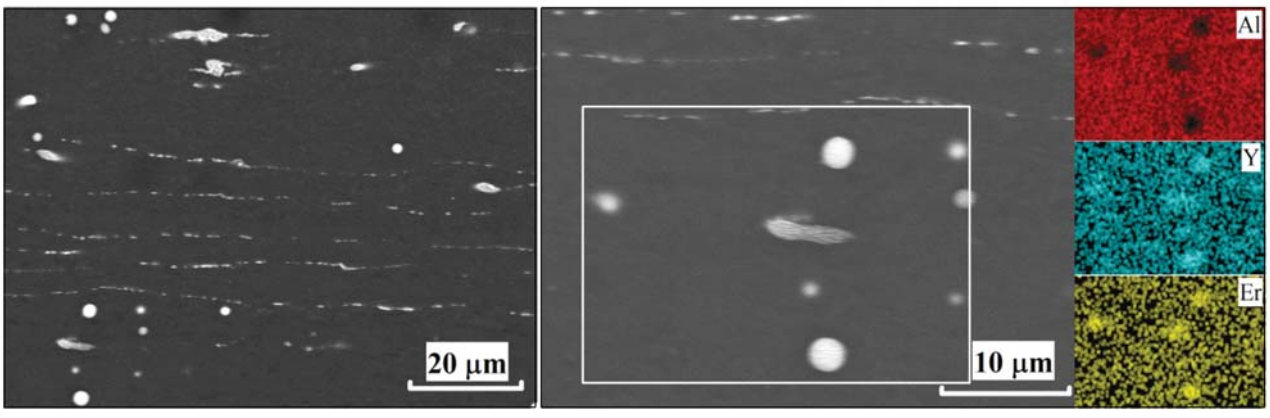

Fig. 2. Microstructure (SEM) and distribution of dopants between the phases in highlighted region in cold rolled state as exemplified by mode T1

Рис. 2. Микроструктура (СЭМ) и распределение легирующих элементов между фазами в выделенной области в холоднокатаном состоянии на примере режима Т1

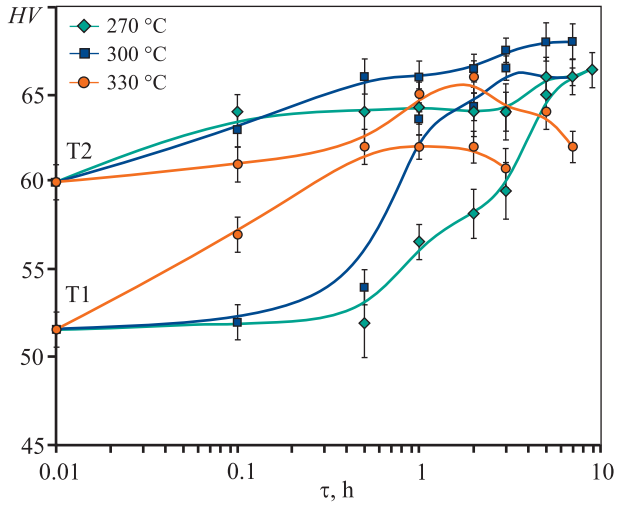

Fig. 3. Hardness as a function of annealing time at various temperatures

Рис. 3. Зависимости твердости от времени отжига при разных температурах

region in a cold rolled state, as exemplified by a sheet fabricated according to mode T1. The eutectic particles are located mainly along the boundaries, being elongated in the rolling direction.

After rolling, the sheets were annealed at 270—330 °C. Figure 3 illustrates hardness as a function of annealing time. In the sheets fabricated according to mode T1 (cold rolling of ingot), significant strengthening occurs. With an increase in the temperature from 270 to 300 °C, the same maximum hardness of 66 HV is achieved after 7 and 3 h, respectively. For the aims of comparison, in an ingot during annealing at t = 300 °C the maximum hardness (61 HV) is achieved in 7 h, and at 270 °C in 24 h [35].

Cold rolling significantly accelerates decomposition of (Al), allowing a greater hardness in sheets to be achieved, in comparison with ingots. Defects accumulated during cold rolling stimulate strengthening due to precipitation of $L1_2$ dispersoids, thus showing the prevailing heterogeneous mechanism of nucleation. The same argument can be confirmed by analysis of hardness evolution of samples fabricated according to mode T2. The annealing of sheets annealed before rolling to maximum hardness at 270—300 °C leads to increase in hardness by 6—8 HV. Thus, thermal stimulus is insufficient for complete decomposition of solid solution upon ingot annealing. In combination with the subsequent cold rolling and annealing at t = = 300 °C in 5—7 h, AlYScEr alloy demonstrates maximum hardness: 68 HV. During annealing at t = 330 °C, a certain strengthening is also observed, which in ≈1 h is superseded by polygonization processes leading to

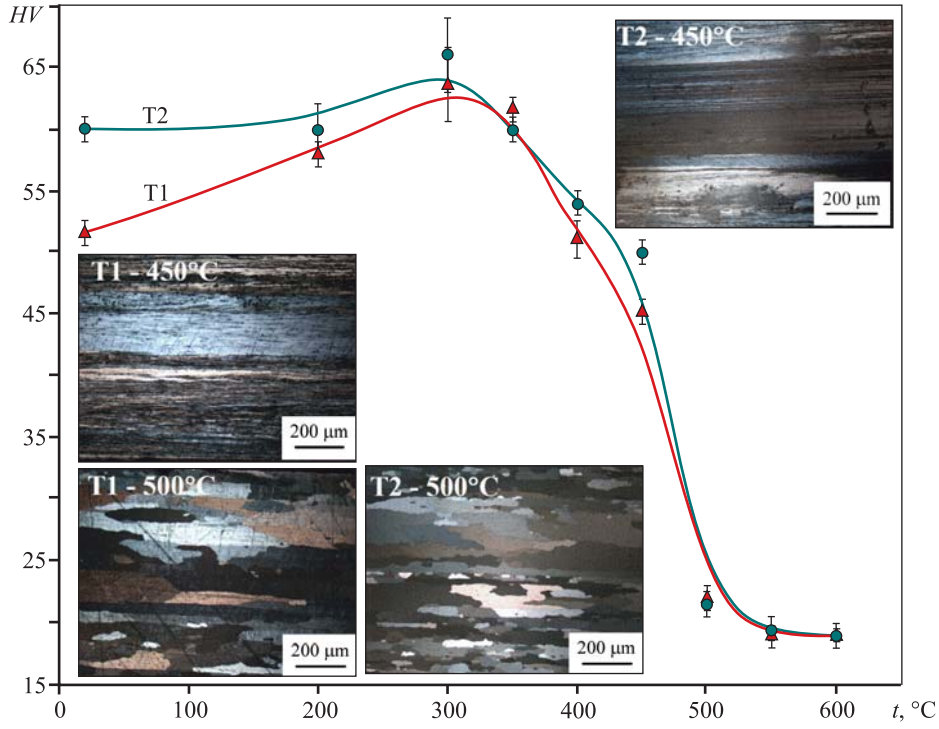

Fig. 4. Hardness as a function of temperature of 1 h annealing and granular structure (OM) of sheets

Рис. 4. Зависимости твердости от температуры 1-часового отжига и зеренная структура (СМ) листов

decrease in the hardness together with coarsening of dispersoids.

Figure 4 illustrates the hardness as a function of temperature of 1h annealing, and the granular structure of sheets in the range of recrystallization temperature. During annealing to 450 °C, the non-recrystallized structure retains in the alloy, the hardness decreases insignificantly (to 45 and 50 HV) in the sheets fabricated according to modes T1 and T2, respectively. A greater hardness in the sample according to mode T2 (annealing before rolling) evidences formation of more disperse and homogeneous polygonised structure. Similar results were achieved in [35] for the same alloy exposed to preliminary annealing, hot and cold rolling. A sharp decrease in the hardness to 19 HV occurs after 1 h annealing at t = 550 °C, when the structure is completely recrystallized. Irrespective of the mode of sheet fabrication, the alloy demonstrates a high thermal stability up to 400 °C, the hardness is 51—54 HV.

Table 1 summarizes the experimental results of uniaxial tensile tests of samples of AlYScEr alloy fabricated according to different modes. After rolling (mode T1), the ingot has a yield stress $\sigma_{0.2}$ = 167 MPa. During annealing at t = 300 °C, this property increases to 192 MPa in 4 h and actually does not decrease upon subsequent increase in annealing time to 100 h.

The alloy fabricated according to mode T1 is characterized by high thermal stability. The sheet preliminary annealed before rolling (T2) has $\sigma_{0.2}$ = 195 MPa. With an increase in the annealing time at t = 300 °C from 1 to 7 h, the yield stress actually does not change and after 100 h it insignificantly decreases to 180 MPa. Herewith, the relative elongation (δ) increases with an increase in the annealing time due to depletion (Al) and decrease in the concertation of defects.

For the same reasons, the electrical conductivity increases in sheets with increase in annealing duration at t = 300 °C (Table 2). After 100 h annealing, the electrical conductivity of the new alloy is close to that of the electrotechnical alloy 1350 (A5E), which has a significantly lower yield stress (110 MPa) [36]. The mode T2 provides better electrical conductivity. For the aims of comparison, the conductive alloy A5E has lower ultimate strength in annealed state σ_u = 120÷160 MPa, at approximately the same electrical conductivity IACS — 60.5 % (specific electric resistance: 0.0285 Ω·mm^2/m) [37].

Table 1. **Experimental results of tensile tests of sheets from AlYScEr alloy fabricated according to different modes**
Таблица 1. Результаты испытаний на растяжение листов сплава AlYScEr, полученных по разным режимам

State	T1			T2		
	$\sigma_{0.2}$, MPa	$\sigma_в$, MPa	δ, %	$\sigma_{0.2}$, MPa	$\sigma_в$, MPa	δ, %
Deformed	167±1	174±1	11±1	195±1	205±1	7±1
After annealing						
t = 300 °C, 1 h	186±2	198±2	8±1	198±3	212±2	7±2
t = 300 °C, 4 h	192±2	204±1	9±1	195±2	210±1	13.5±1.5
t = 300 °C, 7 h	190±1	205±1	12±4	194±1	210±1	12.1±0.5
t = 300 °C, 100 h	189±1	205±1	13±1	180±1	197±1	12.8±0.8

Table 2. **Electrical conductivity of sheets from AlYScEr alloy, aluminum, and electrotechnical alloy 1350 (A5E)**
Таблица 2. Электропроводность листов сплава AlYScEr, алюминия и электротехнического сплава 1350 (A5E)

State	IACS, %			
	T1	T2	Al (99,99%) [36]	1350 [36]
Deformed	54.4	58.1	64.5	61
After annealing				
t = 300 °C, 1 h	57.7	59.0		
t = 300 °C, 4 h	59.4	59.8		
t = 300 °C, 7 h	59.6	60.1		
t = 300 °C, 100 h	59.8	60.5		

Conclusions

The strengthening features, the mechanical properties, and the electrical conductivity of Al—0.2Y—0.2Sc—0.3Er alloy after cold rolling were determined.

1. The cold rolling of ingots accelerates strengthening upon annealing at $t = 270$ and 300 °C, thus decreasing the time to achieve peak hardness from 24 and 7 h for an ingot to 7 and 3 h for a sheet, respectively. The defects accumulated during cold rolling stimulate strengthening due to precipitation of $L1_2$ dispersoids. This shows the prevailing heterogeneous mechanism of dispersoid nucleation.

2. During the annealing of sheets to 450 °C, the non-recrystallized structure retains. The hardness of sheets produced according to modes T1 (ingot rolling) and T2 (rolling after annealing to maximum hardness) equals to 45 and 50 HV, respectively. The greater hardness of a sample fabricated according to mode T2 shows evidence of the formation of more disperse and homogeneous polygonised structure in it.

3. Ingot annealing at $t = 300$ °C in 7 h and cold rolling with subsequent annealing at 300 °C in 7 h provides a high level of mechanical properties and electrical conductivity: $\sigma_{0.2} = 194$ MPa, $\sigma_u = 210$ MPa, $\delta = 12.1$ % and IACS — 60.1 %.

References

1. Drits M.E., Dutkiewicz J., Toropova L.S., Salawa J. The effect of solution treatment on the ageing processes of Al—Sc alloys. *Crystal Research and Technology*. 1984;19:1325—1330. https://doi.org/10.1002/crat.2170191014
2. Drits M.Ye., Ber L.B., Bykov Yu.G., Toropova L.S., Anastaseva G.K. Aging of alloy Al—0.3at.%Sc. *Physics of Metals and Metallography*. 1984;57(6):118—126.
3. Blake N., Hopkins M.A. Constitution and age hardening of Al—Sc alloys. *Journal of Materials Science*. 1985;20:2861—2867. https://doi.org/10.1007/BF00553049
4. Torma T., Kovács-Csetényi E., Turmezey T., Ungár T., Kovács I. Hardening mechanisms in Al—Sc alloys. *Journal of Materials Science*. 1989;24:3924—3927. https://doi.org/10.1007/bf01168955
5. Brodova I.G., Polents I.V., Korzhavina O.A., Popel P.S., Korshunov I.P., Esin V.O. Structural investigations of rapidly crystallized Al—Sc alloys. *Melts Moscow*. 1992;4(5):392—397.
6. Nakayama M., Furuta A., Miura Y. Precipitation of Al_3Sc in Al—0.23wt.%Sc alloy. *Materials Transactions*. 1997;38(10):852—857. https://doi.org/10.2320/matertrans1989.38.852
7. Norman A.F., Prangnell P.B., McEwen R.S. The solidification behaviour of dilute aluminium-scandium alloys. *Acta Materialia*. 1998;46:5715—5732. https://doi.org/10.1016/S1359-6454(98)00257-2
8. Hyde K.B., Norman A.F., Prangnell P.B. The growth morphology and nucleation mechanism of primary $L1_2$ Al_3Sc particles in Al—Sc alloys. *Materials Science Forum*. 2000;331-337:1013—1018. https://doi.org/10.4028/www.scientific.net/msf.331-337.1013
9. Davydov V.G., Rostova T.D., Zakharov V.V., Filatov Y.A., Yelagin V.I. Scientific principles of making an alloying addition of scandium to aluminium alloys. *Materials Science and Engineering: A*. 2000;280:30—36. https://doi.org/10.1016/S0921-5093(99)00652-8
10. Jones M.J., Humphreys F.J. Interaction of recrystallization and precipitation: the effect of Al_3Sc on the recrystallization behavior of deformed aluminium. *Acta Materialia*. 2003;51:2149—2159. https://doi.org/10.1016/S1359-6454(03)00002-8
11. Costa S., Puga H., Barbosa J., Pinto A.M.P. The effect of Sc additions on the microstructure and age hardening behaviour of as cast Al—Sc alloys. *Materials and Design*. 2012;42:347—352. https://doi.org/10.1016/j.matdes.2012.06.019
12. Fuller C.B., Seidman D.N., Dunand D.C. Mechanical properties of Al(Sc,Zr) alloys at ambient and elevated temperatures. *Acta Materialia*. 2003;51(16):4803—4814. https://doi.org/10.1016/S1359-6454(03)00320-3
13. Robson J.D. A new model for prediction of dispersoid precipitation in aluminium alloys containing zirconium and scandium. *Acta Materialia*. 2004;52:1409—1421. https://doi.org/10.1016/j.actamat.2003.11.023
14. Forbord B., Lefebvre W., Danoix F., Hallem H., Marthinsen K. Three dimensional atom probe investigation on the formation of $Al_3(Sc,Zr)$-dispersoids in aluminium alloys. *Scripta Materialia*. 2004;51:333. https://doi.org/10.1016/j.scriptamat.2004.03.033
15. Belov N.A., Alabin A.N., Eskin D.G., Istomin-Kastrovskii V.V. Optimization of hardening of Al—Zr—Sc cast alloys. *Journal of Materials Science*. 2006;41:5890—5899. https://doi.org/10.1007/S10853-006-0265-7
16. Knipling K.E., Karnesky R.A., Lee C.P., Seidman D.N. Precipitation evolution in Al—0.1Sc, Al—0.1Zr and Al—0.1Sc—0.1Zr (at.%) alloys during isochronal aging. *Acta Materialia*. 2010;58(15):5184-5195. https://doi.org/10.1016/j.actamat.2010.05.054
17. Song M., Fang Y. He S. Effects of Zr content on the yield strength of an Al—Sc alloy. *Journal of Materials Engineering and Performance*. 2011;20:377—381. https://doi.org/10.1007/s11665-010-9693-2
18. Rokhlin L.L., Bochvar N.R., Leonova N.P. Study of decomposition of oversaturated solid solution

in Al—Sc—Zr alloys at different ratio of scandium and zirconium. *Inorganic Materials: Applied Research*. 2011;2:517—520.
https://doi.org/10.1134/S2075113311050170

19. McNamara C.T., Kampe S.L., Sanders P.G., Swenson D.J. The effect of cold work on the precipitation and recrystallization kinetics in Al—Sc—Zr alloys. *Light Metals*. 2013;379—382.
https://doi.org/10.1007/978-3-319-65136-1_66
20. Guan R., Shen Y., Zhao Z., Wang X. A high-strength, ductile Al—0.35Sc—0.2Zr alloy with good electrical conductivity strengthened by coherent nanosized-precipitates. *Journal of Materials Science and Technology*. 2017;33:215—223.
https://doi.org/10.1016/j.jmst.2017.01.017
21. Liu L., Jiang J.-T., Zhang B., Shao W.-Z., Zhen L. Enhancement of strength and electrical conductivity for a dilute Al—Sc—Zr alloy via heat treatments and cold drawing. *Journal of Materials Science and Technology*. 2019;35(6):962—971.
https://doi.org/10.1016/j.jmst.2018.12.023
22. Harada Y., Dunand D.C. Microstructure of Al_3Sc with ternary transition-metal additions. *Materials Science and Engineering: A*. 2002;329/331:686—695.
https://doi.org/10.1016/S0921-5093(01)01608-2
23. Karnesky R.A., van Dalen M.E, Dunand D.C., Seidman D.N. Effects of substituting rare-earth elements for scandium in a precipitation-strengthened Al—0.08at.%Sc alloy. *Scripta Materialia*. 2006;55(5):437—440.
https://doi.org/10.1016/j.scriptamat.2006.05.021
24. van Dalen M.E., Dunand D.C., Seidman D.N. Nanoscale precipitation and mechanical properties of Al—0.06at.%Sc alloys microalloyed with Yb or Gd. *Journal of Materials Science*. 2006;41:7814—7823.
https://doi.org/10.1007/S10853-006-0664-9
25. Rokhlin L.L., Dobatkina T.V., Bochvar N.R., Lysova E.V., Tarytina I.E. Effect of yttrium and chromium on the recrystallization of Al—Sc alloys. *Russian Metallurgy (Metally)*. 2007;335—339.
https://doi.org/10.1134/s0036029507040131
26. Harada Y., Dunand D.C. Microstructure of Al_3Sc with ternary transition-metal additions. *Intermetallics*. 2009;17(1-2):17—24.
https://doi.org/10.1016/j.intermet.2008.09.002
27. Karnesky R.A., Dunand D.C., Seidman D.N. Evolution of nanoscale precipitates in Al microalloyed with Sc and Er. *Acta Materialia*. 2009;57(14):4022—4031.
https://doi.org/10.1016/j.actamat.2009.04.034
28. Krug M.E., Werber A., Dunand D.C., Seidman D.N. Core—shell nanoscale precipitates in Al—0.06at.%Sc microalloyed with Tb, Ho, Tm or Lu. *Acta Materialia*. 2010;58(1):134—145.
https://doi.org/10.1016/j.actamat.2009.08.074
29. Rokhlin L.L., Bochvar N.R., Boselli J., Dobatkina T.V. Investigation of the phase relations in the Al-Rich alloys of the Al—Sc—Hf system in solid state. *Journal of Phase Equilibria and Diffusion*. 2010;31:327—332.
https://doi.org/10.1007/S11669-010-9710-Z
30. Van Dalen M.E., Dunand D.C., Seidman D.N. Microstructural evolution and creep properties of precipitation-strengthened Al—0.06Sc—0.02Gd and Al—0.06Sc—0.02Yb (at.%) alloys. *Acta Materialia*. 2011;59(13):5224—5237.
https://doi.org/10.1016/j.actamat.2011.04.059
31. Pozdniakov A.V., Barkov R.Yu. Microstructure and mechanical properties of novel Al—Y—Sc alloys with high thermal stability and electrical conductivity. *Journal of Materials Science and Technology*. 2020:1—6.
https://doi.org/10.1016/j.jmst.2019.08.006
32. Barkov R.Yu., Yakovtseva O.A., Mamzurina O.I., Loginova I.S., Medvedeva S.V., Proviryakov A. S., Mikhailovskaya A.V., Pozdniakov A.V. Effect of Yb on the Structure and Properties of an Electroconductive Al—Y—Sc Alloy. *Physics of Metals and Metallography*. 2020;121(6):604—609.
https://doi.org/10.1134/S0031918X20060022
33. Barkov R.Yu., Mikhaylovskaya A.V., Yakovtseva O.A., Loginova I.S., Prosviryakov A.S., Pozdniakov A.V. Effects of thermomechanical treatment on the microstructure, precipitation strengthening, internal friction, and thermal stability of Al—Er—Yb—Sc alloys with good electrical conductivity. *Journal of Alloys and Compounds*. 2021;855(1):157—367.
https://doi.org/10.1016/j.jallcom.2020.157367
34. Pozdniakov A.V., Barkov R.Yu., Prosviryakov A.S., Churyumov A.Yu., Golovin I.S., Zolotorevskiy V.S. Effect of Zr on the microstructure, recrystallization behavior, mechanical properties and electrical conductivity of the novel Al—Er—Y alloy. *Journal of Alloys and Compounds*. 2018;765:1—6.
https://doi.org/10.1016/j.jallcom.2018.06.163
35. Liu X., Du Y., Liu S., Cheng K., Zhang Z. Phase equilibria and crystal structure of ternary compounds in Al-rich corner of Al—Er—Y system at 673 and 873K. *Journal of Materials Science and Technology*. 2021;60:128—138.
https://doi.org/10.1016/j.jmst.2020.04.047
36. ASM Handbook. Properties and selection: Nonferrous alloys and special-purpose materials. V.2. The Materials Information Company, 2010.

Information about the authors

Leonid E. Gorlov – Student, Department of Physical Metallurgy of Non-Ferrous Metals, National University of Science and Technology (NUST) "MISIS".
https://orcid.org/0000-0002-1631-8772
E-mail: gorlov@edu.misis.ru

Mariya V. Glavatskikh – Graduate Student, Department of Physical Metallurgy of Non-Ferrous Metals, NUST MISIS.
https://orcid.org/0000-0002-1350-1440
E-mail: glavatskikh@edu.misis.ru

Ruslan Yu. Barkov – Cand. Sci. (Eng.), Assistant, Department of Physical Metallurgy of Non-Ferrous Metals, NUST MISIS.
https://orcid.org/0000-0003-1443-5577
E-mail: barkov@misis.ru

Andrei V. Pozdniakov – Cand. Sci. (Eng.), Associate Professor, Department of Physical Metallurgy of Non-Ferrous Metals, NUST MISIS.
https://orcid.org/0000-0002-3116-5057
E-mail: pozdniakov@misis.ru

Информация об авторах

Леонид Евгеньевич Горлов – студент кафедры металловедения цветных металлов (МЦМ), Национальный исследовательский технический университет «МИСИС» (НИТУ МИСИС).
https://orcid.org/0000-0002-1631-8772
E-mail: gorlov@edu.misis.ru

Мария Владимировна Главатских – аспирант кафедры МЦМ, НИТУ МИСИС.
https://orcid.org/0000-0002-1350-1440
E-mail: glavatskikh@edu.misis.ru

Руслан Юрьевич Барков – к.т.н., ассистент кафедры МЦМ, НИТУ МИСИС.
https://orcid.org/0000-0003-1443-5577
E-mail: barkov@misis.ru

Андрей Владимирович Поздняков – к.т.н., доцент кафедры МЦМ, НИТУ МИСИС.
https://orcid.org/0000-0002-3116-5057
E-mail: pozdniakov@misis.ru

Contribution of the authors

L.E. Gorlov – methodology, data processing, formal analysis, participated in discussion of results, wrote article

M.V. Glavatskikh – research, visualization, participated in the discussion of the results

R.Yu. Barkov – data processing, monitoring, obtaining funding, participated in discussion of results

A.V. Pozdniakov – conceptualization, writing and preparation of the initial draft, reviewing and editing

Вклад авторов

Л.Е. Горлов – методология, обработка данных, формальный анализ, участие в обсуждении результатов, подготовка текста статьи.

М.В. Главатских – исследование, визуализация, участие в обсуждении результатов.

Р.Ю. Барков – обработка данных, контроль, получение финансирования, участие в обсуждении результатов.

А.В. Поздняков – концептуализация, написание и подготовка первоначального проекта, рецензирование и научное редактирование.

The article was submitted 06.10.2022, revised 13.12.2022, accepted for publication 20.12.2022

Статья поступила в редакцию 06.10.2022, доработана 13.12.2022, подписана в печать 20.12.2022

UDC 621.791.725, 669.017.165
https://doi.org/10.17073/0021-3438-2023-2-57-73

Research article
Научная статья

Structure and mechanical properties of welded joints from alloy based on VTI-4 orthorhombic titanium aluminide produced by pulse laser welding

S.V. Naumov[1], D.O. Panov[1], R.S. Chernichenko[1], V.S. Sokolovsky[1], E.I. Volokitina[1], N.D. Stepanov[1], S.V. Zherebtsov[1], E.B. Alekseev[2], N.A. Nochovnaya[2], G.A. Salishchev[1]

[1] **Belgorod State University**
85 Pobeda Str., Belgorod, 308015, Russia

[2] **Federal State Unitary Enterprise "All-Russian Scientific Research Institute of Aviation Materials" (VIAM)**
17 Radio Str., Moscow 105005, Russia

✉ Stanislav V. Naumov (NaumovStanislav@yandex.ru)

Abstract: Ti_2AlNb-based alloys are promising materials for operation at high temperatures in aerospace industry. Meanwhile, the existing difficulties of weldability restrict opportunities of their application. This work is devoted to studies of welded joints from Ti_2AlNb-based VTI-4 alloy, obtained using pulsed laser welding (PLW). The optimum PLW modes have been determined providing uniform faultless joint. The features of formation of external defects, internal pores, cracks and non-uniform penetration depth were detected depending on welding conditions. The main PLW parameters influencing on formation of welded joint are voltage and duration of laser pulse. It was demonstrated that at insufficient medium and high peak powers sawtooth seam roots and internal pores can be formed. However, at higher rates of energy input thermal hydraulic processes in welding bathe are violated, accompanied by metal splashing (spattering), heterogeneity of pulse imposition is observed. This leads to formation of cracks, higher porosity, heterogeneity of melting zone, and as a consequence, poor mechanical properties. Microstructure analysis of the welded joints obtained by means of PLW has demonstrated that the melting area is comprised of long dendritic grains of β phase, and the heat affected zone from two regions of β + α_2 phases and β + α_2 + O phases. Herewith, the achieved joint strength equals to ~80 % of the base metal produced using the optimum PLW mode.

Keywords: Ti_2AlNb-based alloy, forging, pulsed laser welding, welded joint, EBSD analysis, mechanical properties

Acknowledgments: This work was supported by the Russian Science Foundation (Agreement No. 19-79-30066) using the equipment of BSU Shared Research Facilities "Technologies and Materials".

For citation: Naumov S.V., Panov D.O., Chernichenko R.S., Sokolovsky V.S., Volokitina E.I., Stepanov N.D., Zherebtsov S.V., Alekseev E.B., Nochovnaya N.A., Salishchev G.A. Structure and mechanical properties of welded joints from alloy based on VTI-4 orthorhombic titanium aluminide produced by pulse laser welding. *Izvestiya. Non-Ferrous Metallurgy*. 2023;29(2):57–73.
https://doi.org/10.17073/0021-3438-2023-2-57-73

Структура и механические свойства сварных соединений из сплава на основе орторомбического алюминида титана ВТИ-4, полученных импульсной лазерной сваркой

С.В. Наумов[1], Д.О. Панов[1], Р.С. Черниченко[1], В.С. Соколовский[1], Е.И. Волокитина[1], Н.Д. Степанов[1], С.В. Жеребцов[1], Е.Б. Алексеев[2], Н.А. Ночовная[2], Г.А. Салищев[1]

[1] **Белгородский государственный национальный исследовательский университет**
308015, Россия, г. Белгород, ул. Победы, 85

[2] **Всероссийский научно-исследовательский институт авиационных материалов (ВИАМ)**
105005, Россия, г. Москва, ул. Радио, 17

✉ Станислав Валентинович Наумов (NaumovStanislav@yandex.ru)

Аннотация: Деформируемые сплавы на основе Ti_2AlNb с повышенной технологичностью для изготовления листовых изделий являются перспективными материалами для работы при высоких температурах в аэрокосмической отрасли, однако возникающие трудности со свариваемостью ограничивают возможности их применения. Работа посвящена изучению сварных соединений из сплава ВТИ-4 на основе Ti_2AlNb, полученных с использованием импульсной лазерной сварки (ИЛС). Определены оптимальные режимы ИЛС, обеспечивающие равномерный бездефектный шов. Выявлены особенности образования внешних дефектов, внутренних пор, трещин и неравномерности глубины проплавления в зависимости от условий сварки. Основными параметрами ИЛС, влияющими на формирование сварного шва, являются напряжение и длительность импульса лазерного излучения. Показано, что при недостаточных средней и высокой пиковых мощностях возможно образование пилообразного корня сварного шва и внутренних пор. Однако при увеличенных погонных энергиях нарушаются термогидравлические процессы в сварочной ванне, что влечет за собой выплеск металла (разбрызгивание), наблюдается неравномерность наложения импульсов. Это приводит к образованию трещин, повышенной пористости, неоднородности зоны плавления и, как следствие, к низким механическим свойствам. Микроструктурное исследование сварных соединений из сплава ВТИ-4, полученных с использованием ИЛС, показало, что зона плавления состоит из крупных дендритных зерен β-фазы, а зона термического влияния – из двух областей β + α_2-фаз и β + α_2 + O-фаз. При этом достигнута прочность ~80 % от прочности основного металла сварного соединения из сплава ВТИ-4, полученного по оптимальному режиму ИЛС.

Ключевые слова: сплав на основе орторомбического алюминида титана, ВТИ-4, Ti_2AlNb, ковка, импульсная лазерная сварка (ИЛС), сварной шов (СШ), BSE анализ, EBSD анализ, механические свойства

Благодарности: Работа выполнена при финансовой поддержке РНФ (Соглашение № 19-79-30066) с использованием оборудования Центра коллективного пользования «Технологии и материалы НИУ “БелГУ”»).

Для цитирования: Наумов С.В., Панов Д.О., Черниченко Р.С., Соколовский В.С., Волокитина Е.И., Степанов Н.Д., Жеребцов С.В., Алексеев Е.Б., Ночовная Н.А., Салищев Г.А. Структура и механические свойства сварных соединений из сплава на основе орторомбического алюминида титана ВТИ-4, полученных импульсной лазерной сваркой. *Известия вузов. Цветная металлургия*. 2023;29(2):57–73. https://doi.org/10.17073/0021-3438-2023-2-57-73

Introduction

Ti_2AlNb-based alloys, for instance, Grade VTI-4, are characterized by low weight and are promising materials for operation at higher temperatures in aircraft and aerospace industry due to their low density, high specific strength and superior resistance against oxidation and creeping [1, 2]. In addition, they can run at higher temperatures in comparison with titanium alloys and their density is by ~40 % lower than that of superalloys based on Ni (5.1 g/cm^3 against 7.7—9.0 g/cm^3) [3—5]. At the same time, the technological properties of these

alloys (for instance, weldability) restrict opportunities of their application.

The strength of a welded joint of the Ti_2AlNb-based alloys exposed to argon arc welding barely achieves 80 % of that of the base metal [6]. Herewith, the plasticity of a welded joint (WJ) decreases, coarse dendritic structure is formed, and the action of electric arc of argon welding forms wide melting area (MA) and heat affected zone (HAZ) [7, 8], which leads to a deterioration of mechanical properties. The highly concentrated heating sources applied upon laser beam welding (LBW) or electron beam welding (EBW) with optimum technological parameters and subsequent thermal treatment can provide production of faultless high-strength WJ [9—12]. This is related with the fact that the heat input and its resulting influence on a microstructure of the base metal can be reduced to minimum during these processes [13].

LBW of titanium alloys, including Ti_2AlNb-based alloys [3, 14, 15], with repetitively pulsed laser Nd:YAG (PLW) produces WJ with good surface quality, minimum defects and superior comprehensive mechanical properties. WJ quality depends on such PLW parameters as traveling speed and average power of laser, energy and duration of pulse, average peak power density, laser spot surface area, and others. The numerous performances of PLW make it possible to control heat release with the accuracy unavailable previously for continuous LBW, and also allow a wide range of experimental conditions to be applied. This can influence on the size of MA dendritic structure, as well as the grain size of various areas of welded joint in general [16, 17]. On the other hand, controlling such high number of parameters complicates the PLW processing [17]. Finally, the violation of the processing can lead to cracking or pores formation [18, 19].

Despite the advantages of LBW and EBW, welding involving highly concentrated heating sources are accompanied by metal melting and formation of columnar B2 structure [13]. In addition, one of the main problems of PLW of titanium alloys is porosity [20]. It has been reported [21] that its formation during PLW is related with the dynamics of welding bath. This is influenced by welding process variables, destruction of keyhole, and solidification processes [22]. In addition, at a high temperature gradient in a liquid bath the protection has cannot escape after rapid solidification and forms a cavity in the seam root. The influence of a plasma channel is also known. Upon violation of welding this can lead to formation of vacuum pore in WJ [23]. In addition, formation of porosity in WJ is influenced by hydrogen [23—26] and evaporation of aluminum during welding [27]. Therefore, the production of faultless WJ from Ti_2AlNb-based alloys on is a complicated problem which requires for selection process variables of PLW. Thus, this work is devoted to determination of the influence of PLW process variables on geometrical sizes and defect structure of welded joints, structure and mechanical properties of WJ from a Ti_2AlNb-based alloy.

Experimental

The material for forging operations and subsequent welding procedures was presented from a plate of the Ti_2AlNb-based VTI-4 alloy (its chemical composition, at.%: Ti—23Al—23Nb—1.4V—0.8Zr—0.4Mo—0.4Si) obtained by triple remelting in a vacuum arc skull furnace. The multiaxial deformation of workpieces cut out from this plate with the sizes of 40×30×60 mm was achieved using a DEVR 1000 modified press (Russia) equipped with a MikroInstrument Miterm T3 heating furnace (Russia). During forging, the temperature of dies was 965 ± 5 °C. The preheating of workpiece to 970 °C was carried out in a Nabertherm furnace, mod. No. 321 400v3/N/PE (Germany) in 30 min. The multiaxial forging was comprised of *abc* deformation (Fig. 1, *a*) at the speed of <0.1 mm/s, i.e. consecutively in the directions of axes *a*, *b* and *c* with the deformation degree of 50 % in each case. In order to obtain hexagonal profile, at the last stage the obtained rectangle was drawn at the edges by 7 ± 2 mm. The forged workpiece was subsequently cooled in air. The external view of the workpiece after deformation is illustrated in Fig. 1, *b*.

The PLW was carried out using a LAT-S-300 laser facility (Russia) with repetitively pulsed impact of Nd:YAG laser (1.064 μm) equipped with an L-5010-A automated coordinate table and a L-101-ChPU controller. Samples in the form of plates with the sizes of 24 × 12.5 × 1.5 mm from the VTI-4 alloy were exposed to single side butt welding. The welding joints were selected in the voltage ranges of 280—320 V and pulse duration of 3—6 ms:

- rectangular pulse with the step between pulses of 0.25 mm;
- flow rate of protecting gas Q_g = 2.5 bar (argon 4.8);
- axial gas supply along the direction of laser radiation with holding of 5 s before start of welding;
- water flow rate Q_w = 0.5 m^3/h;
- focal distance: 0.0 mm (on the surface of welded workpieces);
- welding speed: 0.3 m/min.

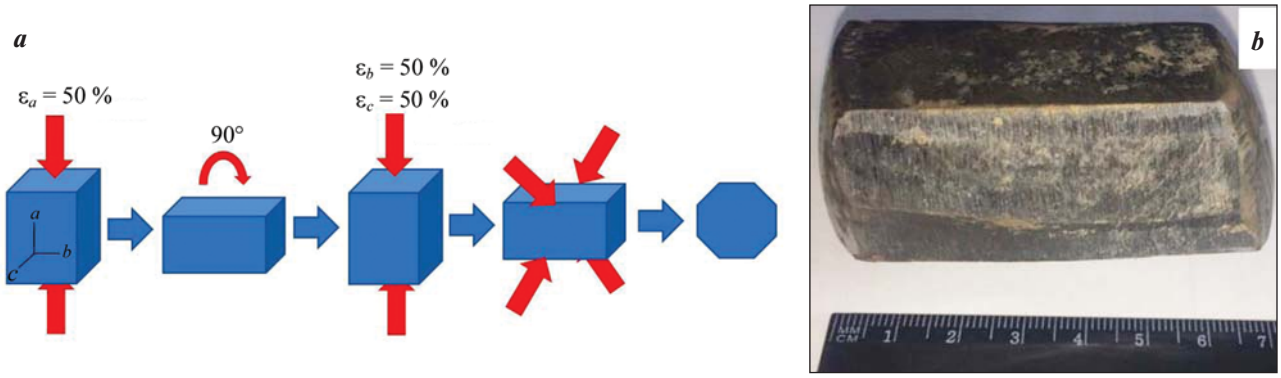

Fig. 1. Multiaxial forging of the VTI-4 alloy on a DEVR 1000 modified press
a – forging sequence; ***b*** – appearance of the forging obtained in the range t = 950÷975 °C

Рис. 1. Мультиосевая ковка сплава ВТИ-4 на модифицированном прессе DEVR 1000
a – схема ковки; ***b*** – внешний вид поковки, полученной в интервале t = 950÷975 °C

Depending on the welding mode (see Table) the peak power (P_{peak}) was varied from 2.17 to 3,21 kW, the average power was P_{avg} = 32÷90 W (Fig. 2). The PLW modes underwent preliminary testing on plates of the VTI-4 alloy. Herewith, the welding parameters were varied in a wider range. In addition, welding voltage and speed were selected on the basis of previous results [3, 14].

Samples for welding and subsequent mechanical tests were cut out using a Sodick VL400Q electric erosion machine (China) in accordance with the layout illustrated in Fig. 3, *a*. The surfaces of cutout plates before welding (24 × 12.5 × 1.5 mm) were polished using Struers SiC FEPA emery paper with a grain size of P220 (68 μm), and the surfaces of welded edges were polished using emery paper with the grain size P1000 (18 μm).

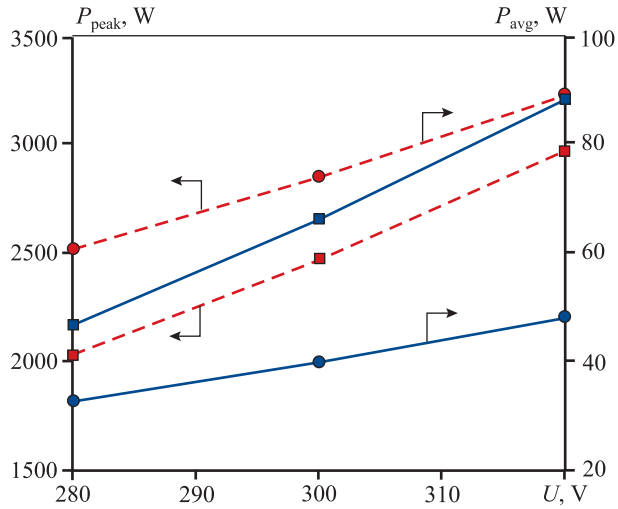

Fig. 2. Energy parameters of pulsed laser beam welding modes
τ = 3 ms (solid lines), τ = 6 ms (dashed lines)

Рис. 2. Энергетические параметры режимов ИЛС
τ = 3 мс (сплошные линии), τ = 6 мс (штриховые)

Modes of pulsed laser welding of VTI-4 alloy

Режимы импульсной лазерной сварки сплава ВТИ-4

PLW mode No.	Voltage U, V	Pulse duration τ, ms
1	280	3
2	300	3
3	320	3
4	280	6
5	300	6
6	320	6

The surfaces of samples for mechanical tests and microstructural studies were prepared also using emery paper with a grain size of P220 to P2000 (5—7 μm) at Baipol Metco (India) and Struers LaboPol-5 (Denmark) machines. The surface was polished using Struers MD Chem (Denmark) cloth polishing wheel with OP-S NonDry (SiC) suspension.

Before operation using an electron microscope, the polished surfaces were cleaned from impurities in a Sapphire ultrasound bath (35 kHz) in acetone in 15—30 min

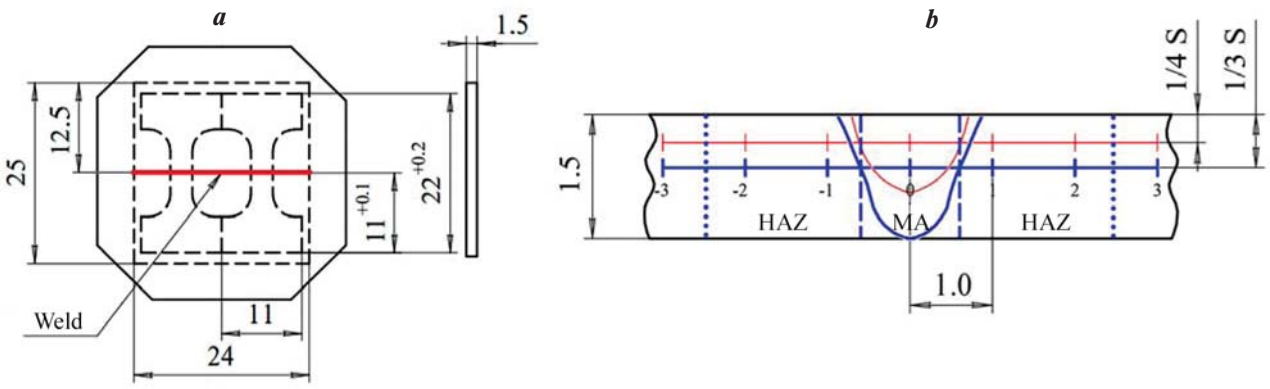

Fig. 3. Layout of sample preparation and microhardness measurement

a – cutting out of a sample from a forged workpiece for welding and subsequent uniaxial tensile testing;
b –measurement of microhardness in the cross section of the welded joint (0 – welded joint center)

Рис. 3. Схемы подготовки образцов и измерения микротвердости

a – резка образцов из поковки из сплава ВТИ-4 для сварки и последующих механических испытаний на одноосное растяжение;
b – измерение микротвердости в поперечном сечении сварного шва (0 – центр сварного шва)

with subsequent cleaning using a Plasma Cleaner Fischione machine (USA) in 30 min. The uniaxial tensile tests were performed using an Instron 5882 test machine (Great Britain) at ambient temperature at the loading rate of 10^{-3} s^{-1}.

Microhardness was determined on polished samples in transversal cross section of welded joints according to ISO 22826. The measurements were carried out with a step of 0.15 mm at a distance of 1/3 and 1/4 of the plate thickness depending on the depth of penetration (Fig. 3, *b*). The measurements were carried out using a Vickers 402MVD hardness meter (the Netherlands) with a load of 0.2 kg and an indentation time of 10 s ($HV_{0.2}$). Control and data acquisition were carried out using Hardtest Wolpert Group software (the Netherlands).

Microstructural studies were carried out using a Nova NanoSEM 450, FEI Q200 and Q600 3D microscopes (Czech Republic) equipped with backscattered electron detector (BSED) at accelerating voltage of 20—30 kV. Identification of geometrical patterns of structural areas of welded joints, data processing of phase and microtextural analyses were carried out using ImageJ and TSL OIM Analysis 9 software (USA). EBSD analysis was carried out in backscattered electron diffraction including recording of grain misorientation map. A sample for EBSD analysis was fixed at test table using carbon adhesive No. 502. A sample inclined at the angle of 70° to horizontal was scanned with the step of 1—3 μm by electron beam with the accelerating voltage of 20—30 kV.

Results and discussion

Description of initial material

The initial structure after multiaxial deformation of workpieces from the VTI-4 alloy is illustrated in Fig. 4. The microstructural studies in the transversal cross section of a sample processed by multiaxial forging revealed the homogeneous structure comprised of globular particles of α_2-phase with the diameter of 2—5 μm, laminar O-phase and fine grain β-matrix. The coarse primary grains of β-phase extended in the direction of final deformation are observed (see Fig. 4, *b*). They are fragmented into finer subgrains with the size of 15±2 μm (see Fig. 4, *a*). Along the boundaries of the latter, the globular particles of α_2-phase are located uniformly distributed over the volume. The plates of O-phase are present inside the subgrains of β-phase (see Fig. 4, *b*).

Visual Dimensional Inspection of Welded Joints

The external appearance of welded joint produced in various PLW modes is illustrated in Fig. 5. Using modes *1*, *2* and *4*, *5* (U = 280÷300 V, τ = 3÷6 ms), the WJ of a silver color were formed without significant convexities and shrinkage craters. Visually the welded points are of uniform round shape with fine flakiness (0.22±0.02 mm), the seam width: ~1.1 mm at pulse duration of 3 ms (see Fig. 5, *a—c*) and ~1.5 mm at 6 ms, respectively (see Fig. 5, *d—f*). However, upon a voltage increase to 320 V, on the WJ surface overlaps were detected as well as heterogene-

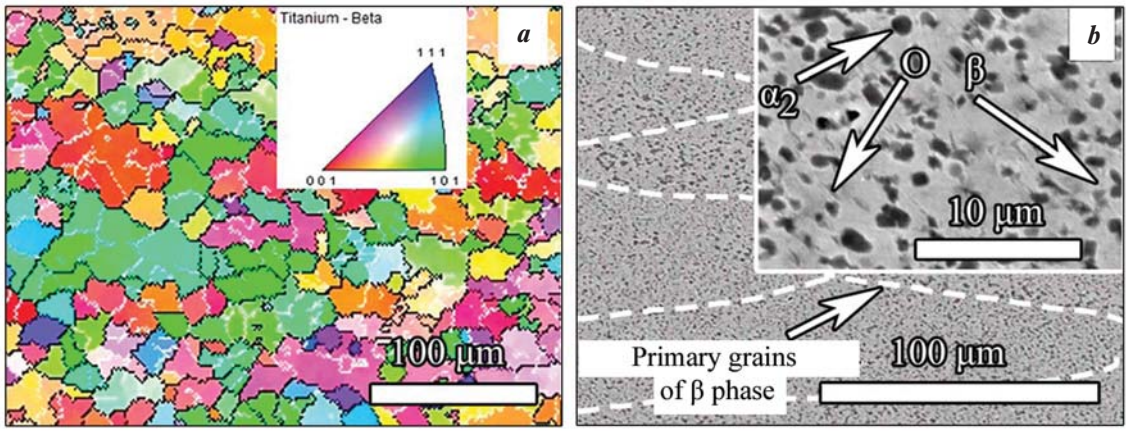

Fig. 4. Microstructure of forged workpiece from the VTI-4 alloy before pulsed laser beam welding

a – inverse pole figure map; ***b*** – BSE-SEM images of the microstructure after multiaxial deformation (the last deformation during multiaxial forging was vertical)

Рис. 4. Микроструктура кованой заготовки из сплава ВТИ-4 до проведения ИЛС

a – карта распределения ориентировок; ***b*** – снимки BSE-SEM микроструктуры после мультиосевой деформации (последняя деформация при мультиосевой ковке проходила вертикально)

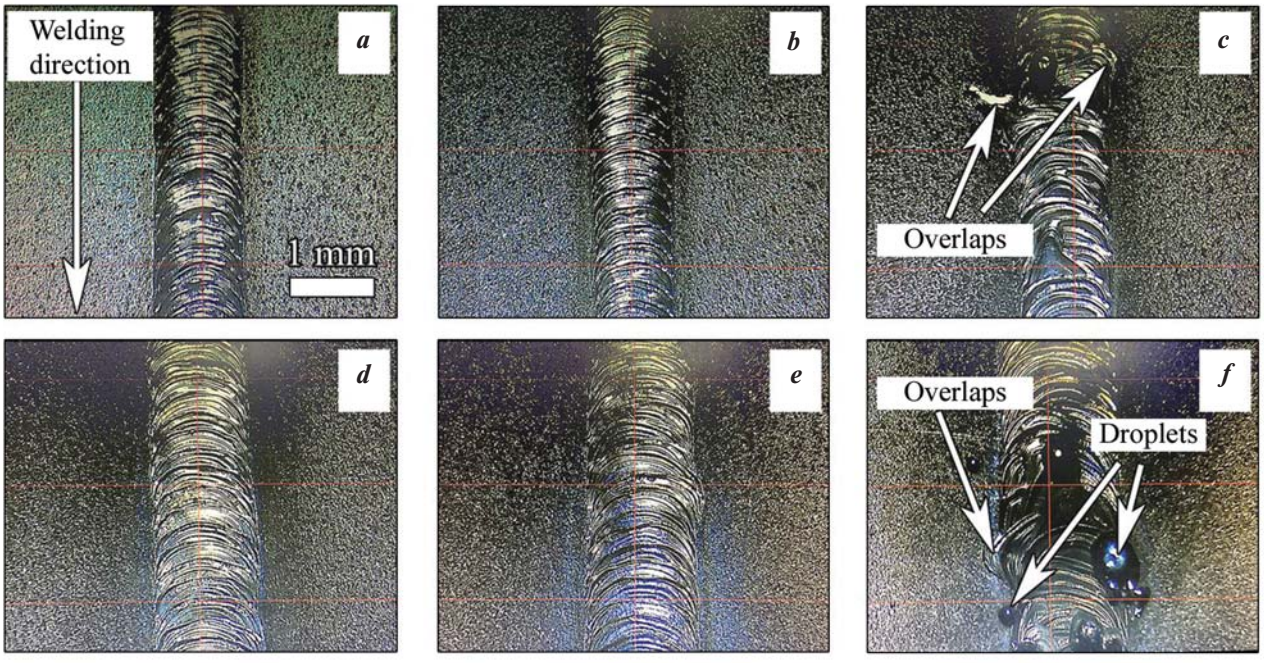

Fig. 5. Appearance of the welded joint from the VTI-4 alloy depending on the modes of laser welding, voltage and duration of the laser radiation pulse

a – mode *1*, ***b*** –*2*, ***c*** –*3*, ***d*** –*4*, ***e*** –*5*, ***f*** –*6*

Рис. 5. Внешний вид сварного соединения из сплава ВТИ-4 в зависимости от режимов ИЛС, напряжения и длительности импульса лазерного излучения

a – режим *1*, ***b*** – *2*, ***c*** –*3*, ***d*** – *4*, ***e*** – *5*, ***f*** – *6*

ous flakiness at τ = 3 ms (Fig. 5, *c*) and splashing at τ = 6 ms (Fig. 5, *f*).

High peak power and an increase in average pulse power lead to violation of thermal hydraulic processes of keyhole formation, promoting formation of coarse pores [22, 28], thus impairing the quality of welded joint. In addition, the energy density increases with pulse peak energy, and as is known, the higher the en-

ergy density, the more intensive is the collapse of bubbles, hence, the probability of formation of coarse pores increases [20].

Studying microstructure of welded joint

Transversal structure of welded joints produced in various PLW modes according to BSE-SEM and EBSD analyses is illustrated in Figs. 6 and 7. The transversal WJ was exposed from above to the impact of laser beam in pulsed mode with laser focusing on the surface of welded samples (focal distance is zero). The WJ shape is knife-like, characterized by the penetration depth and width (Fig. 8). The welded joint in the mode of knife fusion penetration is formed due to material evaporation and plasma formation on the surface. High temperatures on the surface and vapor pressure lead to expansion of the top part of WJ in comparison with its bottom part, thus forming a mushroom shape of the seam [29]. Fine internal pores with the diameter of 20—35 μm were detected. They are located mainly in the root and center of WJ (Fig. 6, *a*—*e*). First of all, occurrence of the pores is related with chemical activity of titanium alloys with respect to gases, which leads to formation of pores and

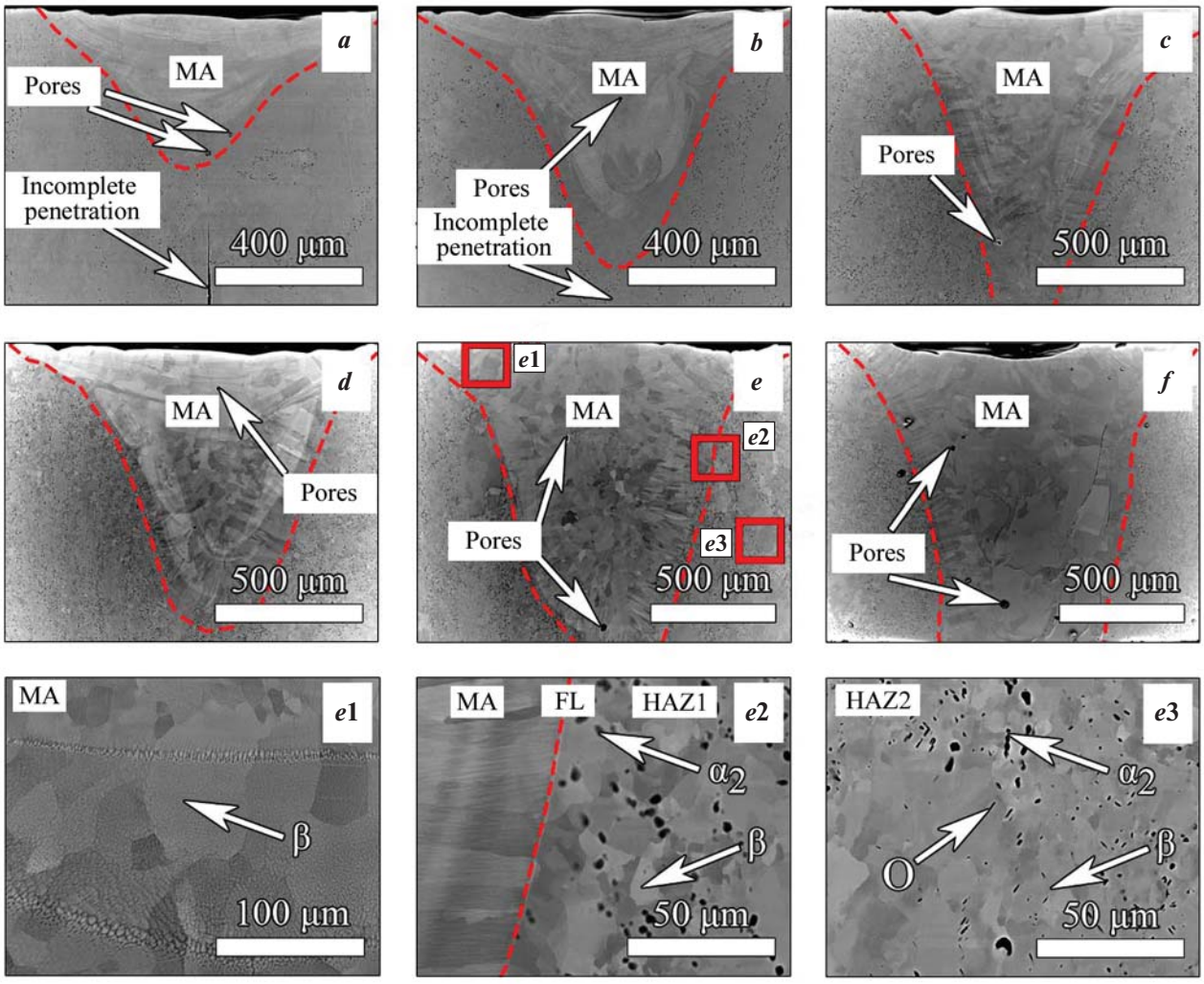

Fig. 6. Comparative analysis of microstructure of the welded joint from the VTI-4 alloy depending on the modes of pulsed laser beam welding

a – mode *1*, ***b*** –*2*, ***c*** –*3*, ***d*** –*4*, ***e*** –*5*, ***f*** –*6*
***e*1** – melting zone; ***e*2** – fusion line and first heat-affected zone; ***e*3** – second heat-affected zone

Рис. 6. Сравнительный анализ микроструктуры сварного соединения из сплава ВТИ-4 в зависимости от режимов ИЛС

a – режим *1*, ***b*** – *2*, ***c*** – *3*, ***d*** – *4*, ***e*** – *5*, ***f*** – *6*
***e*1** – зона плавления; ***e*2** – линия сплавления и первая зона термического влияния; ***e*3** – вторая зона термического влияния

cracks during welding [30]. Keyhole oscillations can cause more intensive formation of bubbles and their collapse will lead to formation of coarse pores and pores which do not have time to float remaining in the WJ central part [20].

When mode *6* is used (U = 320 V, τ = 6 ms), the number of transversal pores with a diameter of 40 ± ± 5 μm increases (Fig. 6, *f*). In addition, incomplete penetrations were detected in the seam root characteristic for modes with fusion depth of less than 1.5 mm (Fig. 6, *a*, *b*, *d*).

Figure *6* also illustrates that the welded joint has the melting area (MA) (Fig. 6, *e*1), the heat affected zone (HAZ), separated by the fusion line (FL), and the area of the base metal (BM) (Fig. 6, *e*2, e3).

It was established that the MA is comprised of β-phase, at the MA—FL interface the grains of β-phase have a more elongated shape, and with an increase in the average power of laser beam up to ~80 W their length increases from ~120 to ~190 μm (Fig. 7, *a—f*). With a further increase in the average power (mode *6*) the size of elongated grains of β-phase decreases to ~170 μm. This is attributed to better heat removal upon formation of opposite beam of the WJ root (Fig. 7, *f*). At the MA—FL interface α_2- and O-phases were completely dissolved upon heating and no back transformation took place upon cooling. At the boundary of the fusion line and HAZ1, there are no coarse globular grains of β-phase (Fig. 6, *e*2). Presumably, this is attributed to high temperature gradients stipulated by the PLW processes, when local impact of each pulse is accompanied by rapid cooling [31].

In turn, the area of thermal impact in terns of revealed structural constituents can be subdivided into HAZ1, comprised of β + α_2 phases (Fig. 6, *e*2), and HAZ2, structurally comprised of β + α_2 + O phases (Fig. 6, *e*3). In the HAZ1 area, the globular α_2-phase was partially retained, since for completion of $\alpha_2 \rightarrow \beta$ transformation higher temperatures are required [32]. Contrary to the base metal, in HAZ2 the O phase upon heating is partially transformed into β phase, whereas the α_2-phase is actually retained. Transition from HAZ1 to HAZ2 is gradual and accompanied by an increase in the fraction of the α_2-phase. During transition from HAZ2 to BM the fraction of the O-phase increases.

In center of the IPF EBSD maps cast, the structure of MA welded joint is observed. It is comprised mainly of elongated dendrites of β-phase, and in the FL region and in the central part of MA — of globular grains of β-phase

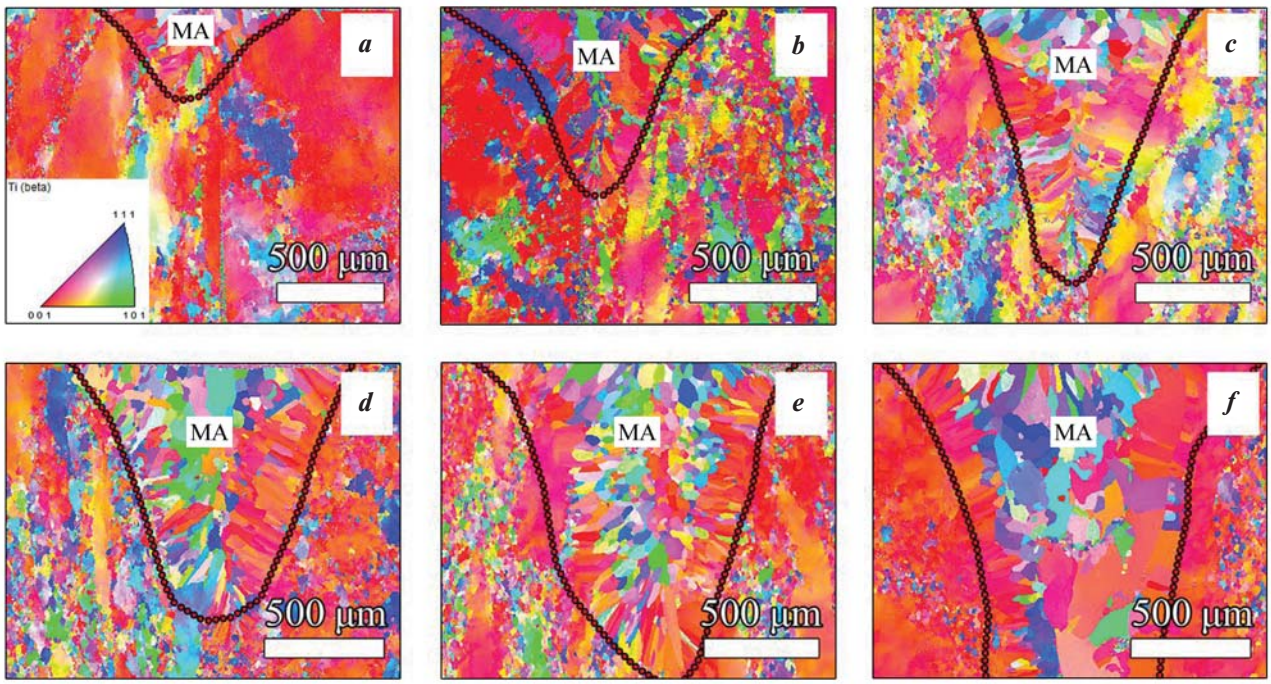

Fig. 7. EBSD analysis of welded joints from the VTI-4 alloy depending on PLW modes
a – mode *1*, ***b*** –*2*, ***c*** –*3*, ***d*** –*4*, ***e*** –*5*, ***f*** –*6*

Рис. 7. EBSD-анализ сварных соединений из сплава ВТИ-4 в зависимости от режимов ИЛС
a – режим *1*, ***b*** – *2*, ***c*** – *3*, ***d*** – *4*, ***e*** – *5*, ***f*** – *6*

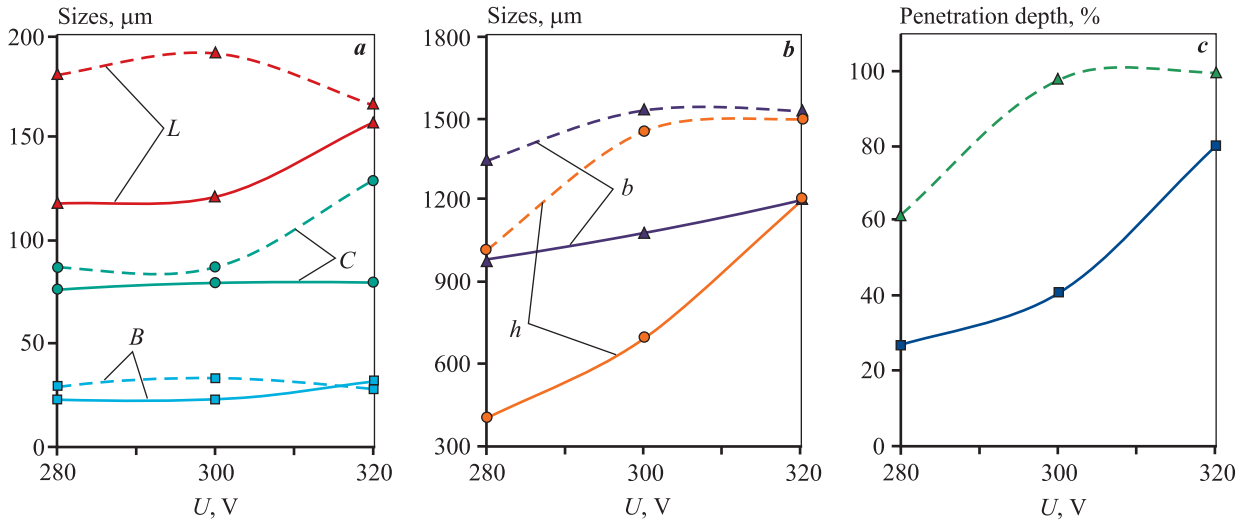

Fig. 8. Parameters of microstructure of welded joints from the VTI-4 alloy (***a***), their geometrical parameters (***b***) and penetration depth (***c***) depending on the PLW modes

τ = 3 ms (solid lines), τ = 6 ms (dashed lines)
a: *L* – length, *B* – width of dendrites at FL boundary, *C* – grain size
b: *h* – depth, *b* – width of the weld

Рис. 8. Параметры микроструктуры сварных швов из сплава ВТИ-4 (***a***), их геометрические параметры (***b***) и глубина проплавления (***c***) в зависимости от режимов ИЛС

τ = 3 мс (сплошные линии), τ = 6 мс (штриховые)
a: *L* – длина, *B* – ширина дендритов на границе ЛС, *C* – размер зерен
b: *h* – глубина, *b* – ширина сварного шва

(Fig. 7). The length of dendrites and the penetration depth increase from 119±20 to 192±15 μm with an increase in the laser power from 40 to 80 W. The width of elongated dendrites nearly does not change and retains in the range of 23—35 μm (Fig. 8, *a*). In welding mode *6* (U = 320 V, τ = 6 ms), the welding bath is deflected, the length of dendrites decreases to 167±15 μm, and their width in the central region of MA increases to 130±10 μm.

The peak power of laser beam influences not only on the penetration depth (Fig. 8, *a*), but also on the external shape of the seam. Usually in the case of repetitively pulsed lasers, the energy density reaches $E = 10^5 \div 10^7$ W/cm^2 at the pulse duration of $<10^{-3}$ s. At the peak power higher than 2.7 kW (Fig. 8, *b*) the energy density increases to $>10^7$, leading to violations in WJ formation, namely: splashing of liquid metal and overlaps (Fig. 5, *c*, *f*).

The width of welded joint at equal focal distance of laser depends on the duration of laser pulse impact: on average at τ = 3 ms it equals to 1.05±0.1 mm, at τ = 6 ms to 1.45±0.1 mm (Fig. 8, *b*). The penetration depth mostly depends on the laser energy density, at its peak power of 2.1 kW (Fig. 8, *c*) the penetration is 27 % of the thickness of welded plates; in welding mode *3* (U = 320 V, τ = 3 ms with the peak power of 3.2 kW) — 80 %. At a pulse duration of 6 ms and the voltage of 300 V and higher the complete penetration depth of plates from the VTI-4 alloy with the thickness of 1.5 mm is achieved (Fig. 8, *c*).

Studying mechanical properties of welded joints

The plots of microhardness and mechanical properties upon uniaxial tension of welded joints are illustrated in Figs. 9 and 10. The microhardness of transversal welded joints is about 340±20 $HV_{0.2}$, and that of base metal about 345±10 $HV_{0.2}$. In the HAZ region, the microhardness decreases to 330±5 $HV_{0.2}$. Generally, for Ti_2AlNb-based alloys, the dispersion strengthening of O-phase is the main mechanism of strengthening. Therefore, due to the absence of O-phase in the region of HAZ1 and MA, the microhardness is the lowest. While the extent of conversion of O-phase into B2-phase decreases from the welding area to HAZ2, the hardness profile demonstrates a trend towards an increase to the base metal [33, 34].

The variation of microhardness profiles in the HAZ1–2 region in comparison with BM and MA is related to changes in volumetric fraction and si-

zes of equiaxial phase α_2, which is mainly distributed along the boundaries of primary grains of β phase [35]. With an increase in the average laser power, the size of equiaxial α_2-phase (α_2 = 3.1±2.0 μm in BM) in HAZ nearly does not change from the average size of 2.8±2.0 μm (in welding mode *1*) to 2.5±2.0 μm (in welding mode *6*). The phase composition of α_2 in HAZ does not differ significantly from BM (~3 %

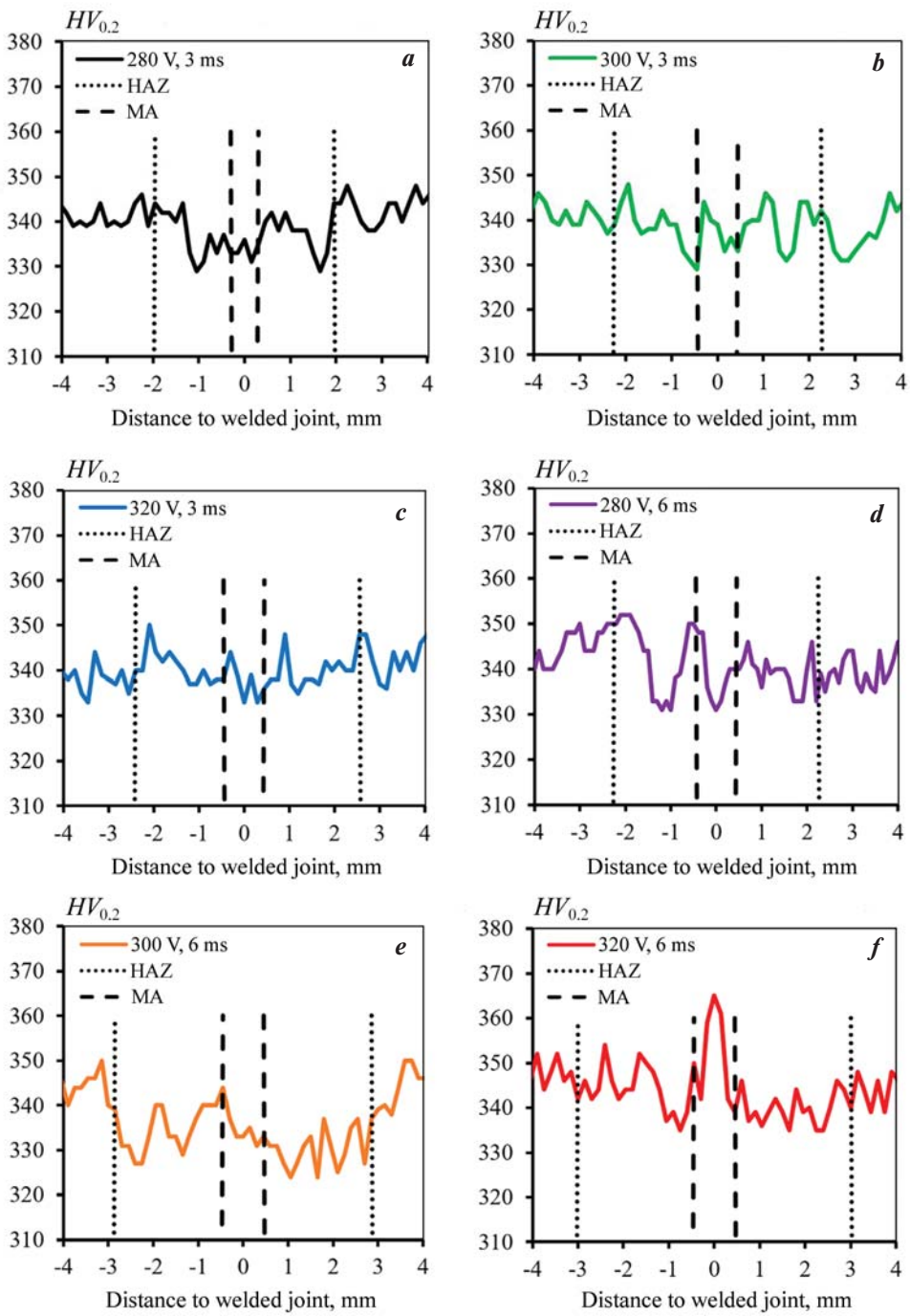

Fig. 9. Distribution of microhardness in the cross-section of welded joints from the VTI-4 alloy depending on PLW modes

a – mode *1*, ***b*** –*2*, ***c*** –*3*, ***d*** –*4*, ***e*** –*5*, ***f*** –*6*

Рис. 9. Распределение микротвердости в поперечном сечении сварных швов из сплава ВТИ-4 в зависимости от режимов ИЛС

a – режим *1*, ***b*** – *2*, ***c*** – *3*, ***d*** – *4*, ***e*** – *5*, ***f*** – *6*

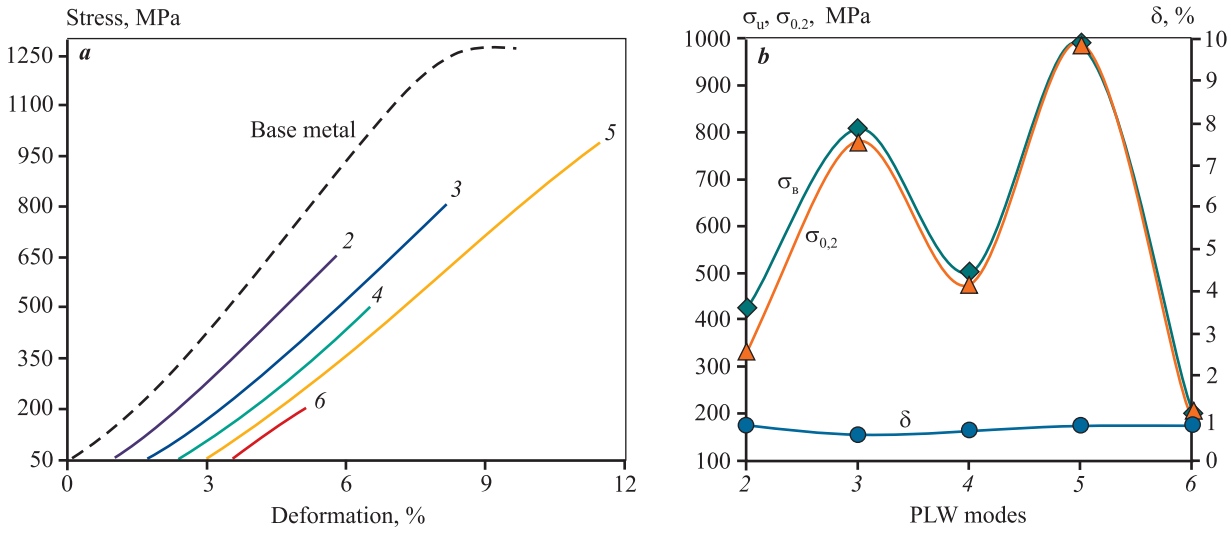

Fig. 10. Tensile diagram (***a***) and mechanical properties (***b***) of welded joints from the VTI-4 alloy depending on PLW modes (numbers near curves)

Рис. 10. Диаграмма растяжения (***a***) и механические свойства (***b***) сварных соединений из сплава ВТИ-4 в зависимости от режимов ИЛС (цифры у кривых)

α_2 phase), since in PLW modes *1—3* and *5* the fraction of α_2 in HAZ does not exceed 2.5 %, and in modes *4* and *6* — 3÷5 %.

Therefore, minor changes in the sizes, phase composition, and distribution of α_2-phase along the boundaries of primary grains of β-phase lead to variations in microhardness profiles transversal to WJ in various sites. Upon welding in mode *6* (U = 320 V, τ = 6 ms) in the MA region, a microhardness peak of 365 $HV_{0.2}$ can be observed. This is related to partial saturation with oxygen [36]. In this case gas was supplied along the laser impact on the surface of welded plates which does not eliminate completely the bath contact with ambient air from the side of seam root.

Mechanical properties of initial VTI-4 alloy are as follows: σ_u = 1250 MPa, $\sigma_{0.2}$ = 1200 MPa, δ = 2.07 %. The strength properties of welded joint are about 80 % of the strength of base metal are achieved at welding mode *5* (U = 300 V, τ = 6 ms). Further increase in the voltage up to 320 V leads to violation of PLW process and the occurrence of external defects, exerting a negative influence on the strength properties. With a decrease in the voltage to 280 V complete penetration (<70 % of the plate thickness) of welded joint is not achieved, and the strength is ~40 % of that of the base metal. The joint is not welded for full depth acts as the stress concentrator, thus impairing the strength properties.

The plasticity of welded joints in all cases decreases (Fig. 10, *b*), since the PLW as well as other method of fusion welding is accompanied by formation of coarse columnar B2 structure [13]. Plasticity can be increased by means of subsequent thermal treatment of welded joints [32].

Studying porosity in welded joint

Fractures after tensile tests are illustrated in Fig. 11. The sample thickness in Fig. 11, *a* was decreased due to localized heating on plate surface and its intensive deformation, as a consequence a portion of metal was removed as in Fig. 11, *e*, due to heterogeneity of welded joint, undercutting and metal splashing.

The fracture of welded joint in all cases is in the MA region closer to the FL boundary. On the fracture surface, a river relief is observed. On the fracture surface, the highest number of gaseous pores occurs (Fig. 11, *a—d*) and extended secondary cracks (Fig. 11, *a*1, *e*1) appear. Such microcracks are nucleated and propagated along the grain boundaries of β-phase due to the absence of deformation inside the grains. The fractures observed in this work are characteristic of the welded joints with the structure of β-phase, where during breaking the crack in the foundation of river line is split [13, 37].

The size and distribution of pores decrease with an increase in the laser power. At low heat input the coarse pores are concentrated on seam root. This is attributed to the violation of keyhole. With an increase in the energy the pore size decreases, the pores are distributed over

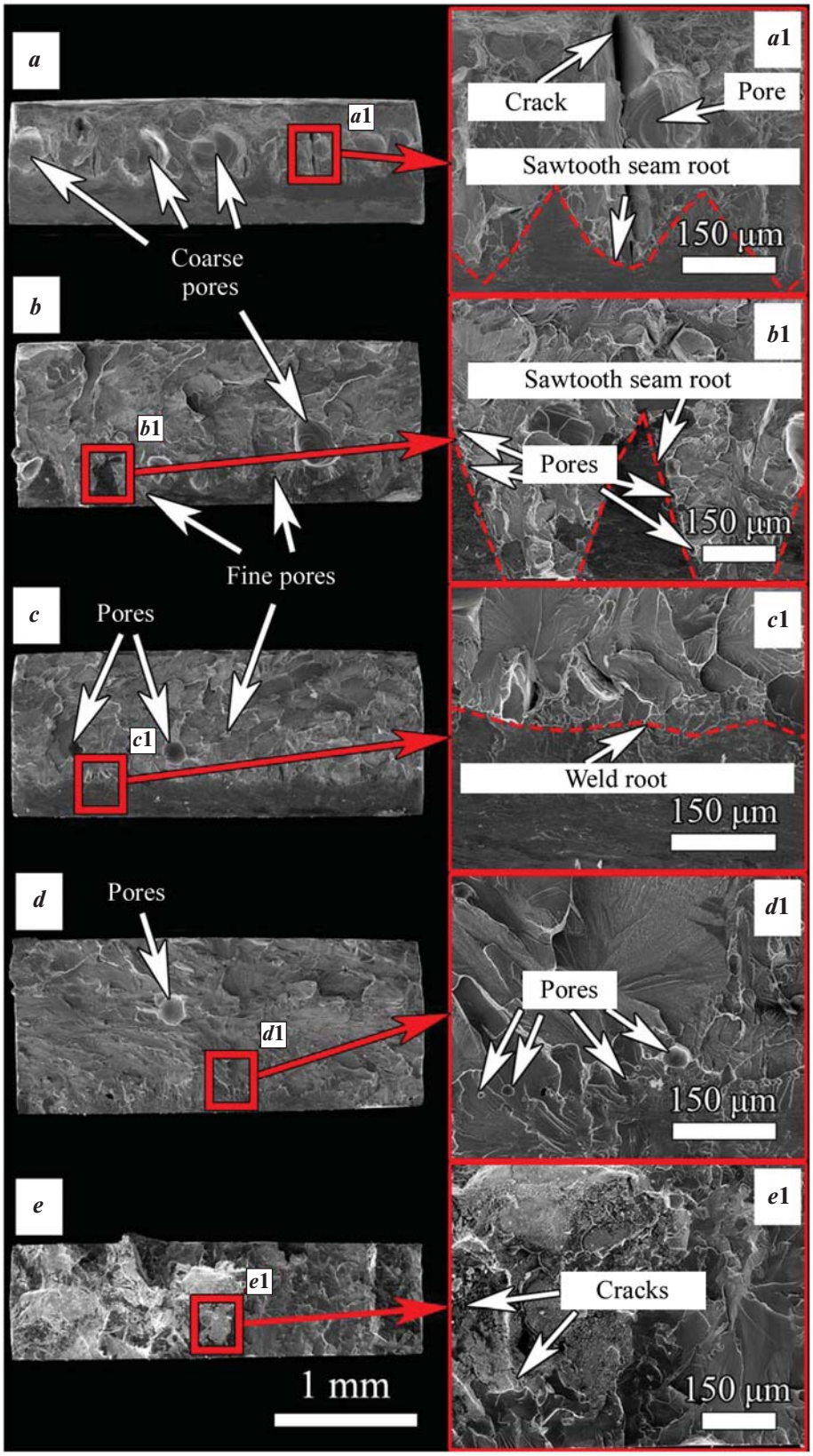

Fig. 11. Morphology of fracture surface of tensile specimens depending on PLW modes
a – mode *1*, ***b*** –*2*, ***c*** –*3*, ***d*** –*4*, ***e*** –*5*, ***f*** –*6* (impact of laser pulsed radiation from above)

Рис. 11. Морфологии поверхности излома образцов на растяжение в зависимости от режимов ИЛС
a – режим *1*, ***b*** – *2*, ***c*** – *3*, ***d*** – *4*, ***e*** – *5*, ***f*** – *6* (действие импульсного лазерного излучения сверху)

the entire volume providing more favorable conditions for floating of gas bubbles.

At the fracture of samples welded in mode *3* (U = = 320 V, τ = 3 ms), a sawtooth WJ root was detected, providing for complete penetration in some places (Fig. 11, *b*). Coarse pores are distributed non-uniformly over the fracture. In the WJ root and center, the high values of peak laser power with regard to its average exerts a negative impact on formation of keyhole. This leads to formation of coarse (Fig. 11, *b*) and fine (Fig. 11, *b*1) pores in the seam cross section [27].

Therefore, it can be seen (Fig. 11, *a*, *b*) that in the transversal cross section of a welded joint under the impact of short pulse and high voltages, the sawtooth seam root is more pronounced with the formation of coarser spherical pores with the sizes of 150—200 μm (modes *2* and *3*). With a twofold increase in the duration of the laser radiation pulse the sawtooth seam root is less pronounced (Fig. 11, *c*), and finer pores are formed: up to ~100 μm (mode *4*). Due to the stabilization of keyhole in mode *5* (U = 300 V, τ = 6 ms), maximum pore content is achieved using optimized welding parameters [38]. However, in mode *5*, fine spherical pores with the sizes of 10—30 μm are concentrated in the bottom part of the welded joint, which can be attributed to local incomplete penetration (Fig. 11, *d*1). The rare occurrence of single spherical pores with the size up to ~100 μm in the central part of transversal cross section of welded joint can be attributed to local incomplete penetration (Fig. 11, *d*).

Porosity decreases the effective surface area of welded joint cross section, makes it loose, decreases plasticity, and also acts as a stress concentrator [24]. This can be attributed to crack nucleation and its propagation to the WJ root in the welding mode *2* (U = = 300 V, τ = 3 ms) (Fig. 11, *a*1). Existence of coarse pores in welded joint cross section in modes *2* (~11.5 %) and 3 (~3.8 %) increases the volume of their total fraction in respect of fracture cross section (Fig. 11, *a*, *b*). With an increase in laser power and pulse duration, the fraction of pores in the transversal cross section decreases, equaling for mode *4* (U = 280 V, τ = 6 ms) to <2 % (average power: 60.8 W), and for the rest not higher than 1 %.

Conclusions

Due to the preliminary preparation of the structural state of material after multiaxial abc forging of a workpiece with heating up to 970 °C at the rate of <0.1 mm/s and deformation degree of 50 % in each case, as well as the use of optimum pulsed mode of laser welding, a faultless high quality welded joint was obtained from the Ti_2AlNb-based VTI-4 alloy with the strength properties at the level of ~80 % of the base metal.

In the case of the LAT-S-300 laser facility the optimum PLW conditions for sheet material from the VTI-4 alloy with the thickness of 1.5 mm, where the volumetric portion of pores does not exceed 1 % of the cross section of the welded joint, are as follows:

— pulse voltage: 300 V;
— pulse duration: 6 ms;
— step between pulses: 0.25 mm;
— flow rate of protecting gas: 2.5 bar;
— focal distance on the surface of workpieces is zero;
— welding speed: 0.3 m/min.

It was established that the melting area of the welded joint during PLW is comprised of β-phase, while α_2- and O-phases were completely dissolved upon heating. Due to the high temperature gradients stipulated by PLW processes, the heat affected zone is comprised of the of $\beta + \alpha_2$ and $\beta + \alpha_2 + O$ regions.

It was demonstrated that the reasons for the porosity of the welded joint upon PLW of the VTI-4 alloy are as follows:

— violations of thermal hydraulic processes;
— formation of sawtooth seam root with incomplete penetration;
— no protecting gas backing from the side of seam root;
— splashing of liquid metal;
— overlaps on seam surface;
— non-uniformity of pulse application.

All these factors lead to additional cracking, heterogeneity of the melting area and, as a consequence, to poorer mechanical properties.

References

1. Banerjee D., Gogia A.K., Nandi T.K., Joshi V.A. A new ordered orthorhombic phase in a Ti_3AlNb alloy. *Acta Metallurgica*. 1988;36(4):871—882. https://doi.org/10.1016/0001-6160(88)90141-1
2. Banerjee D. The intermetallic Ti_2AlNb. *Progress in Materials Science*. 1997;42(1-4):135—158. https://doi.org/10.1016/S0079-6425(97)00012-1
3. Wang L., Sun D., Li H., Gu X., Shen C. Microstructures and mechanical properties of a laser-welded joint of Ti_3Al—Nb alloy using pure Nb filler metal. *Metals (Basel)*. 2018;8(10):785. https://doi.org/10.3390/met8100785
4. Shagiev M.R., Galeyev R.M., Valiakhmetov O.R. Ti_2AlNb-Based intermetallic alloys and composites. *Materials physics and mechanics*. 2017;33(1):12—18. https://doi.org/10.18720/MPM.3312017_2

5. Pollock T.M., Tin S. Nickel-based superalloys for advanced turbine engines: Chemistry, microstructure, and properties. *Journal of Propulsion and Power*. 2006;22(2):361—374. https://doi.org/10.2514/1.18239
6. Liu X., Wu S., Ji Y., Shao L., Zhao H., Wan X. Ultrasonic frequency pulse tungsten inert gas welding of Ti_2AlNb-based alloy. *Xiyou Jinshu/Chinese Journal of Rare Metals*. 2014;38(4):541—547. https://doi.org/10.13373/j.cnki.cjrm.2014.04.001
7. Lu B., Yin J., Wang Y., Yang R. Gas tungsten arc welding of Ti_2AlNb based alloy sheet. In: *Proc. 12th World Conf. Titan (Ti 2011)*. (China, Beijing, 19—24 June 2011). 2012. Vol. 1. P. 816—818.
8. Shao L., Cui E. Joining of Ti—22Al—25Nb Alloy using different welding methods. *Materials China*. 2019;38(3):286—290. https://doi.org/10.7502/j.issn.1674-3962.2019.03.11
9. Mohandas T., Banerjee D., Mahajan Y.R., Kutumba Rao V.V. Studies on fusion zone fracture behaviour of electron beam welds of an α + β-titanium alloy. *Journal of Materials Science*. 1996;31(14):3769—3775. https://doi.org/10.1007/BF00352792
10. Li D., Hu S., Shen J., Zhang H., Bu X. Microstructure and mechanical properties of laser-welded joints of Ti—22Al—25Nb/TA15 dissimilar titanium alloys. *Journal of Materials Engineering and Performance*. 2016;25(5):1880—1888. https://doi.org/10.1007/s11665-016-2025-4
11. Li Y.-J., Wu Ai-P., Li Q., Zhao Y., Zhu R.-C., Wang G.-Q. Effects of welding parameters on weld shape and residual stresses in electron beam welded Ti_2AlNb alloy joints. *Transactions of Nonferrous Metals Society of China*. 2019;29(1):67—76. https://doi.org/10.1016/S1003-6326(18)64916-7
12. Skupov A.A., Sviridov A.V., Khodakova E.A., Afanasev-Khodykin A.N. Creation of joints from intermetallic titanium alloys (review). *Trudy VIAM*. 2021;7:31—38. (In Russ.).
Скупов А.А., Свиридов А.В., Ходакова Е.А., Афанасьев-Ходыкин А.Н. Создание неразъемных соединений из интерметаллидных титановых сплавов (обзор). *Труды ВИАМ*. 2021;7:31—38. https://doi.org/10.18577/2307-6046-2021-0-7-31-38
13. Zhang K., Lei Z., Chen Y., Yang K., Bao Y. Heat treatment of laser-additive welded Ti_2AlNb joints: Microstructure and tensile properties. *Materials Science and Engineering: A*. 2019;744:436—444. https://doi.org/10.1016/j.msea.2018.12.058
14. Auwal S.T., Ramesh S., Yusof F., Manladan S.M. A review on laser beam welding of titanium alloys. International *Journal of Advanced Manufacturing Technology*. 2018;97(1-4):1071—1098. https://doi.org/10.1007/s00170-018-2030-x
15. Chludzinski M., dos Santos R.E., Churiaque C., Ortega-Iguña M., Sánchez-Amaya J.M. Pulsed laser welding applied to metallic Materials — A Material Approach. *Metals*. 2021;21(4):640. https://doi.org/10.3390/met11040640
16. Zhang P., Jia Z., Yu Z., Shi H., Li S., Wu D., Yan H., Ye X., Chen J., Wang F., Tian Y. A review on the effect of laser pulse shaping on the microstructure and hot cracking behavior in the welding of alloys. *Optics & Laser Technology*. 2021;140:107094. https://doi.org/10.1016/j.optlastec.2021.107094
17. Gaikwad A., Deore H., Kotwal V., Pawar A., Valli A. Review on laser welding of titanium alloy. In: *Proc. International Conference on Ideas, Impact and Innovation in Mechanical Engineering (ICIIIME 2017)* (India, Rajasthan, 1—2 June 2017). 2017. Vol. 5(6). P. 789—795.
18. Li Y.-J., Wu A.-P., Li Q., Zhao Y., Zhu R.-C., Wang G.-Q. Mechanism of reheat cracking in electron beam welded Ti_2AlNb alloys. *Transactions of Nonferrous Metals Society of China*. 2019;29(9):1873—1881. https://doi.org/10.1016/S1003-6326(19)65095-8
19. Panov D.O., Naumov S.V., Sokolovsky V.S., Volokitina E.I., Kashaev N., Ventzke V., DInse R., Riekehr S., Povolyaeva E.A., Alekseev E.B., Nochovnaya N.A., Zherebtsov S.V., Salishchev G.A. Cracking of Ti_2AlNb-based alloy after laser beam welding. *IOP Conference Series: Materials Science and Engineering*. 2021;1014:012035. https://doi.org/10.1088/1757-899X/1014/1/012035
20. Xu J., Rong Y., Huang Y., Wang P., Wang C. Keyhole-induced porosity formation during laser welding. *Journal of Materials Processing Technology*. 2018;252:720—727. https://doi.org/10.1016/j.jmatprotec.2017.10.038
21. Zhou J., Tsai H.L. Porosity formation and prevention in pulsed laser welding. *ASME Journal of Heat and Mass Transfer*. 2007;129(8):1014—1024. https://doi.org/10.1115/1.2724846
22. Bruyere V., Touvrey C., Namy P. A phase field approach to model laser power control in spot laser welding. In: *Proc. 2014 COMSOL Conf. 2014*. P. 1—4. URL: https://www.comsol.com/paper/a-phase-field-approach-to-model-laser-power-control-in-spot-laser-welding-18505 (accessed: 01.09.2022).
23. Li H. Analysis of porosity in welding of titanium alloy. In: *Proc. 2020 3rd International Conference on Electron Device and Mechanical Engineering (ICEDME)* (China, Suzhou, 1—3 May 2020). 2020. P. 486—489. https://doi.org/10.1109/ICEDME50972.2020.00116
24. Li H. The causes and control of porosity in titanium alloy welding. In: *Proc. 2020 3rd International Conference on Electron Device and Mechanical Engineering (ICEDME)* (China, Suzhou, 1—3 May 2020). 2020. P. 490—493. https://doi.org/10.1109/ICEDME50972.2020.00117

25. Huang J.L., Warnken N., Gebelin J.-C., Strangwood M., Reed R.C. On the mechanism of porosity formation during welding of titanium alloys. *Acta Materialia*. 2012;60(6-7):3215—3225. https://doi.org/10.1016/j.actamat.2012.02.035
26. Chen W., Li J.W., Xu L., Lu B. Development of Ti_2AlNb alloys: Opportunities and challenges. *Advanced Materials and Processes*. 2014;172(5):23—27.
27. Zhan X., Yan T., Gao Q., Zhu Z., Bu H., Wang Z. The porosity formation mechanism in the laser welded joint of TA15 titanium alloy. *Materials Research Express*. 2019;6(7):076558. https://doi.org/10.1088/2053-1591/ab1612
28. Torkamany M.J., Malek Ghaini F., Papan E., Dadras S. Process optimization in titanium welding with pulsed Nd:YAG laser. *Science of Advanced Materials*. 2012;4(3-4): 489—496. https://doi.org/10.1166/sam.2012.1307
29. Baranov D.A., Parkin A.A., Zhatkin S.S. Features of formation of the welded seam of heat-resistant KhN45VMTYuBR alloy depending on the modes of laser welding. *Izvestiya Samarskogo nauchnogo tsentra RAN*. 2018;2:170—176. (In Russ.).
Баранов Д.А., Паркин А.А., Жаткин С.С. Особенности формирования сварного шва жаропрочного сплава ХН45ВМТЮБР в зависимости от режимов лазерной сварки. *Известия Самарского научного центра РАН*. 2018;2:170—176.
30. Grigoryants A.G., Shiganov I.N., Misyurov A.I. Technological processes of laser processing. Moscow: MGTU imeni. N.E. Baumana. 2008. 664 p. (In Russ.).
Григорьянц А.Г., Шиганов И.Н., Мисюров А.И. Технологические процессы лазерной обработки. Москва: МГТУ им. Н.Э. Баумана, 2008. 664 с.
31. Baeslack W.A., Cieslak M.J., Headley T.J. Structure, properties and fracture of pulsed Nd:YAG laser welded Ti—14.8wt%Al—21.3wt%Nb titanium aluminide. *Scripta Metallurgica*. 1988;22(7):1155—1160. https://doi.org/10.1016/S0036-9748(88)80122-4
32. Panov D., Naumov S., Stepanov N., Sokolovsky V., Volokitina E., Kashaev N., Ventzke V., Dinse R., Riekehr S., Povolyaeva E., Nochovnaya N., Alekseev E., Zherebtsov S., Salishchev G. Effect of pre-heating and post-weld heat treatment on structure and mechanical properties of laser beam-welded Ti_2AlNb-based joints. *Intermetallics*. 2022;143:107466. https://doi.org/10.1016/j.intermet.2022.107466
33. Chen X., Xie F. Q., Ma T. J., Li W. Y., Wu X. Q. Effects of post-weld heat treatment on microstructure and mechanical properties of linear friction welded Ti_2AlNb alloy. *Materials & Design*. 2016;94:45—53. https://doi.org/10.1016/j.matdes.2016.01.017
34. Xiong L., Mi G., Wang C. Microstructure and mechanical properties of laser-welded joints of Ti—22Al-25Nb/Ti—6Al—4V dissimilar titanium alloys. *Journal of Laser Applications*. 2018;30(3):032412. https://doi.org/10.2351/1.5040610
35. Chen W., Chen Z.Y., Wu C.C., Li J.W., Tang Z.Y., Wang Q.J. The effect of annealing on microstructure and tensile properties of Ti—22Al—25Nb electron beam weld joint. *Intermetallics*. 2016;75:8—14. https://doi.org/10.1016/j.intermet.2016.02.006
36. Mehdi B., Badji R., Ji V., Allili B., Bradai D., Deschaux-Beaume F., Soulié F. Microstructure and residual stresses in Ti—6Al—4V alloy pulsed and unpulsed TIG welds. *Journal of Materials Processing Technology*. 2016;231:441—448. https://doi.org/10.1016/j.jmatprotec.2016.01.018
37. Wu J., Xu L., Lu Z., Cui Y., Yang R. Preparation of powder metallurgy Ti—22Al—24Nb—0.5Mo alloys and electron beam welding. *Jinshu Xuebao/ Acta Metallurgica Sinica*. 2016;52:1070—1078. https://doi.org/10.11900/0412.1961.2016.00019
38. Huang J., Turner R., Gebelin J.C., Warnken N., Strangwood M., Reed R.C. The effect of hydrogen on porosity formation during electron beam welding of titanium alloys. In: *ASM Proc International Conference on Trends in Welding Rearch* (USA, Chicago, 4—8 June 2012). 2013. P. 868—875.

Information about the authors

Stanislav V. Naumov – Cand. Sci. (Eng.), Assistant Professor of the Department of Materials Science and Nanotechnology (MSN); Senior Research Scientist of the Laboratory of Bulk Nanostructured Materials (BNM), Belgorod State University (BSU).
https://orcid.org/0000-0002-4084-8861
E-mail: NaumovStanislav@yandex.ru

Dmitrii O. Panov – Cand. Sci. (Eng.), Assistant Professor of the Department of MSN; Senior Research Scientist of the Laboratory of BNM, BSU.
https://orcid.org/0000-0002-8971-1268
E-mail: dimmak-panov@mail.ru

Ruslan S. Chernichenko – Engineer of the Laboratory of BNM, BSU.
https://orcid.org/0000-0002-8619-0700
E-mail: chernichenko@bsu.edu.ru

Vitaly S. Sokolovsky – Cand. Sci. (Eng.), Research Scientist of the Laboratory of BNM, BSU.
https://orcid.org/0000-0001-5607-2765
E-mail: sokolovskiy@bsu.edu.ru

Elena I. Volokitina – Engineer of the Laboratory of BNM, BSU.
https://orcid.org/0000-0001-9554-2651
E-mail: 1108668@bsu.edu.ru

Nikita D. Stepanov – Cand. Sci. (Eng.), Assistant Professor of the Department of MSN; Senior Research Scientist of the Laboratory of BNM, BSU.
https://orcid.org/0000-0003-2476-3953
E-mail: stepanov@bsu.edu.ru

Sergey V. Zherebtsov – Dr. Sci. (Eng.), Professor of the Department of MSN, Chief Research Scientist of the Laboratory of BNM, BSU.
https://orcid.org/0000-0002-1663-429X
E-mail: zherebtsov@bsu.edu.ru

Evgeny B. Alekseev – Cand. Sci. (Eng.), Head of Sector, All-Russia Institute of Aviation Materials «VIAM».
Scopus-ID 56581528500
E-mail: hiten_@mail.ru

Nadezhda A. Nochovnaya – Dr. Sci. (Eng.), Head of Laboratory, All-Russia Institute of Aviation Materials «VIAM».
E-mail: nochovnaya_viam@mail.ru

Gennady A. Salishchev – Dr. Sci. (Eng.), Professor of the Department of MSN, Head of the Laboratory of BNM, BSU.
https://orcid.org/0000-0002-0815-3525
E-mail: salishchev_g@bsu.edu.ru

Информация об авторах

Станислав Валентинович Наумов – к.т.н., доцент кафедры материаловедения и нанотехнологий (МиН), ст. науч. сотрудник лаборатории объемных наноструктурных материалов (ОНМ), Белгородский государственный национальный исследовательский университет (НИУ «БелГУ»).
https://orcid.org/0000-0002-4084-8861
E-mail: NaumovStanislav@yandex.ru

Дмитрий Олегович Панов – к.т.н., доцент кафедры МиН, ст. науч. сотрудник лаборатории ОНМ, НИУ «БелГУ».
https://orcid.org/0000-0002-8971-1268
E-mail: dimmak-panov@mail.ru

Руслан Сергеевич Черниченко – инженер лаборатории ОНМ, НИУ «БелГУ».
https://orcid.org/0000-0002-8619-0700
E-mail: chernichenko@bsu.edu.ru

Виталий Сергеевич Соколовский – к.т.н., науч. сотрудник лаборатории ОНМ, НИУ «БелГУ».
https://orcid.org/0000-0001-5607-2765
E-mail: sokolovskiy@bsu.edu.ru

Елена Ивановна Волокитина – инженер лаборатории ОНМ, НИУ «БелГУ».
https://orcid.org/0000-0001-9554-2651
E-mail: 1108668@bsu.edu.ru

Никита Дмитриевич Степанов – к.т.н., доцент кафедры МиН, ст. науч. сотрудник лаборатории ОНМ, НИУ «БелГУ».
https://orcid.org/0000-0003-2476-3953
E-mail: stepanov@bsu.edu.ru

Сергей Валерьевич Жеребцов – д.т.н., профессор кафедры МиН, гл. науч. сотрудник лаборатории ОНМ, НИУ «БелГУ».
https://orcid.org/0000-0002-1663-429X
E-mail: zherebtsov@bsu.edu.ru

Евгений Борисович Алексеев – к.т.н., начальник сектора, Всероссийский научно-исследовательский институт авиационных материалов (ВИАМ).
Scopus-ID: 56581528500
E-mail: hiten_@mail.ru

Надежда Алексеевна Ночовная – д.т.н., начальник лаборатории, ВИАМ.
E-mail: nochovnaya_viam@mail.ru

Геннадий Алексеевич Салищев – д.т.н., профессор кафедры МиН, зав. лабораторией ОНМ, НИУ «БелГУ».
https://orcid.org/0000-0002-0815-3525
E-mail: salishchev_g@bsu.edu.ru

Contribution of the authors

S.V. Naumov – planned and conducted experiments, wrote an article.

D.O. Panov – carried out forging, participated in the discussion of the results, corrected the article.

R.S. Chernichenko – prepared initial samples, prepared samples for research, conducted mechanical tests.

V.S. Sokolovsky – conducted EBSD analysis, conducted experiments, corrected the article.

E.I. Volokitina – prepared samples for structural studies.

N.D. Stepanov – participated in the discussion of the results.

S.V. Zherebtsov – participated in the discussion of the results.

E.B. Alekseev – produced the initial alloy for experiments.

N.A. Nochovnaya – determined the purpose of the work, produced the initial alloy for experiments.

G.A. Salishchev – determined the purpose of the work, participated in the discussion of the results, corrected the article.

Вклад авторов

С.В. Наумов – планирование и проведение экспериментов, подготовка текста.

Д.О. Панов – проведение ковки, участие в обсуждении результатов, правка статьи.

Р.С. Черниченко – подготовка исходных образцов и образцов для исследований, проведение механических испытаний.

В.С. Соколовский – проведение EBSD анализа, проведение экспериментов, правка статьи.

Е.И. Волокитина – подготовка образцов для структурных исследований.

Н.Д. Степанов – участие в обсуждении результатов.

С.В. Жеребцов – участие в обсуждении результатов.

Е.Б. Алексеев – приготовление исходного сплава для экспериментов.

Н.А. Ночовная – определение цели работы, изготовление исходного сплава для экспериментов.

Г.А. Салищев – научное руководство, участие в обсуждении результатов, правка статьи.

The article was submitted 03.09.2022, revised 08.03.2023, accepted for publication 10.03.2023

Статья поступила в редакцию 03.09.2022, доработана 08.03.2023, подписана в печать 10.03.2023

UDC 620.178.3
https://doi.org/10.17073/0021-3438-2023-2-74-82

Research article
Научная статья

Titanium alloy fatigue strength and eigenfrequency stability

D.I. Shetulov[1], **V.V. Mylnikov**[1], **E.A. Dmitriev**[2]

[1] **Nizhny Novgorod State University of Architecture and Civil Engineering**
65 Ilyinskaya Str., Nizhny Novgorod 603950, Russia

[2] **Komsomolsk-na-Amure State University**
27 Lenina Prosp., Komsomolsk-na-Amure 681013, Russia

✉ Vladimir V. Mylnikov (mrmylnikov@mail.ru)

Abstract: We conducted a study on fatigue in flat samples of the VT3-1 titanium alloy using "soft" cyclic beam bending tests. For this purpose, we developed an innovative electromagnetic test bench. The test bench's electromechanical system induces mechanical vibrations at a frequency that matches the eigenfrequency of the sample, ensuring that the cyclic load frequency remains constant. The electromagnetic force bends the sample while the elastic force unbends it, producing a quasi-sinusoidal cyclic load. Through our investigation, we determined the impact of this cyclic loading on both cyclic strength and durability. Our findings indicate that the VT3-1 titanium alloy possesses high resistance to fatigue and an endurance limit. Furthermore, we observed a low variability of the experimental fatigue resistance in relation to the approximating fatigue curve, suggesting the alloy has high structural stability. This finding indicates that the VT3-1 titanium alloy possesses high structural stability. To assess eigenfrequency stability, we subjected the alloy samples to cyclic tests, interrupting them at a reference number of 50 million cycles to evaluate changes in eigenfrequencies and stability under loads close to the fatigue limit. The results showed that the titanium alloy has a high level of eigenfrequency stability. Interruptions in cyclic tests resulted in jump-like increases in eigenfrequencies, which was not observed in continuous tests. Nevertheless, the total eigenfrequency deviations from the initial value at the end of the tests were similar in both cases.

Keywords: titanium alloy, fatigue resistance, eigenfrequency stability, cyclic loading frequency, eigenfrequency, endurance limit, durability, cyclic strength

For citation: Shetulov D.I., Mylnikov V.V., Dmitriev E.A. Titanium alloy fatigue strength and eigenfrequency stability. *Izvestiya. Non-Ferrous Metallurgy.* 2023;29(2):74–82. https://doi.org/10.17073/0021-3438-2023-2-74-82

Усталостная прочность и частотная стабильность титанового сплава

Д.И. Шетулов[1], **В.В. Мыльников**[1], **Э.А. Дмитриев**[2]

[1] **Нижегородский государственный архитектурно-строительный университет**
603950, Россия, г. Нижний Новгород, ул. Ильинская, 65

[2] **Комсомольский-на-Амуре государственный университет**
681013, Россия, г. Комсомольск-на-Амуре, пр-т Ленина, 27

✉ Владимир Викторович Мыльников (mrmylnikov@mail.ru)

Аннотация: Исследованы образцы титанового сплава ВТ3-1 на усталость при нагружении по «мягкой» схеме консольного изгиба плоских образцов. Для таких исследований была разработана оригинальная электромагнитная установка. В ней реа-

лизована работа на основе электромеханической системы, в которой возбуждение механических колебаний осуществляется исходя из собственной частоты колебания испытуемого образца, т.е. реализуется режим, когда частота возбуждающей силы (частота циклического нагружения) всегда равна частоте собственных колебаний образца. Изгиб образца производится электромагнитной силой, а разгиб происходит под действием сил упругости материала, тем самым обеспечивается циклическое нагружение, близкое к синусоидальному. Изучено влияние реализуемого в данной установке вида циклического нагружения на циклическую прочность и долговечность. Установлено, что исследуемый титановый сплав имеет высокие характеристики показателей сопротивления усталости и предела выносливости. В ходе проведенных исследований отмечен небольшой разброс экспериментальных значений сопротивления усталости образцов относительно аппроксимирующей линии кривой усталости, что свидетельствует о высокой стабильности структурно-чувствительных свойств титанового сплава ВТ3-1. Также исследованы образцы этого сплава на частотную стабильность. За контрольное число наработки было принято 50 млн циклов нагружения, при которых проводилась сравнительная оценка изменения частотных характеристик. Представлены частотные характеристики и выявлена динамика частотной стабильности испытаний образцов при нагрузках, близких к пределу усталости. Установлено, что исследуемый титановый сплав имеет высокие значения частотной стабильности. При этом перерывы в циклических испытаниях приводят к скачкообразному приросту частоты, а при непрерывных испытаниях такого не наблюдалось, однако общее отклонение частоты от первоначальной к концу испытаний примерно одинаковое.

Ключевые слова: титановый сплав, сопротивление усталости, частотная стабильность, частота циклического нагружения (ЧЦН), собственная частота колебаний (СЧК), предел выносливости, долговечность, циклическая прочность

Для цитирования: Шетулов Д.И., Мыльников В.В., Дмитриев Э.А. Усталостная прочность и частотная стабильность титанового сплава. *Известия вузов. Цветная металлургия*. 2023;29(2):74–82.

https://doi.org/10.17073/0021-3438-2023-2-74-82

Introduction

Inelastic materials are commonly utilized for manufacturing spring elements that operate under complex cyclic loading, as well as components that maintain their dimensions under loads [1—7]. Inelastic properties observed under cyclic loading can be referred to as internal friction, imperfect elasticity, damping, mechanical hysteresis, energy dissipation, or cyclic load ductility [8]. Many researchers posit that microplastic deformations arising from cyclic loading are local and sporadic due to the heterogeneity of the material micro-properties. Meanwhile, others utilize dynamic mechanical analysis under temperature variations to determine changes in elastic strength and activation energy of the micro deformations [9—12].

We employed a novel experimental procedure to assess the stability of eigenfrequency in materials utilized for manufacturing elastic elements in high-precision emitters which convert electrical oscillations into mechanical vibrations. Even minor fluctuations in eigenfrequency, resulting from changes in elastic modulus, inelasticity properties, and atom/lattice oscillations, can lead to unsatisfactory oscillation conversion errors and early onset of fatigue failure [13—16].

The aim of this study is to evaluate the cyclic strength and eigenfrequency stability of flat samples made of the VT3-1 titanium alloy under “soft” cyclic beam bending tests.

Materials and methods

We designed and constructed a specialized auto-oscillating electromagnetic bench (see Fig. 1) for conducting cyclic beam transverse bending tests on flat samples [17]. The electromechanical system induces mechanical vibrations at a frequency equivalent to the eigenfrequency of the sample (thus, the cyclic load frequency always matches the sample eigenfrequency). The electromagnetic force bends the sample while the elastic force unbends it, producing a quasi-sinusoidal cyclic load (see Fig. 2).

We produced flat samples following the design depicted in Fig. 3. The stress in the reference cross-section of the sample was determined by analyzing the vibration amplitude. The proposed method involves establishing a correlation between the force applied to the sample and the sample displacement at the point of application and then estimating the stress based on the known force. We identified the analytical force-displacement relationship for the steady mode. It is assumed that under cyclic loads, the forces applied to the sample (inertia, elasticity, and external forces) generate maximum stress and displacement equal to those produced by a static load with a magnitude equivalent to the dynamic resultant force.

We tested the VT3-1 high-strength titanium alloy with the following chemical composition (wt.%): 85.95—91.05 % Ti; 0.2—0.7 % Fe; up to 0.1 % C; 0.15—0.4 % Si; 0.8—2 % Cr; 2—3 % Mo; up to 0.05 % N; 5.5—7 % Al; up to 0.5 % Zr; up to 0.15 % O; up to 0.015 % H; other impurities: 0,3 % (GOST 19807-91).

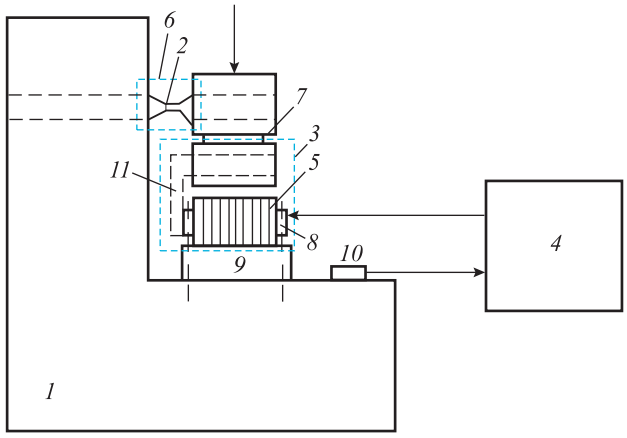

Fig. 1. Vibration stability test bench

1 – bed, ***2*** – sample, ***3*** – electromagnetic exciter, ***4*** – power supply and control components, ***5*** – solenoid coil, ***6*** – oscillation measuring system, ***7*** – ferromagnetic yoke, ***8*** – stator, ***9*** – dampers, ***10*** – accelerometer, ***11*** – П-shaped tape core

Рис. 1. Схема установки для испытаний на частотную стабильность

1 – станина, ***2*** – образец, ***3*** – электромагнитный возбудитель (ЭМ), ***4*** – блок питания и автоматики, ***5*** – катушка ЭМ, ***6*** – измерительная система параметров процесса колебаний, ***7*** – ферромагнитный якорь электромагнитного возбудителя, ***8*** – статор электромагнитного возбудителя, ***9*** – виброизоляторы, ***10*** – датчик виброускорения, ***11*** – П-образный ленточный сердечник

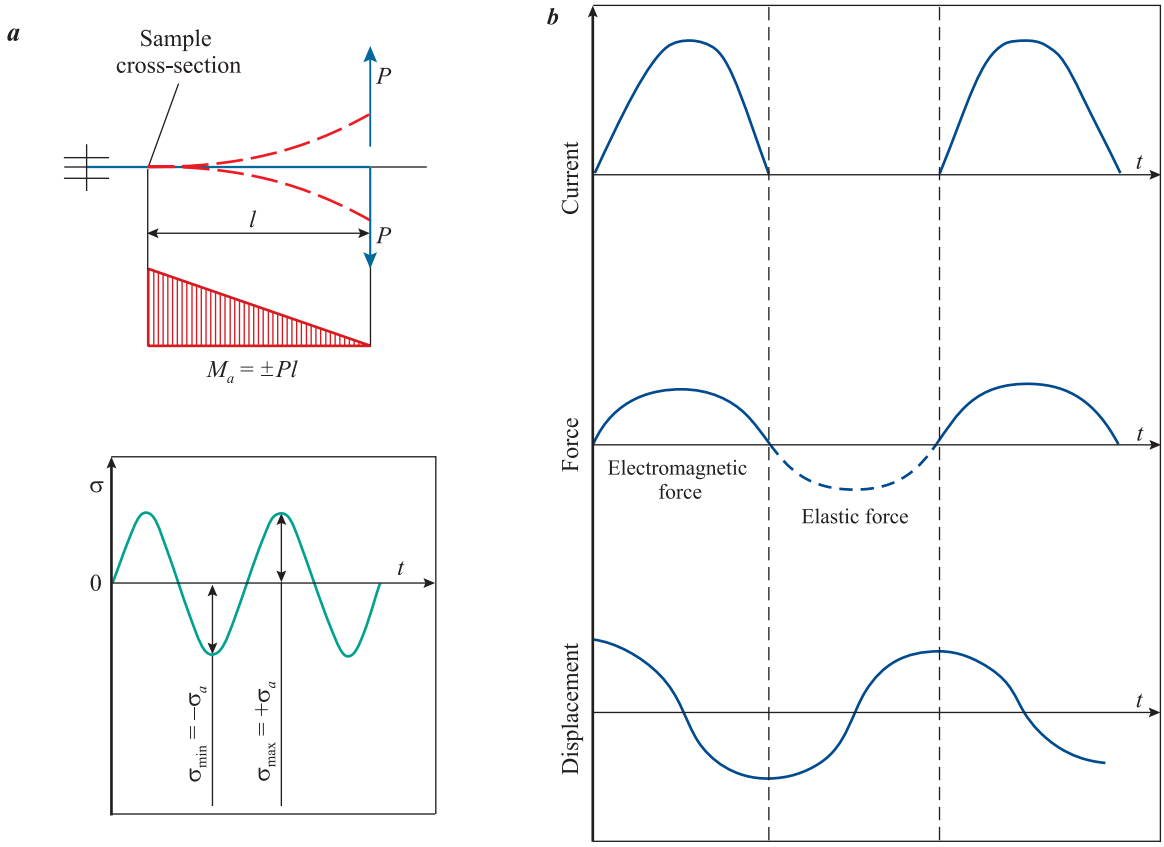

Fig. 2. Cyclic beam transverse bending of a flat sample (***a***). Synchronization of the current pulses, electromagnetic force, and elasticity force with the sample displacement (***b***)

Рис. 2. Нагружение по схеме консольного циклического поперечного изгиба плоского образца (***a***) и согласование импульсов тока, электромагнитной силы и силы упругости с перемещением консоли исследуемого образца в разработанной установке (***b***)

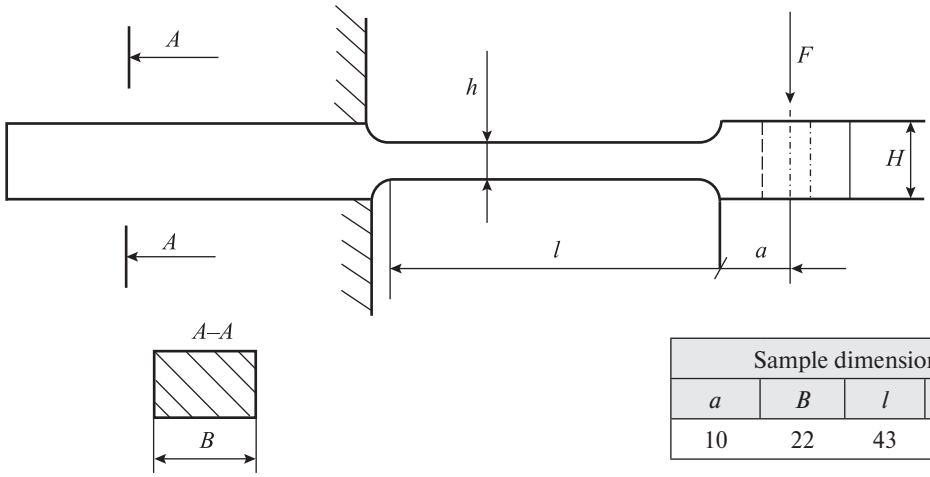

Sample dimensions, mm				
a	*B*	*l*	*h*	*H*
10	22	43	5	13

Fig. 3. Dimensional drawing of the test samples

Рис. 3. Эскиз и размеры образцов для испытания

The service life was set to be 50 million cycles, and we halted the fatigue tests each night, with the samples being stored under normal loading conditions.

As the stress approached the fatigue limit, the tests became more prolonged, and we kept the test bench operating overnight. However, we observed that the eigenfrequency of the sample altered after an overnight pause, whereby in the morning, following a 10-hour interruption, it was higher than the previous night when the test was halted.

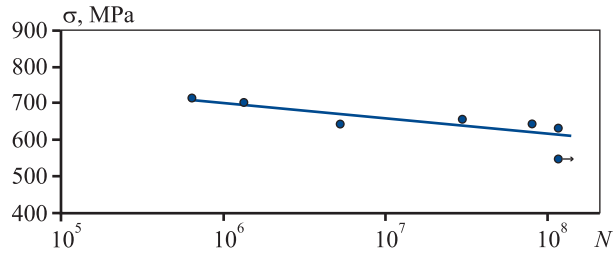

Fig. 4. VT3-1 titanium alloy fatigue curve after annealing at $t = 870$ °C

Рис. 4. Кривая усталости титанового сплава ВТ3-1 после отжига при $t = 870$ °C

Fatigue test results and discussion

Fig. 4 illustrates the fatigue curve obtained from the beam transverse self-oscillating bending tests conducted on the flat samples. The fatigue resistance, represented by the slope of the fatigue curve ($tg\alpha_w = 0.0394$), was found to be low (or very low compared to [18]), while the endurance limit ($\sigma_{-1} = 600$ MPa) was high. The fatigue test results displayed in Fig. 4 exhibited low variability when compared to the approximating fatigue curve, indicating the high stability of the alloy's structural properties.

According to papers [19, 20], the number of cycles (N) vs. stress ($tg\alpha_w$) curve becomes steeper as the damageability under cyclic loading increases. It is worth noting that the opposite triangle leg of $tg\alpha_w$ represents the stress in the sample, while the adjacent leg represents the number of cycles to failure:

$$tg\alpha_w = \frac{d \lg \sigma}{d \lg N}.$$

The physical significance of $tg\alpha_w$ is related to the propagation rate of local plastic deformation in the surface layer. In the case of beam transverse bending tests, only the surface layer of the sample undergoes plastic deformation, while the rest of the sample experiences elastic deformation. As a result, the propagation rate of plastic deformation in the surface layer is affected by the elastic deformation of the rest of the sample.

The slope angle of $tg\alpha_w$ indicates the increase in the number of cycles with respect to stress. A smaller $tg\alpha_w$ value corresponds to a longer time to failure even under high loads. On the other hand, a steeper slope angle of the fatigue curve correspond to a higher $tg\alpha_w$ value and a lower endurance of the sample. This means the VT3-1 titanium alloy features a low failure rate under cyclic loading.

Eigenfrequency test results and discussion

The key point is to investigate the eigenfrequency stability under loads close to the fatigue limit. To achieve this, individual samples were tested for eigenfrequency stability under the specified load. The samples used for the eigenfrequency tests had been subjected to different numbers of loading cycles. In order to make comparisons between the samples, the maximum eigenfrequency deviation (Δω) is assumed to be the eigenfrequency change from the initial value after $50 \cdot 10^6$ cycles. A positive Δω deviation represents an increase in the eigenfrequency, while a negative deviation represents a decrease.

Fig. 5 and 6 depict the eigenfrequencies of two VT3-1 titanium alloy samples under loads close to the fatigue limit.

Fig. 5, *a* displays two envelope curves, with the upper curve indicating the initial eigenfrequency and the lower curve representing the final eigenfrequency as the test bench was stopped after a daily run. The daily eigenfrequency changes during the cycle testing are contained within the area between the two curves.

In Fig. 5, *b* the eigenfrequencies are presented as a single polyline. The vertical steps signify the eigenfrequency changes following overnight breaks, while the sloped lines indicate the daily eigenfrequency variations as the number of load cycles increases.

The sample in Fig. 5, operated at 550 MPa stress, exhibited a total eigenfrequency deviation of 0.27 Hz. This deviation corresponds to the eigenfrequency deviation observed during the reference number of cycles (50 mln cycles). However, the largest eigenfrequency deviation of 0.36 Hz was observed approximately in the middle of the sample's service life, with the highest deviation occurring after the first 10 million cycles.

The total eigenfrequency deviation observed in the sample operated at 630 MPa stress in Fig. 6 was 0.34 Hz, which decreased to 0.32 Hz after the reference number of cycles (50 mln). No other significant eigenfrequency changes were detected. The largest eigenfrequency variation occurred after the first 10 million cycles, similar to the previous case.

It is worth noting that the observed eigenfrequency deviation was small (0.36 Hz), and its change during the overnight break was only 0.1 Hz.

Other researchers [21—25] have reported that fatigue test interruptions have little to no effect on the fatigue limit but may result in increased cycles to failure. However, in the case of eigenfrequency tests, our results indicate that interruptions do affect the eigenfrequency of the samples. Specifically, we observed a 0.1 Hz increase in eigenfrequency when the test bench was turned on in the morning compared to when it was turned off the night before.

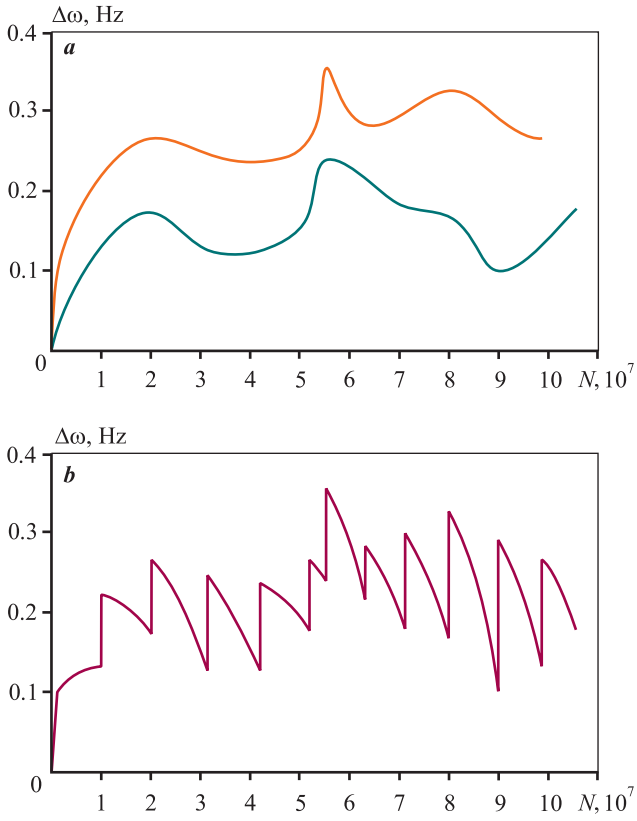

Fig. 5. Sample eigenfrequency variations (***a***) and deviations (***b***) vs. the number of load cycles
Initial eigenfrequency ω_0 = 231.28 Hz, load σ = 550 MPa

Рис. 5. Графические изображения изменения (***a***) и отклонения (***b***) частоты колебаний образца в зависимости от количества циклов нагружения
Начальная частота ω_0 = 231,28 Гц, нагрузка σ = 550 МПа

To provide a comparison, we conducted continuous tests on two samples of VT3-1 titanium alloy and found that the maximum eigenfrequency variation for sample *1* was +0.45 Hz, while for sample *2*, it was —0.09 Hz. This means that the eigenfrequency of sample *1* continuously increased, while that of sample *2* slightly decreased.

We also compared the eigenfrequencies recorded in the continuous and intermittent tests. The continuous tests did not result in any eigenfrequency jumps typical of the tests interrupted at night, but the overall eigenfrequency deviations from the initial value by the end of the tests were approximately the same. These findings further support the high stability of the titanium alloy eigenfrequency.

Continuous tests of the VT3-1 titanium alloy samples*

Результаты непрерывных испытаний образцов* из титанового сплава ВТ3-1

Sample *1*		Sample *2*	
Number of cycles, mln.	Frequency change, Hz	Number of cycles, mln.	Frequency change, Hz
1.9	0.13	2.0	0.01
5.4	0.15	4.5	–0.03
9.5	0.12	5.4	–0.07
12.8	0.22	10.5	–0.06
14.5	0.27	14.8	–0.04
20.3	0.31	19.0	–0.04
23.1	0.38	23.3	–0.05
24.7	0.37	24.2	–0.07
26.3	0.37	25.9	–0.08
27.2	0.43	26.1	–0.11
29.8	0.42	27.6	–0.10
32.3	0.45	28.6	–0.09
33.5	Failure	29.4	Failure

* Sample *1*. Stress $U = 550$ MPa, initial eigenfrequency $\omega_0 = 231.28$ Hz; sample *2*: $U = 580$ MPa, $\omega_0 = 238.8$ Hz.

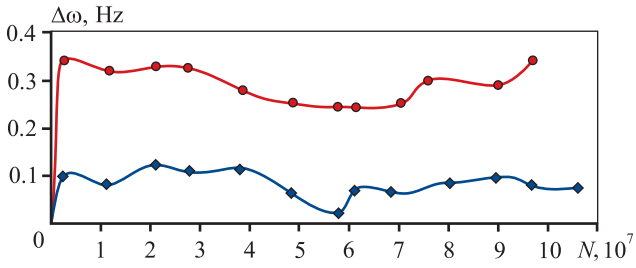

Fig. 6. Sample eigenfrequency deviations vs. the number of load cycles

Initial eigenfrequency $\omega_0 = 236.9$ Hz, load $\sigma = 630$ MPa

Рис. 6. Графическое изображение отклонений частоты колебаний образца в зависимости от количества циклов нагружения

Начальная частота $\omega_0 = 236{,}9$ Гц, нагрузка $\sigma = 630$ МПа

Conclusion

The fatigue behavior of VT3-1 titanium alloy flat samples was assessed using a "soft" self-oscillating cyclic beam bending test. The results indicated high fatigue resistance, with $tg\alpha_w$ value of 0.0394 and an endurance limit of $\sigma_{-1} = 600$ MPa. The fatigue test results also showed low variability relative to the approximating fatigue curve, suggesting high stability of the VT3-1 alloy eigenfrequency. The maximum eigenfrequency deviation observed was 0.36 Hz. However, cyclic test interruptions resulted in a jump in eigenfrequency of 0.1 Hz. Comparing the results of continuous and intermittent tests showed that both tests resulted in a similar total eigenfrequency deviation.

Overall, the VT3-1 alloy is well-suited for the manufacture of dimensionally stable components with low inelastic properties.

References

1. Terent'ev V.F., Korableva S.A. Fatigue of metals. Moscow: Nauka, 2015. 479 p. (In Russ).
   Терентьев В.Ф., Кораблева С.А. Усталость металлов. М.: Наука. 2015. 479 с.
2. Mughrabi H., Christ H.-J. Cyclic deformation and fatigue of selected ferritic and austenitic steels; specific aspects. *ISIJ International*. 1997;37(12):1154—1169.
3. Gromov V.E., Ivanov Yu.F., Vorobiev S.V., Konovalov S.V. Fatigue of steels modified by high intensity electron beams. Cambridge, 2015. 272 p.

4. Shkol'nik L.M. Fatigue testing methodology: Guide. Moscow: Metallurgiya, 1978. 304 p. (In Russ).
Школьник Л.М. Методика усталостных испытаний: Справочник. М.: Металлургия, 1978. 304 с.
5. Gadolina I.V., Makhutov N.A., Erpalov A.V. Varied approaches to loading assessment in fatigue studies. *International Journal of Fatigue*. 2021;144:106035. https://doi.org/10.1016/j.ijfatigue.2020.106035
6. Suresh S. Fatigue of metals. Cambridge University Press, 2006. 701 p.
7. Myl'nikov V.V., Kondrashkin O.B., Shetulov D.I., Chernyshov E.A., Pronin A.I. Fatigue resistance changes of structural steels at different load spectra. *Steel in Translation*. 2019;49(10):678—682. https://doi.org/10.3103/S0967091219100097
Мыльников В.В., Шетулов Д.И., Кондрашкин О.Б., Чернышов Е.А., Пронин А.И. Изменение показателей сопротивления усталости конструкционных сталей при различных спектрах нагружения. *Известия высших учебных заведений. Черная металлургия*. 2019; 62(10): 796—802. https://doi.org/10.17073/0368-0797-2019-10-796-802
8. Troshchenko V.T., Khamaza L.A., Pokrovsky V.V. Cyclic deformation and fatigue of metals (Ed. M. Bily). Amsterdam: Elsevier, 1993. 500 p.
9. Golovin S.A., Tikhonova I.V. Temperature dependence of internal friction and properties of deformed low-carbon iron alloys. *Deformatsiya i razrushenie materialov*. 2013;(7):16—21. (In Russ.).
Головин С.А., Тихонова И.В. Температурная зависимость внутреннего трения и свойства деформированных малоуглеродистых сплавов железа. *Деформация и разрушение материалов*. 2013;(7): 16—21.
10. Golovin S.A., Petrushina A.G. Temperature spectrum of internal friction of cast iron. *Izvestiya vysshikh uchebnykh zavedenii. Chernaya metallurgiya*. 2009; (9):51—54. (In Russ.).
Головин С.А., Петрушина А.Г. Температурный спектр внутреннего трения чугунов. *Известия высших учебных заведений. Черная металлургия*. 2009;(9):51—54.
11. McClaflin D., Fatemi A. Torsional deformation and fatigue of hardened steel including mean stress and stress gradient effects. *International Journal of Fatigue*. 2004;26(7):773—784. https://doi.org/10.1016/j.ijfatigue.2003.10.019
12. Golovin I.S., Bychkov A.S., Mikhailovskaya A.V., Dobatkin S.V. Contributions of phase and structural transformations in multicomponent Al—Mg alloys to the linear and nonlinear mechanisms of anelasticity. *The Physics of Metals and Metallography*. 2014;115(2):192—201. https://doi.org/10.1134/S0031918X14020082
Головин И.С., Бычков А.С., Михайловская А.В., Добаткин С.В. Вклад фазовых и структурных превращений в многокомпонентных Al—Mg сплавах в линейные и нелинейные механизмы неупругости. *Физика металлов и металловедение*. 2014;115(2):204. https://doi.org/10.7868/ S0015323014020089
13. Kardashev B.K., Sapozhnikov K.V., Betekhtin V.I., Kadomtsev A.G., Narykova M.V. Internal friction, young's modulus, and electrical resistivity of submicrocrystalline titanium. *Physics of the Solid State*. 2017;59(12):2381—2386. https://doi.org/10.1134/S1063783417120204
Кардашев Б.К., Сапожников К.В., Бетехтин В.И., КадомцевА.Г., Нарыкова М.В. Внутреннее трение, модуль Юнга и электросопротивление субмикрокристаллического титана. *Физика твердого тела*. 2017;59(12):2358—2362. https://doi.org/10.21883/FTT.2017.12.45231.131
14. Blanter M.S., Golovin I.S., Neuhäuser H., Sinning H.R. Internal friction in metallic materials. *Springer Series in Materials Science*. 2007;90:1—535. https://doi.org/10.1007/978-3-540-68758-0
15. Stolyarov V.V. Inelasticity of ultrafine-grained metals. *Izvestiya vysshikh uchebnykh zavedenii. Chernaya metallurgiya*. 2010;(11):51—54. (In Russ.).
Столяров В.В. Неупругость ультрамелкозернистых металлов. *Известия высших учебных заведений. Черная металлургия*. 2010;(11):51—54.
16. Romaniv O.N., Laz'ko L.P., Krys'kiv A.S. Relationship of internal friction to the fatigue life of patented steel wire. *Materials Science*. 1984;19:522—527. https://doi.org/10.1007/BF00722120
Романив О.Н., Лазько Л.П., Крыськив А.С. Зависимость внутреннего трения от усталостной долговечности запатентованной стальной проволоки. *Физико-химическая механика материалов*. 1984;19(6):44—50.
17. Myl'nikov V.V., Shetulov D.I. Fatigue testing facility. Patent 2781466 (RF). 2022. (In Russ.).
Мыльников В.В., Шетулов Д.И. Установка для испытаний на усталость: Патент 2781466 (РФ). 2022.
18. Myl'nikov V.V., Shetulov D.I., Chernyshov E.A. Variation in factors of fatigue resistance for some pure metals as a function of the frequency of loading cycles. *Russian Journal of Non-Ferrous Metals*. 2010;51(3):237—242. https://doi.org/10.3103/S1067821210030089
Мыльников В.В., Чернышов Е.А., Шетулов Д.И.

Изменение показателей сопротивления усталости некоторых чистых металлов в зависимости от влияния частоты циклов нагружения. *Известия вузов. Цветная металлургия*. 2010;(3):40—45.

19. Mylnikov V.V., Shetulov D.I., Chernyshov E.A. Investigation into the surface damage of pure metals allowing for the cyclic loading frequency. *Russian Journal of Non-Ferrous Metals*. 2013;54(3):229—233. https://doi.org/10.3103/S1067821213030103
Мыльников В.В., Шетулов Д.И., Чернышов Е.А. Исследование повреждаемости поверхности чистых металлов с учетом частоты циклического нагружения. *Известия вузов. Цветная металлургия*. 2013;(2):55—60.
20. Shetulov D.I On the estimation of the metals endurance fatigue by the damage of the surface anomalous layers. *Soviet Materials Science*. 1984;(6):117—120.
Шетулов Д.И. К оценке сопротивления усталости материалов по повреждению поверхностных аномальных слоев. *Физико-химическая механика материалов*. 1984. No. 6. С. 117—120.
21. Stephens R.I., Fatemi A., Stephens R., Fuchs H.O. Metal fatigue in engineering. New York: John Wiley & Sons, 2000. 472 p.
22. ASM Metals: HandBook. Vol. 19. Fatigue and fracture. ASM International, 2002. 2592 p.
23. Schijve J. Fatigue of structures and materials. Springer Science & Business Media, 2001.
24. Campbell F.C. Fatigue and fracture: Understanding the basics. ASM International, 2012. 525 p.
25. Lee Y-L., Barkey M.E., Kang H-T. Metal fatigue analysis handbook: Practical problem-solving techniques for computer-aided engineering. Butterworth-Heinemann: Elsevier Inc., 2011. 632 p.

Information about the authors

Dmitry I. Shetulov – Dr. Sci. (Eng.), Professor, Leading Researcher of the Department of Science, Nizhny Novgorod State University of Architecture and Civil Engineering (NGASU).
https://orcid.org/0009-0009-2826-5477
E-mail: schetulov@mail.ru

Vladimir V. Mylnikov – Cand. Sci. (Eng.), Associate Professor of the Department of Construction Technologies; Leading Researcher of the Department of Scientific Research, Innovation and Project Work; Head of the Laboratory of Strength and Plasticity of Functional Materials, NNGASU.
https://orcid.org/0000-0001-5545-4163
E-mail: mrmylnikov@mail.ru

Eduard A. Dmitriev – Dr. Sci. (Eng.), Rector of Komsomolsk-na-Amure State University.
https://orcid.org/0000-0001-8023-316X
E-mail: rector@knastu.ru

Информация об авторах

Дмитрий Иванович Шетулов – д.т.н., профессор, вед. науч. сотрудник Управления науки Нижегородского государственного архитектурно-строительного университета (ННГАСУ).
https://orcid.org/0009-0009-2826-5477
E-mail: schetulov@mail.ru

Владимир Викторович Мыльников – к.т.н., доцент кафедры технологии строительства; вед. науч. сотрудник Управления научных исследований, инноваций и проектных работ; зав. лабораторией «Прочность и пластичность функциональных материалов», ННГАСУ.
https://orcid.org/0000-0001-5545-4163
E-mail: mrmylnikov@mail.ru

Эдуард Анатольевич Дмитриев – д.т.н., ректор Комсомольского-на-Амуре государственного университета.
https://orcid.org/0000-0001-8023-316X
E-mail: rector@knastu.ru

Contribution of the authors

D.I. Shetulov – scientific guidance, correction of the text and conclusions.

V.V. Mylnikov – provision of the resources, preparation and management of the experiments, conducting the experiments, formation of the main concept, goal and objectives of the study; writing the text, formulation of the conclusions.

E.A. Dmitriev – analysis of the research results, correction of the text.

Вклад авторов

Д.И. Шетулов – научное руководство, корректировка текста, корректировка выводов.

В.В. Мыльников – обеспечение ресурсами, подготовка эксперимента, проведение экспериментов, формирование основной концепции, постановка цели и задачи исследования, подготовка текста, формулировка выводов.

Э.А. Дмитриев – анализ результатов исследований, корректировка текста.

The article was submitted 14.02.2023, revised 19.03.2023, accepted for publication 20.03.2023

Статья поступила в редакцию 14.02.2023, доработана 19.03.2023, подписана в печать 20.03.2023